Effect of Dissipation on the Dynamics of Superconducting Single Electron Transistors

by

Shuchao Meng

A thesis
presented to the University of Waterloo
in fulfilment of the
thesis requirement for the degree of
Doctor of Philosophy
in
Physics

Waterloo, Ontario, Canada, 2012

I hereby declare that I am the sole author of this thesis. This is a true copy of the thesis, including any required final revisions, as accepted by my examiners.

I understand that my thesis may be made electronically available to the public.

Shuchao Meng

Abstract

In this thesis, I will present the experimental results of the dynamics of superconducting single electron transistors (sSETs), under the influence of tunable dissipation. The sSET, consisting of two dc SQUIDs in series and the third gate electrode, is deposited onto a GaAs/AlGaAs heterostructure which contains a two dimensional electron gas plane 100nm beneath the substrate surface. The Josephson coupling energy, charging energy and dissipation related Hamiltonian can all be tuned *in situ*, while keeping others unchanged. We measured the switching current statistics and the transport properties, as a function of the dissipation and gate charge at different temperatures.

If the sSET is in the classical regime where phase is a good quantum variable, we found that the switching current and corresponding Josephson energy decrease as dissipation increases. Our observation agrees qualitatively with the theoretical calculation of a single Josephson junction with dominant Josephson energy, in a frequency dependent dissipative environment where energy barrier decreases as dissipation increases in thermally activated escape regime. This dissipation dependence result can be understood as the consequence of a reduced quantum fluctuations in the charge numbers.

Whereas in the charging regime, the switching current shows a 1e periodicity with respect to gate charge, indicating a pronounced charging effect. At a specific gate charge number, quantum fluctuations of the phase variable are compressed as dissipation increases, resulting in an enhanced switching current and Josephson energy. This result matches the theory

of a sSET capacitively coupled to a dissipative environment qualitatively. The temperature dependence of the switching current histogram indicates the existence of both quantum and classical thermal phase diffusion. Moreover, quantum charge fluctuations are minimized at the degeneracy point, causing a sharp dip on the width of the switching current histogram.

For a sSET with comparable Josephson energy and charging energy, quantum fluctuations of both phase and charge variables are significant. The influence of dissipation on the dynamics of the device is distinct in the classical and charging regimes. Dissipation compresses quantum phase fluctuations in the charging regime, whereas reduces the quantum charge fluctuations in the classical regime. The transition between these two regimes is found to be determined by the tunnel resistance of the SQUID. The competition between Josephson and charging energies, however, is not the intrinsic parameter of this transition. Our results imply that a detailed theoretical calculation of a sSET with comparable Josephson coupling energy and charging energy under the influence of dissipation is needed.

Acknowledgements

First, I would like to thank my supervisor Dr. Jan Kycia, for providing me with advice, encouragement and support through my graduate career. Not only I learned various knowledge and experimental skills from him, but most importantly, I have benefited a lot from his persistence, passion and perspective on scientific research which make him an excellent and inspiring advisor. In fact, I have acquired so much more when working with him. The study in his lab has been an impressive experience in my life and will be advantageous through the rest of my career.

I am very grateful to my advisory committee members: Dr. Frank Wilhelm, Dr. Hart Peemoeller, Dr. Tong Leung and former members Dr. Tom Devereaux and Dr. Arokia Nathan, for their helps and interests in my work. They gave me lots of useful suggestions when we met on the advisory committee meeting, for reviewing the progress of my project. Especially when I was attending the weekly meeting in Frank's group, I acquired much knowledge and ideas from the point of theorist's view.

Thanks to Jeff Quilliam and Luke Yaraskevitch who now are my best friends and have been working with me on the same dilution fridge. We have to split the experimental time because the different measurement setup conflicts sometimes. We had a really good collaboration and I learned a lot experimental technique and data analysis methods from their measurements on different magnetic materials.

Thanks many other people who have directly contributed to the experimental work in this thesis. Dr. Nina Heinig and Roberta Kelly helped to characterize the e-beam photolithography which is the crucial step for

device fabrication. Chas Mugford and Nat Persaud helped running the liquifier to feed the cryogenics. Dr. Andy Sachrajda in NRC provided the GaAs/AlGaAs substrate without which I was not able to perform this specially designed measurement. Also, I had a great time working with all labmates: Jeff Mason, Lauren Persaud, Jeff Hill, David Pomaranski, Halle Revell, Shaoxiong Li and Borko Djurkovic.

Finally, I am forever indebted to my parent, my sister, my wife Jinli and my childeren Sichun and Siluo who are most important in my life, not only for helping to support and encourage me but always bring me happiness.

Table of Contents

List of Tables

List of Figures

Chapter 1

Introduction

The dynamics of microscopic variables of an atomic scale object is governed by quantum mechanics. On a macroscopic scale, however, quantum mechanics can still survive in a collective state such as superconductivity, superfluidity and Josephson effect, which in fact are a manifestation of the coherent microscopic variables. These macroscopic quantum phenomena, described by macroscopic degrees of freedom, originate from the superpositions of a large number of quantum states of individual microscopic objects.

The macroscopic variable describing the Josephson effect or a Josephson junction, formed by two superconductors separated by a thin insulating barrier, is the phase difference φ of the condensed wave function in two superconductors. Within the resistively and capacitively shunted junction (RCSJ) model, the dynamics of φ is governed by the Josephson energy $E_J = \hbar I_C/2e$, the charging energy $E_C = e^2/2C$, and a shunting resistance R responsible for the dissipation, here I_C is the critical current and C is the junction capacitance. Associated with the charging energy, another quantum variable is the charge number Q on the junction capacitor, satisfying a commutation relation $[\varphi, Q] = 2ei$. If the dimension of a Josephson junction is large enough such that $E_J \gg E_C$, the phase is well-defined and the charging effect is negligible in this classical Josephson regime. As the

junction dimension is reduced down to the order of 100nm, the energy of an excess single charge on the junction capacitor becomes dominant so that $E_J \ll E_C$. The charge number now is a good quantum variable and the quantum fluctuations of the phase is significant.

This quantum mechanical effects in a mesoscopic Josephson junction have been investigated actively in recent years, for both fundamental physics and the great potential in different applications, such as being a quantum bit (qubit) [1, 2], a noise detector [3, 4] and a microwave photon counter [5]. For instance, a Cooper pair box, consisting of a small Josephson junction capacitively coupled to an electrode, has been used as a charge qubit whose quantum states are differentiated by the Cooper pair numbers [6, 7]. A superconducting loop, interrupted by one [8] or three [9, 10] Josephson junctions, can form another type of quantum two-level system with the flux through the loop pointing up or down, named flux qubit. Considering the multiple quantized energy levels in the potential well of a current biased junction, the so-called phase qubit has been studied using a single Josephson junction with well-defined phase variable [11, 12, 13]. Moreover, different Josephson junction circuits have been used as the probes to read out different quantum states. In terms of characteristic energies of the Josephson junction, the E_J/E_C ratio decreases as the dimension of the junctions is reduced. E_J/E_C is estimated to be $\gg 10^4$ in the phase qubit, ~ 50 in the flux qubit and on the order of unity in the charge qubit.

As the main component of the circuit on the substrate, the Josephson junction inherently interacts with various degrees of freedom, causing its intrinsic coherence to be weakened. For instance, critical current fluctuations can substantially limit the coherence in all types of Josephson junction circuits [14]. Except for this intrinsic dissipation, the coupling to a particular degree of freedom in the environment is another type of main decoherence source, such as the low frequency charge noise [15, 16], low frequency flux noise [17], dielectric loss in the substrate [18] and some high frequency resonant modes in the electromagnetic environment [19].

In order to obtain a longer coherence time, one approach is to eliminate the noise coupled to the qubit, and another is to tune the device's parameters so that it is intrinsically immune to unwanted degrees of freedom. For example, a modified charge qubit, in an intermediate regime where E_J is comparable to E_C, can be operated close to the double degeneracy point of charge and flux states where the device is not sensitive to both charge and flux noise [20, 21]. Moreover, a single Josephson junction with E_J/E_C on the order of unity, shunted by a very large inductance of a Josephson junction array, can be seen as a new type of charge-based qubit [22, 23]. This device shows the unique feature of the immunization to offset charge noise induced by random, slowly drifting microscopic charges which are inherent in many solid-state systems. A Cooper pair box with a large $E_J/E_C \sim 50$ can also be operated in the charging regime where the qubit is not sensitive to background charge noise [24, 25].

In fact, A. J. Leggett has drawn the attention to a macroscopic quantum tunneling system coupled to a dissipative environment which acts as a bath of harmonic oscillators interacting linearly with the system [26, 27]. Especially, Josephson junction circuits with a dominating Josephson energy show superconducting behavior at very low temperature, with the well-defined phase variable. As the charge energy rises, the localized charge leads to the Coulomb blockade of Cooper pair tunneling and causes the phase to fluctuate quantum mechanically. Thus, the phase order may be destroyed completely when E_J/E_C is lowered below a critical value, resulting in an insulating state. Dissipation in such small Josephson junction circuits will damp the quantum fluctuations of the phase, and drive a transition from insulator to superconductor even if $E_J < E_C$. These dissipation driven phase transitions have been studied in a single Josephson junction [28, 29], a superconducting single electron transistor (sSET) [30], one dimensional [31] and two dimensional [32, 33, 34, 35] Josephson junction arrays, even a junction coupled to a carbon nanotube [36].

Of great interest is the influence of dissipation on the dynamics of small Josephson junction circuits where interplay between the phase, charge,

phase diffusion, macroscopic quantum tunneling, thermally activated escape and Coulomb blockade may all be accessed. This subject has been extensively studied both theoretically [37, 38, 39, 40, 41, 42, 43, 44, 45, 46, 47] and experimentally in several different configurations, notably in a single Josephson junction [22, 28, 48, 49, 50] and in a superconducting single electron transistor [30, 51]. Of course, the dissipation seen by the junction has to be characterized accurately. For instance, a shunting resistor can be fabricated on-chip and its resistance can be easily estimated from the low frequency I-V measurement. In the microwave frequency range, however, the real part of the total effective impedance $Re[Z(\omega)]$, responsible for the dissipation, is on the order of the vacuum impedance $Z_0 \approx 50\Omega$, if there does not exist any high resistive element within a wavelength distance from the junction. Several methods have been used for building a desired dissipative environment, such as a normal metal shunting resistor [30, 52, 53], a tunable delay transmission line [48, 54], a high resistance Josephson junction array [50, 55], a two dimensional electron gas (2DEG) grounding plane [33, 51, 56], a quantum dot [57] and a capacitively coupled graphene layer [58].

Josephson junction circuits with different Josephson energy, charging energy and total impedance of the circuit can be summarized in different regimes, as depicted in Fig. 1.1. If $E_J/E_C \gg 1$, the junction is dominated by the phase in the Josephson regime. The self-shunting resistance is normally much less than the resistance quantum $R_Q = h/e^2 \approx 25.9k\Omega R_Q$. Thus the total impedance of the environment is very low. In the opposite regime where a small, high resistance Josephson junction is in the charging regime and has a high impedance environment ($Re[Z] \gg R_Q$), the incoherent charge tunneling becomes dominant and the charge is individually transferred across the junction [59, 60].

The sSET, as the most sensitive electrometer [60, 61, 62, 63], has attracted much attention due to its capability of having a combined Josephson and charging effect. This device normally consists of two Josephson junctions in series and the third gate electrode capacitively coupled to the

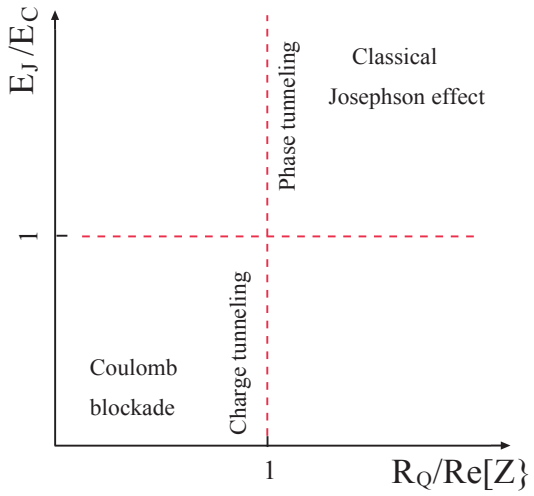

Figure 1.1: The Josephson junction circuits with different values of E_J/E_C and shunting impedance.

central island. From the phase point of view, the sSET can be seen as a single Josephson junction with gate controlled critical current [53, 64, 65]. On the other hand, the small superconducting island is well isolated from the external environment via two high resistance junctions. Thus, the excess charge number on the island is well-defined so that the discrete charge tunnels across the device one by one. This device is a good test bed to study the dynamics of a macroscopic quantum tunneling circuit in the intermediate regime where the competition between Josephson energy and charging energy is dramatic, i.e. quantum fluctuations of both phase and charge variables are significant.

To study the influence of a dissipative environment on a sSET, different approaches have been performed, such as a shunting resistor [30, 66], a capacitively coupled 2DEG [47, 51], microwave photons [67], a microstrip transmission line [68] and a high impedance Josephson junction array [69, 70]. It has been shown that the theoretical prediction based on the assumption $E_J/E_C \ll 1$ could not fully interpret the experimental

results with $E_J \approx E_C$ in some details [47, 51]. The theory, however, is consistent with the measurement in the strong charging regime [30]. Most importantly, a detailed picture of the influence of dissipation on a Josephson junction device with comparable E_J and E_C remains an open question.

Therefore, in this thesis, we will present the measurement on a Josephson junction circuit with fully controlled E_J/E_C on the order of unity and an *in situ* tunable low impedance dissipative environment. Specifically, we have performed a comprehensive investigation of the switching current (I_{SW}) and transport property on the sSETs, in both the classical Josephson and charging regimes respectively. Our design is also compared to the Josephson junction circuits with common leads which act as transmission lines with a typical impedance $Z_0 \approx 50\Omega$ at microwave frequency.

Our sSETs consist of two superconducting quantum interference devices (SQUIDs) in series and a relative large central island. A small magnetic field can be applied perpendicular to the SQUID via a superconducting solenoid, tuning the effective Josephson coupling energy. The gate voltage is applied to the conductive 2DEG plane to adjust the potential on the island and charge related energy. A low impedance dissipative environment is generated via capacitively coupling the sSET to a two dimensional electron gas 100nm beneath the substrate surface. The GaAs/$Al_{0.3}Ga_{0.7}$As heterostructure substrate is placed onto a back gate. A negative back gate voltage can be applied for producing a uniform electrical field to the 2DEG, tuning the sheet resistance and the consequent total impedance seen by the sSET. We focused on the microwave frequency range where the capacitive coupling between the sSET and the 2DEG is strong, ensuring the low impedance, dissipative environment $Re[Z] \ll R_Q$. All the electrical leads are highly filtered to minimize high frequency noise for a low noise environment.

The sSET switches out from the superconducting state into the finite voltage state as bias current is ramped up. The switching current is the maximum supercurrent which the device can support. From the statistics

of these stochastic switching events, we can derive the escape or tunneling rate of the phase in both thermally activated and quantum tunneling regimes, as well as the effective critical current and Josephson energy. By tuning the dissipation, we can find the optimal operating regime where the device is not sensitive to unwanted degrees of freedom. The transport property in a voltage biased configuration will show a rich structure of current peaks arising from the internal resonance modes or the external resonances in the environment.

A brief overview of the structure of this thesis is as follows:

In **Chapter 2**, we start with the theory of a single Josephson junction. Thermally activated escape and macroscopic quantum tunneling will be discussed. After we go through a semiclassical description of a SET in both normal state and superconducting state, we will show the influence of dissipation on the transport property which is the main task in this thesis. The analogs between a dc SQUID and a sSET will also be discussed.

In **Chapter 3**, we will show the experimental techniques used in our measurement, including sample design and fabrication, dissipation characterization, cryogenic techniques and low noise electronic techniques.

In **Chapter 4**, we will present the experimental results, starting with characterizing the sample parameters and data acquisition method. The switching current statistics of the sSET in classical Josephson regime will be shown and compared to the theoretical calculation. The data of a different device in the charging regime will be presented for different values of gate charge, dissipation and temperature. The temperature dependence of the switching current histogram will be discussed in terms of quantum and classical phase diffusion. We also show the effect of dissipation on the transport of a sSET with a much higher tunnel resistance. In addition, some problems involved in our experiment will be discussed.

In the last **Chapter**, by summarizing the experimental results, we conclude that the influence of dissipation on the sSET in the classical regime is opposite to that of the sSET in the charging regime. A transition between these two regimes occurs when the SQUID tunnel resistance

$R_N = R_Q/2$. Our measurement can be used as an effective method to determine whether phase or charge variable is a good quantum number.

Chapter 2

Theory of Single Electron Transistors

In this chapter we will give a theoretical overview of the experiment, covering several Josephson junction circuits. Section 2.1 discusses a single Josephson junction from classical regime to charging regime. Then the semiclassical description of a single electron transistor will be shown, in both normal state and superconducting state. In the last section, we will go through the effect of electromagnetic environment on different junction circuits.

2.1 Single Josephson Junction

2.1.1 Josephson effect

If a superconductor is cooled below the transition temperature, two electrons will bind together through the interaction with a phonon, to form a Cooper pair with charge 2e. All the Cooper pairs will enter in the same quantum state which can be described by a macroscopic wave function having amplitude $|\psi|$ and phase φ as $\psi = |\psi| \exp i\varphi$. A Josephson junction can be created when two superconductors are separated by a very thin insulating layer ($\sim$1nm). Due to the small thickness of the insulating barrier, the wave functions in the two electrodes can overlap, allowing

Cooper pairs to tunnel across the junction [71, 72].

In 1962 Josephson made the remarkable prediction that a zero voltage supercurrent [73]

$$I_s = I_C \sin \Delta\varphi \tag{2.1}$$

can flow across a Josephson junction. In this so-called dc Josephson relation, $\Delta\varphi$ is the phase difference of the Ginzbrug-Laudau wavefunction in the two superconductors, and the critical current I_C is the maximum supercurrent that the junction can support. At zero magnetic field the critical current is given by the Ambegaokar-Baratoff relation [74]

$$I_C R_N = \frac{\pi \Delta(T)}{2e} \tanh \frac{\Delta(T)}{2k_B T}, \tag{2.2}$$

where R_N is the normal state resistance of the junction and $\Delta(T)$ is the temperature dependent superconducting gap. The other physical constants are electron charge $e = 1.6 \times 10^{-19} C$ and Boltzmann constant $k_B = 1.38 \times 10^{-23} J \cdot K^{-1}$.

If a voltage V is applied to a Josephson junction, the phase difference will evolve according to

$$\frac{d\Delta\varphi}{dt} = \frac{2eV}{\hbar}, \tag{2.3}$$

where $\hbar = 1.05 \times 10^{-34} J \cdot S$ is the reduced Planck constant. This equation will cause an oscillating supercurrent with an amplitude I_C at frequency $f_J = 2eV/h$. This ac Josephson relation links voltage and frequency only through fundamental constants e and h. From both dc and ac Josephson relations, a Josephson junction can be regarded as an inductor with a dynamic non-linear inductance

$$L_J = \frac{\hbar}{2e} \frac{1}{I_C \cos \Delta\varphi}. \tag{2.4}$$

If a Josephson junction is driven by electromagnetic radiation at frequency f_{ac}, the response of dc current-voltage (I-V) characteristics gives rise to multiple constant voltage steps (Shapiro steps) at $V_n =$

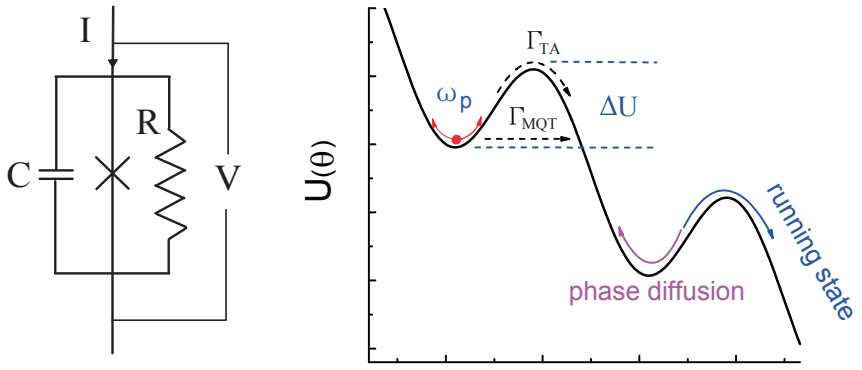

Figure 2.1: The circuit of RCSJ model and the washboard potential. The phase particle could escape out from the bottom of one potential well via thermal activation (TA) or macroscopic quantum tunneling (MQT).

$nhf_{ac}/2e$ [75]. This type of synchronization with an external source of electromagnetic radiation can be used as a voltage standard because the frequency can be measured with a very high precision.

The phase difference, $\Delta\varphi$, is not a gauge-invariant variable so that it does not have a unique value. Considering the existence of a magnetic field, the gauge-invariant phase difference θ is defined as

$$\theta \equiv \Delta\varphi - (2\pi/\Phi_0)\int \mathbf{A}\cdot d\mathbf{S}, \tag{2.5}$$

where $\mathbf{A}$ is the vector potential, $\Phi_0 = h/2e$ is the flux quanta and $h = 6.63\times10^{-34} J\cdot S$ is Planck constant. The integration is from one electrode of the junction to another, over the junction area $\mathbf{S}$. In the dc and ac Josephson relation, $\Delta\varphi$ should be replaced by θ.

To describe the dynamics of a realistic Josephson junction, the resistively and capacitively shunted junction (RCSJ) model is normally used [76, 77], in which the ideal junction is shunted by a resistor R and capacitor C, as illustrated in Fig. 2.1. Within this model, the phase

difference θ of a current biased Josephson junction is described by the following equation

$$I = I_C \sin\theta + V/R + C dV/dt. \tag{2.6}$$

Using the ac Josephson relation, we can obtain the second-order nonlinear differential equation

$$I = I_C \sin\theta + \frac{\hbar}{2eR}\frac{d\theta}{dt} + \frac{C\hbar}{2e}\frac{d^2\theta}{dt^2}. \tag{2.7}$$

Defining a dimensionless time variable $\tau = \omega_{p0} t$ with

$$\omega_{p0} = \sqrt{2eI_C/\hbar C}, \tag{2.8}$$

Equation (2.7) can be rewritten as

$$\frac{d^2\theta}{d\tau^2} + \frac{1}{Q}\frac{d\theta}{d\tau} = \frac{\partial U(\theta)}{\partial\theta} \tag{2.9}$$

with a defined potential

$$U(\theta) = -E_J(\cos\theta + \gamma\theta). \tag{2.10}$$

Equation (2.9) is the analog to the equation of motion of a particle of mass $m = (\hbar/2e)^2 C$ moving along the tilted washboard potential $U(\theta)$ with a slope proportional to normalized bias current $\gamma = I/I_C$ (see Fig. 2.1). Here, ω_{p0} is the plasma frequency of the oscillating phase particle at the bottom of one potential well with $I = 0$ and $Q = \omega_{p0} RC$ is the quality factor. The Josephson coupling energy is defined as

$$E_J = \frac{\hbar}{2e} I_C. \tag{2.11}$$

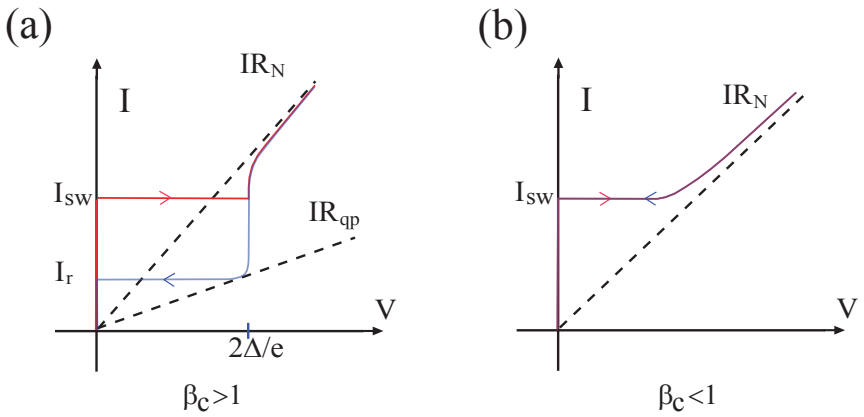

Figure 2.2: (a) Hysteretic I-V curve of an underdamped Josephson junction. (b) Non-hysteretic I-V curve of an overdamped Josephson junction. At finite temperature, switching current I_{SW} replaces the critical current I_C.

Another damping parameter, which is more frequently used, is defined as

$$\beta_c \equiv Q^2 = \frac{2eI_C R^2 C}{\hbar}. \tag{2.12}$$

In the absence of thermal and quantum fluctuations, in the case $\gamma < 1$, the junction is in the zero-voltage state which corresponds to the particle being trapped in the bottom of one potential well. As current is increased above I_C, the particle will escape out of the bottom and roll down along the washboard, resulting in a voltage across the junction. For different damping, the junction shows two types of I-V characteristics corresponding to an overdamped case with $\beta_c < 1$ and an underdamped case with $\beta_c > 1$. As shown in Fig. 2.2, if $\beta_c < 1$, the equation $V = R(I^2 - I_C^2)^{1/2}$ smoothly interpolates between $V = 0$ for $I < I_C$ and resistive behavior $V = IR$ for $I \gg I_C$. In the underdamped case, the hysteretic I-V curve is no longer a single value function. The voltage first jumps discontinuously to a finite value $2\Delta/e$. If I is reduced below I_C, the voltage will not drop back to

zero until a retrapping current $I_r \approx 4I_C/\pi Q$ is reached. As the bias is reduced, the energy fed from bias current can not be dissipated as phase rolls down on the board until a much smaller bias current I_r. The particle is then trapped in one local minima and the junction goes back into the supercurrent branch.

2.1.2 Escape Rate

For an underdamped Josephson junction, at finite temperatures $T > 0$, the phase particle may escape out from one potential well by thermally activated (TA) processes [48, 49, 78, 79] or macroscopic quantum tunneling (MQT) through the barrier [80, 81, 82, 83, 84]. At the switching current $I_{SW} < I_C$, the Josephson junction switches into the $2\Delta/e$ voltage state.

The energy barrier for escape or tunneling is current dependent. It is written as [78]

$$\Delta U(\gamma) = 2E_J[(1-\gamma^2)^{1/2} - \gamma\cos^{-1}\gamma] \tag{2.13}$$

for $I < I_C$. As γ is increased, the plasma frequency of the phase particle is also weakly dependent on bias current

$$\omega_p = \omega_{p0}(1-\gamma^2)^{1/4}. \tag{2.14}$$

As $\gamma \to 1$, Equation (2.13) can be approximated as

$$\Delta U(\gamma) \approx \frac{4\sqrt{2}}{3}E_J(1-\gamma^{3/2}). \tag{2.15}$$

The thermally activated escape rate Γ_{TA} is dominant at a high temperature, following Kramers formula [85]

$$\Gamma_{TA} = a_t\frac{\omega_p}{2\pi}\exp\left(-\frac{\Delta U}{k_B T}\right) \tag{2.16}$$

where a_t is a temperature and damping dependent prefactor

$$a_t = 4/(\sqrt{1 + Qk_BT/1.8\Delta U} + 1)^2. \tag{2.17}$$

As temperature is lowered, thermally activated escape is exponentially suppressed. Below a crossover temperature T_{cr}

$$T_{cr} \approx \frac{\hbar\omega_p}{2\pi k_B} = \frac{\hbar\omega_{p0}}{2\pi k_B}(1-\gamma^2)^{1/4}, \tag{2.18}$$

the quantum tunneling rate Γ_{MQT} exceeds Γ_{TA}. Within the Wentzel-Kramers-Brillouin (WKB) approximation, this rate is

$$\Gamma_{MQT} = a_q \frac{\omega_p}{2\pi} \exp\left(-\frac{36}{5}\frac{\Delta U}{\hbar\omega_p}(1 + \frac{0.87}{Q})\right) \tag{2.19}$$

with

$$a_q \approx [120\pi\frac{36}{5}\frac{\Delta U}{\hbar\omega_p}]^{1/2}. \tag{2.20}$$

Note that Γ_{MQT}, ω_p and ΔU are all dependent on the bias current. The MQT rate is exponentially dependent on the damping, or Γ_{MQT} decreases as more dissipation is introduced, causing the phase to be more localized. Defining a relevant coefficient $\alpha = 1/2Q$, T_{cr} is estimated to be

$$T_{cr} \approx \frac{\hbar\omega_p}{2\pi k_B}[(1+\alpha^2)^{1/2} - \alpha]. \tag{2.21}$$

Thus, stronger damping implies a lower T_{cr}, causing the MQT more difficult to be observed.

In the case of low temperatures and small damping, the energy of the phase particle in one potential well is quantized [11, 86]. Because one Josephson junction can be deemed as an anharmonic oscillator consisting of a capacitor and a non-linear inductor, the energy spacing between two adjacent quantized levels become smaller as higher excited states are occupied. The energy level spacing between the ground and first excited

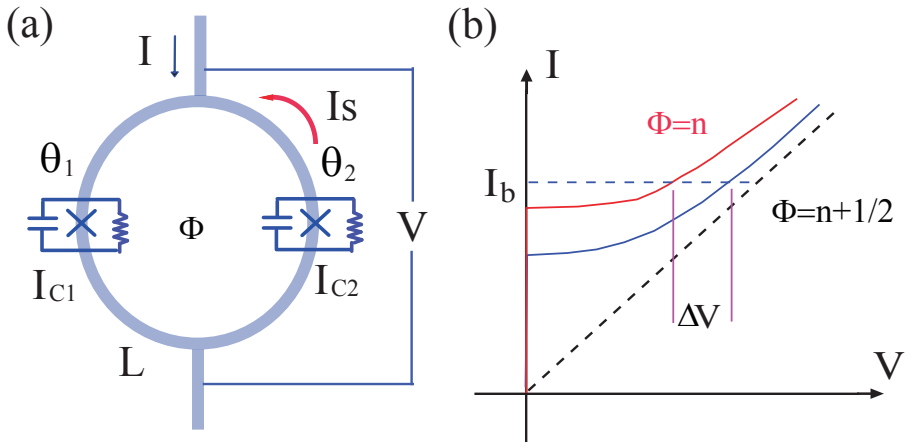

Figure 2.3: (a) Illustration of a dc SQUID. (b) Non-hysteretic I-V curves at different values of flux in the loop.

state in a parabolic approximation is

$$E_{01} = h\omega_p. \tag{2.22}$$

If a microwave radiation at frequency f_{mw} is applied to the junction, single photon or multi-photon absorption could drive the transition between the ground and first excited state, fulfilling the condition: $E_{01} = nhf_{mw}$ where n is the photon number (for example, see Ref. [12, 13, 87]).

2.1.3 dc SQUID

A dc SQUID normally consists of two Josephson junctions connected in parallel in a superconducting loop, as sketched in Fig. 2.3 (a). Defining the critical current and phase of junction 1 and 2 as $I_{C1,2}$ and $\theta_{1,2}$ respectively, the bias current I is split between two junctions as

$$I = I_{C1}\sin\theta_1 + I_{C2}\sin\theta_2. \tag{2.23}$$

The flux quantization in the superconducting loop requires

$$\theta_1 - \theta_2 = 2\pi\Phi/\Phi_0(mod2\pi), \tag{2.24}$$

here Φ is the total flux through the loop. Assuming two junctions have the same critical current I_C and the external flux is Φ_e, Φ could be written by

$$\Phi = \Phi_e + LI_s \tag{2.25}$$

with the circulating screening current I_s

$$I_s = \frac{I_C}{2}(\sin\theta_1 - \sin\theta_2), \tag{2.26}$$

where L is the loop inductance. All the equations are considered in the zero-voltage state. If the loop inductance L is much smaller than the junction inductance L_J, the parameter of the SQUID, $\beta_L \equiv 2LI_C/\Phi_0 \ll 1$, $\Phi = \Phi_e$ and the screening current is negligible. Thus, we can get a fully tuned current from zero to maximum $2I_C$ by applying an external field:

$$I = 2I_C \sin\theta|\cos(\pi\Phi/\Phi_0)|. \tag{2.27}$$

In this case, the SQUID behaves effectively as a single junction with flux dependent critical current $2I_C|\cos(\pi\Phi/\Phi_0)|$. Indeed, the SQUIDs in our devices stay in this regime so that we can tune the critical current and effective Josephson coupling energy from the maximum down to zero. The relative amplitude of the modulation of the critical current with flux is affected strongly by β_L. If $\beta_L = 1$, the modulation is 50%. In the case $\beta_L \gg 1$, it is inversely proportional to β_L.

If a dc SQUID is operated as a magnetometer, it becomes a flux to voltage convertor. The SQUID must fulfill two conditions in order to have a high sensitivity and low noise. For the junction, $\beta_c < 1$ ensures a single value I-V relation. For the superconducting loop, $\beta_L \leq 1$ is the optimal working point. Normally, the bias current is set to be slightly greater than

$2I_C$ and the I-V curves are shifted between two typical curves shown in Fig. 2.3(b) as the flux in the loop changes. Thus, the output voltage will be a periodic function of external magnetic filed, with a periodicity Φ_0.

Considering two phase variables in two Josephson junctions, the dynamics of a dc SQUID must be seen as the equation of motion of a particle in a two dimensional (2D) potential. Basically, it is a tilted parabolic shape potential which is shifted by Φ_e with multiple meta-stable states separated by a saddle point. The 2D macroscopic quantum tunneling has been observed in a current biased hysteretic dc SQUID [88, 89].

2.1.4 Ultra-small Junction

All the discussion of a Josephson junction above is in the classical Josephson regime where we only consider the phase variable of the junction. In a quantum mechanical description, the charge operator Q associated with the junction capacitance C is a conjugate variable to $(\hbar/2e)\varphi$. This causes the commutation relation

$$[\varphi, Q] = 2ie. \tag{2.28}$$

This phase-charge uncertainty relation does not play a major role for a large junction because of the negligible Q operator. However, if the junction size is reduced to be so small that the energy cost of a single charge (electron or Cooper pair) across the junction is significant, a quantum mechanical description of the junction is needed. For simplicity, we can write the Hamiltonian of a zero-biased small Josephson junction as [39, 59, 60]

$$H_0 = E_C(\frac{Q}{e})^2 - E_J \cos\varphi, \tag{2.29}$$

where in the φ representation, the charge operator is

$$Q = \frac{2e}{i}\frac{\partial}{\partial\varphi} \tag{2.30}$$

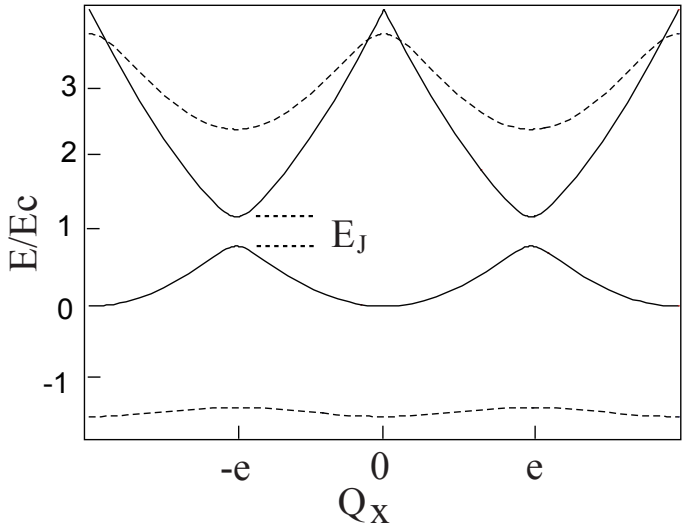

Figure 2.4: The ground and first excited energy bands of a single Josephson junction for two values of E_J/E_C. Solid line: $E_J/E_C = 0.2$ and dashed line: $E_J/E_C = 2$.

and the charging energy E_C is defined as

$$E_C = \frac{e^2}{2C}, \tag{2.31}$$

corresponding to the static energy of one discrete charge on the capacitor. Obviously, for a normal state tunnel junction, the $2e$ in the charge operator will be replaced by e.

Accordingly, from the Josephson energy term $-E_J \cos\varphi$, equation (2.29) describes a particle moving in a periodic potential. The energy eigenstate has the form of

$$\psi_{n,Q_x}(\varphi + 2\pi) = \exp(i2\pi\frac{Q_x}{2e})\psi_{n,Q_x}(\varphi), \tag{2.32}$$

where n is the order of an eigenstate which is dependent on a charging parameter Q_x considered as a "quasi-charge" in analog to the quasi-

momentum in a Bloch state in a periodic lattice. This charge state has a definite number of Cooper pairs, but a completely indefinite phase variable. The energy level $E_n(Q_x)$ has a band structure having a periodicity $2e$, covering $-e \leq Q_x \leq e$ in the first Brillouin zone. The detailed expression of $E_n(Q_x)$ depends on the competition between E_J and E_C, as shown in Fig. 2.4.

In the "nearly free-electron" limit with $E_C \gg E_J$, the energy band is approximately given by a parabolic function $E_n(Q_x) \approx Q_x^2/2C$ in the extended Brillouin zones. The band gap at the boundary where $Q_x = \pm e$ is

$$\delta E_n = E_C(E_J/E_C)^n/n^{n-1}. \tag{2.33}$$

Apparently, the first band gap between the ground and first excited state is the Josephson coupling energy E_J.

In the opposite limit $E_C \ll E_J$, the ground state has the energy

$$E_0(Q_x) = -\Delta_0 \cos\frac{2\pi Q_x}{2e}, \tag{2.34}$$

where the width of the band is

$$\Delta_0 = 16(\frac{E_J E_C}{\pi})^{1/2}(\frac{E_J}{2E_C})^{1/4}\exp[-(8\frac{E_J}{E_C})^{1/2}] \tag{2.35}$$

and the energy gap to the first excited state is

$$\delta E_1 = \hbar\omega_{p0}. \tag{2.36}$$

In this strong Josephson limit, the junction more likely stays in the ground state because of the large band gap.

Analogous to the ac Josephson effect which describes the current oscillation occurring in a voltage biased junction, a dc current biased small junction with $E_C \gg E_J$ at very low temperature can show similar voltage oscillations (Bloch oscillations) due to the coherence of Cooper pair tunneling with high shunting impedance. If the driving current is

very small, the quasi-charge Q_x is increased adiabatically and the system stays in the lowest band. The voltage across the junction will oscillate at a frequency $f_{Bloch} = I/2e$. To observe this effect, a dc plus ac current can be applied to the junction simultaneously [90]. If the ac frequency is in resonance with the Bloch oscillation frequency, the I-V characteristics will show resonant current peaks.

For a small junction with well-defined charge numbers, two conditions must be satisfied for Coulomb charging energy. At first, E_C should be considerably larger than thermal noise at experimental temperature: $E_C \gg k_B T$. Secondly, it must exceed the quantum energy uncertainty associated with the time constant of the junction: $\Delta E \geq h/2R_T C$. Thus the junction tunnel resistance R_T must satisfy

$$R_T \geq R_K \tag{2.37}$$

where $R_K = h/e^2 \approx 25.9k\Omega$ is the resistance quantum.

We now look at a normal tunnel junction with high R_T and well-controlled charge numbers at zero temperature. An electron tunneling, causing the charge to change from Q to $Q - e$, is only possible if the difference of charging energies before and after the tunneling is positive

$$\Delta E = \frac{Q^2}{2C} - \frac{(Q-e)^2}{2C} \geq 0. \tag{2.38}$$

This condition is satisfied only if $Q \geq e/2$, or the voltage on the junction is $V \leq e/2C$. In other words, there is no current flowing through the junction in the range $-e/2C < V < e/2C$. This current suppression below certain voltage is named Coulomb blockade. If the junction is current biased, the junction is charged up to $V = e/2C$ in a period, causing one electron to tunnel. The voltage then drops down to $-e/2C$ and increases again. This cycling process is a single electron Bloch oscillation which has a frequency $f_{Bloch} = I/e$.

It is well known that the tunneling process occurs only via exchanging

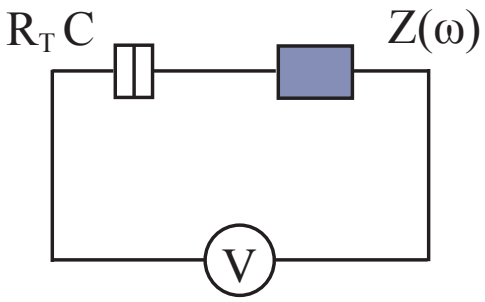

Figure 2.5: The circuit of an ultra-small tunnel junction biased by the voltage source via the external impedance $Z(\omega)$.

energy between the junction and the electromagnetic environment in which the junction is embedded [40, 41, 42]. In this charging regime, the tunneling rate of single charge is directly proportional to the energy exchange probability $P(E)$.

As shown in Fig. 2.5, one ultra-small junction is biased by a voltage in series with the impedance $Z(\omega)$. Note that the current biased configuration can be treated in the same way as this case, where the voltage source is a function of the time averaged current through the junction. Using the Caldeira-Leggett model [26, 27], the environment can be treated quantum mechanically as an infinite set of LC harmonic oscillators. In general, the impedance $Z(\omega)$ consists of some resistive components which are responsible for dissipation.

The forward tunneling rate is written as

$$\overrightarrow{\Gamma}(V) = \frac{1}{e^2 R}\int_{-\infty}^{+\infty} dE \frac{E}{1-\exp(-E/k_B T)} P(eV-E), \tag{2.39}$$

where, the probability function $P(E)$ is

$$P(E) = \frac{1}{2\pi\hbar}\int_{-\infty}^{+\infty} dt \exp[J(t) + \frac{i}{\hbar}ET]. \tag{2.40}$$

The phase-phase correlation function $J(t)$ is mainly determined by the real part of the total impedance as

$$J(t) = 2\int_0^{+\infty} \frac{d\omega}{\omega} \frac{ReZ_T(\omega)}{R_K} [coth\frac{\hbar\omega}{2k_BT}(\cos\omega t - 1) - i\sin\omega t], \quad (2.41)$$

where the total impedance of the circuit $Z_T(\omega)$ is composed by the junction capacitance in parallel with $Z(\omega)$ as

$$Z_T(\omega) = \frac{1}{i\omega C + Z^{-1}(\omega)}. \quad (2.42)$$

We can also write the backward tunneling rate as

$$\overrightarrow{\Gamma}(V) = \overleftarrow{\Gamma}(-V). \quad (2.43)$$

Thus, the total current or the I-V characteristics is

$$I(V) = e(\overrightarrow{\Gamma}(V) - \overleftarrow{\Gamma}(V)). \quad (2.44)$$

Obviously, the dynamics of an ultra-small tunnel junction is affected strongly by the shunting impedance. If this impedance is much less than the resistance quantum, then we can make a good approximation that $Z(\omega) = 0$. This will cause $P(E) = \delta(E)$. The junction shows a standard resistive I-V curve without Coulomb gap voltage. In the high impedance case where $ReZ(\omega) \gg R_K$, we find $P(E) = \delta(E - E_C)$ at low temperature. This means that only if the energy provided by the source satisfies $eV = E_C$, the electron can tunnel through the junction via transferring the same amount of energy to the environment. Thus, the Coulomb gap $e/2C$ is recovered.

Now we look at a ultra-small Josephson junction with $E_C \gg E_J$ biased by a voltage V. Using the same method, the Cooper pair current flowing

through this superconducting junction is [43, 46, 91]

$$I(V) = 2e(\overrightarrow{\Gamma}(V) - \overleftarrow{\Gamma}(V)) = \frac{\pi e E_J^2}{\hbar}[P(2eV) - P(-2eV)]. \tag{2.45}$$

To illustrate the fundamental behavior of this Josephson junction, we assume a simple case where a shunting resistor R forms a pure ohmic environment. In the low impedance limit where $R \ll R_K$, the function $P(2eV)$ is peaked at $V = 0$ and I-V curve shows a supercurrent at zero voltage. The quantum fluctuations of the phase variable increase as charging effect increases. A larger E_C/E_J ratio causes a smaller effective Josephson coupling energy E_J^* [44, 46]. Consequently, the supercurrent branch of the I-V curve turns into a "supercurrent" peak, showing a clear phase diffusion region. The strong damping from the low impedance environment can compress the quantum fluctuations of the phase, increasing the effective Josephson energy. At finite temperature, the results of $P(E)$ theory in this regime coincide with the picture for the phase diffusion in a junction with overdamped phase dynamics [43].

When the impedance of the environment is increased, the charging effects becomes observable. In the case $R > R_K$, the function $P(2eV)$ is peaked around the voltage $V = E_C^*/2e$, where $E_C^* = (2e)^2/2C$ is the charging energy corresponding to one Cooper pair. The tunneling of Cooper pairs is now determined by the interplay of energy from the voltage source and the Cooper pair charging energy. When these two energies have equal value, the condition for tunneling is satisfied and the I-V curve shows a current peak centered around the value $V_b = e/C$. If we replace the single electron by a Cooper pair in the normal state junction case, we can also get this result. The peak becomes sharper as the impedance of the environment increases. The experiments performed on a single Josephson junctions with $E_C \gg E_J$, in a high impedance ohmic environment, have shown the current peaks induced by incoherent Cooper pair tunneling at non-zero voltage [52].

For a small underdamped Josephson junction having high tunnel resis-

tance, the characteristic frequencies involved in the dynamics such as MQT, TA escape and retrapping rate are very high. For instance, the plasma frequency is $\omega_p \sim 10^{11}$Hz and the retrapping voltage V_g corresponds to a frequency $2eV_g/\hbar \sim 10^{12}$Hz. Unless extremely small, high impedance components are fabricated close to the junction (within 1mm), the high frequency shunting impedance of the whole circuit, which is seen by the junction, plays a major role. Generally, the leads connecting the junction to the current and voltage bonding pads show a typical impedance on the order of the vacuum impedance $Z_0 \approx 50\Omega$ at a microwave frequency.

It is crucial to understand the effect of this low impedance (strong damping) in small, high resistance junction circuits. This has a significant impact on the low temperature behavior of the retrapping current $I_r(T)$. $I_r(T)$ does not drop continuously as temperature decreases, showing a temperature independent region below a threshold. This observation can not be explained within the RCSJ model where $I_r(T)$ is estimated to be $4I_C/\pi Q$, decreasing exponentially with the freezing out of the quasi-particle damping as $\exp(-\Delta/k_BT)$. Instead, the damping mechanism mainly is due to the high frequency lead impedance Z_0 which exceeds the quasi-particle damping at low temperature [92, 93].

Another consequence of this strong damping is the phase diffusion in an underdamped small junction before it switches into the gap voltage state [38, 94]. Similar to the nonhysteretic overdamped junction which has finite thermally activated resistance below I_C, the small junction is overdamped at microwave frequency. As the bias current increases above a threshold, the phase particle has nonzero probability to roll over the energy barriers and to be retrapped into the bottom of the next potential well, causing a finite voltage pulse. The repeating diffusion events will cause a finite resistance before the junction switches into the gap voltage state. Indeed, phase diffusion even can exist in the underdamped regime of a current biased small junction [95]. In a specially designed extremely low impedance environment, a small and nonhysteretic Josephson junction may recover its theoretical critical current [96].

To observe the charging nature of a small Josephson junction, it not only requires a high tunnel resistance, but also a high shunting impedance. In practice, a very high impedance condition is very hard to fulfill. The low impedance formed by the lead may wash out the charging nature of a small junction by reducing the quantum fluctuations of the phase variable. A high impedance environment can be obtained by depositing high resistance normal metal close to the junction [28, 52, 97] or using the SQUID arrays as the leads which exhibits a very high dynamic resistance if the flux through the loop is tuned to be $\Phi_0/2$. Although the effective impedance of the junction array can not be described by a linear impedance model, it still was used to observe the Coulomb blockade of Cooper-pair and coherent tunneling in a single Josephson junction [50, 55, 98].

2.2 Single Electron Transistor

Although a single junction can be operated in the charging regime, the charge related Hamiltonian is constant. Using a gate electrode to voltage bias a Josephson junction via a capacitor, the island is isolated from external environment by the junction. Thus, the charge on the island can be well-defined, forming a so-called Cooper pair box. By adding one more junction to the island, a double junction system can sustain a dc current with a gate controlled potential on the island. In this section, we will show the theoretical description of such a device, named a single electron transistor (SET), in both the normal state and the superconducting state. The effect of the electromagnetic environment on the sSET will also be addressed.

2.2.1 SET in Normal State

As shown in Fig. 2.6. A normal state SET can be made using normal metal or driving the superconducting SET to normal state in a strong magnetic field. At first, we focus on the mesoscopic island which is effectively

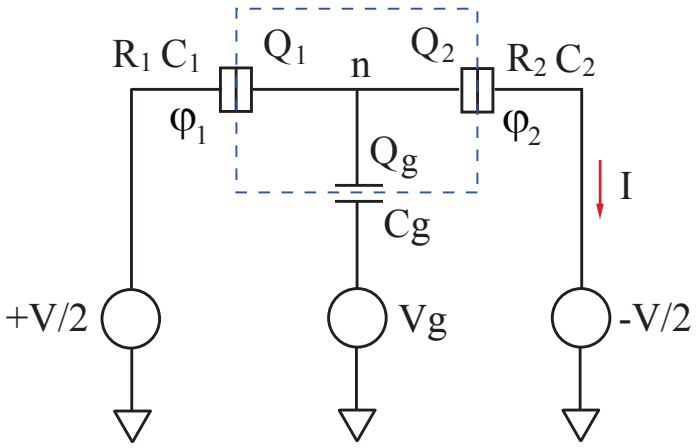

Figure 2.6: The configuration of a SET. The island (dashed box) includes the capacitors of two tunnel junctions and the gate capacitance C_g. Gate voltage V_g is used to control the offset charge on the island.

isolated from the external circuit by two tunnel junctions. Defining the charging energy

$$E_C = e^2/2C_\Sigma, \tag{2.46}$$

here $C_\Sigma = C_1 + C_2 + C_g$ is the total capacitance of the island, $C_{1,2}$ denote the capacitance of two junctions and C_g is the gate capacitance. We assume the temperature is low enough so that $E_C \gg K_B T$. Moreover, two time constants of the circuit R_1C_1 and R_2C_2 have to be longer than the uncertainty time associated with the Coulomb energy $\Delta t \sim h/2E_C$. This ensures the charge on the island to be localized. Thus the junction tunnel resistance must satisfy

$$R_{1,2} > R_K. \tag{2.47}$$

Under these circumstances, the SET is in the Coulomb-blockade regime, and the electron number on the island is a good quantum variable. We assume Q_1, Q_2 and Q_g are the charge number on two junction capacitors and gate capacitor, respectively. The island charge number is $n = Q_1 -$

$Q_2 - Q_g$. The tunneling of one excess electron on the island increases the total island charge by e. The increase of the island potential due to the tunneling can be large enough so that the tunneling of subsequent electrons is prevented. For a symmetrically voltage biased SET, when one electron tunnels on the island across the first junction, the charge number on the island increases from n to $n+1$. Thus, the electrostatic energy difference is

$$\Delta E_1^+ = \frac{e}{C_\Sigma}[(C_2 + \frac{1}{2}C_g)V + (C_g V_g - ne) - \frac{1}{2}e]. \tag{2.48}$$

In this equation, $Q_g = C_g V_g$ acts effectively as an offset charge on the island. Therefore, Q_g can be controlled by adjusting the electrostatic potential V_g on the gate. Similarly, we can write the energy difference ΔE_2^- for one electron tunneling off the island through the second junction, corresponding to the island charge number dropping back to n. These two steps result in one electron being transferred across the SET from left to right. We can also get the energy ΔE_1^- and ΔE_2^+ which are the energies for an electron tunneling across the island from right to left.

A net current can flow through the SET only if the tunneling is electrostatically favorable, requiring $\Delta E_{1,2}^{\pm} > 0$. We can get the $V - V_g$ relations which are shown as multiple parallel lines fulfilling these equations. As shown in Fig. 2.7, the energy eV has to be larger than the energy difference between the initial and final states, which is dependent on the gate charge number Q_g. At the charge degeneracy point $Q_g/e = 1/2$, the energy difference decreases down to zero. Current now can pass the SET even for a bias $V \sim 0$.

For the conditions $\Delta E_{1,2}^{\pm} < 0$, the charge states are stable because of the unfavorable energy cost. We can get the following equations

$$e(n - \frac{1}{2}) < C_g V_g + (C_2 + \frac{1}{2}C_g)V < e(n + \frac{1}{2}) \tag{2.49}$$

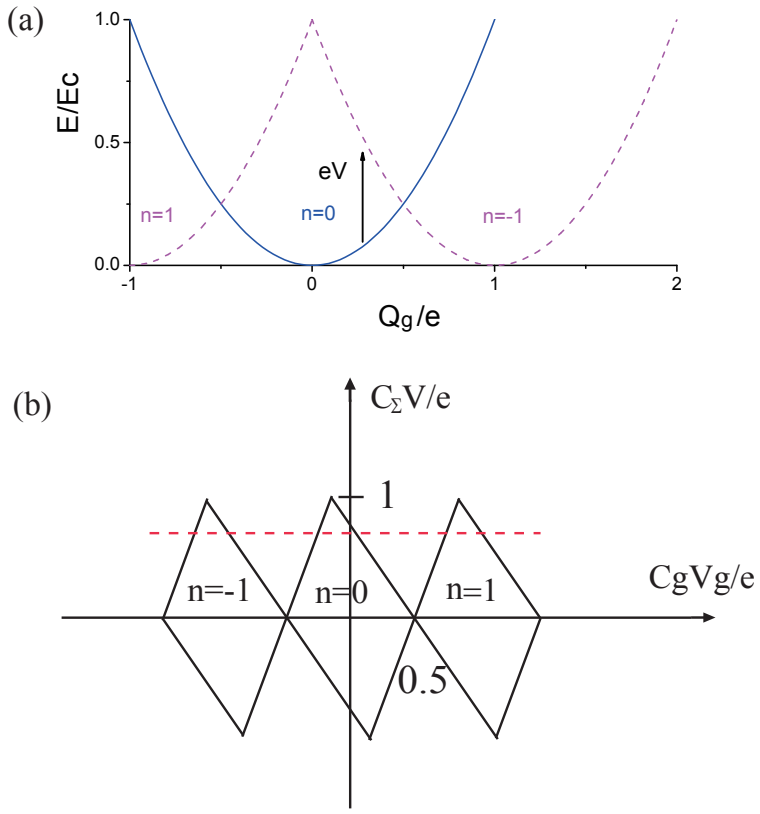

Figure 2.7: (a) Schematic illustration for single electron tunneling conditions. (b) The stability diagram of a normal state SET with $C_1 = 2C_2 = 10C_g$. Inside these diamond regions, there is a certain number of electrons on the island.

$$e(n-\frac{1}{2}) < C_g V_g - (C_1 + \frac{1}{2}C_g)V < e(n+\frac{1}{2}). \tag{2.50}$$

Inside these diamond regions on the $V - V_g$ plane (see Fig. 2.7 (b)), the island has a certain number of electrons. The transitions between different charge states are suppressed by Coulomb blockade effect. Thus, no current can flow through the device. If we apply a bias voltage $V < e/C_\Sigma$ and sweep the gate voltage V_g simultaneously, periodic current peaks will be observed when the SET is driven out of the stable diamond regions. These

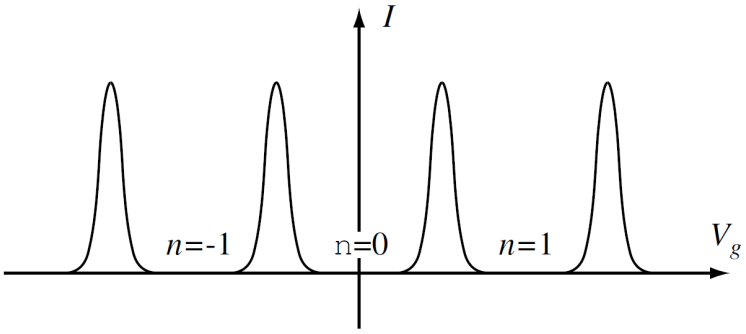

Figure 2.8: Coulomb blockade oscillations of a SET for a bias voltage $V < e/C_\Sigma$.

Coulomb blockade oscillations are illustrated in Fig. 2.8.

2.2.2 SET in Superconducting State

If the SET is made of superconducting material, and operated below the superconducting transition temperature of the material, the SET goes into a superconducting state. Actually, this is the common case because a single charge tunneling device is always cooled down to mK range, for reducing thermal fluctuations. For instance, ultra-small Al/AlO_x/Al tunnel junctions are commonly used in a metallic SET because of the high quality, native oxide insulting layer which grows on Al. In this case, the charge carriers are Cooper pairs or quasi-particles. For this type of superconducting SET with superconducting leads and island, sometimes called Cooper pair transistor, we have to take into account the superconducting energy gap Δ and the Josephson coupling energy $E_{J1,2}$ of both junctions.

For simplicity, we assume $E_{J1,2} \ll E_C$ so that the number of Cooper pairs is well-defined and the sSET is governed by the charging energy of the island, here $E_C = e^2/2C_\Sigma$ is still the island charging energy. We can obtain the similar Coulomb blockade equations for Cooper pair tunneling. At low bias voltage, the charge carriers are purely Cooper pairs. When

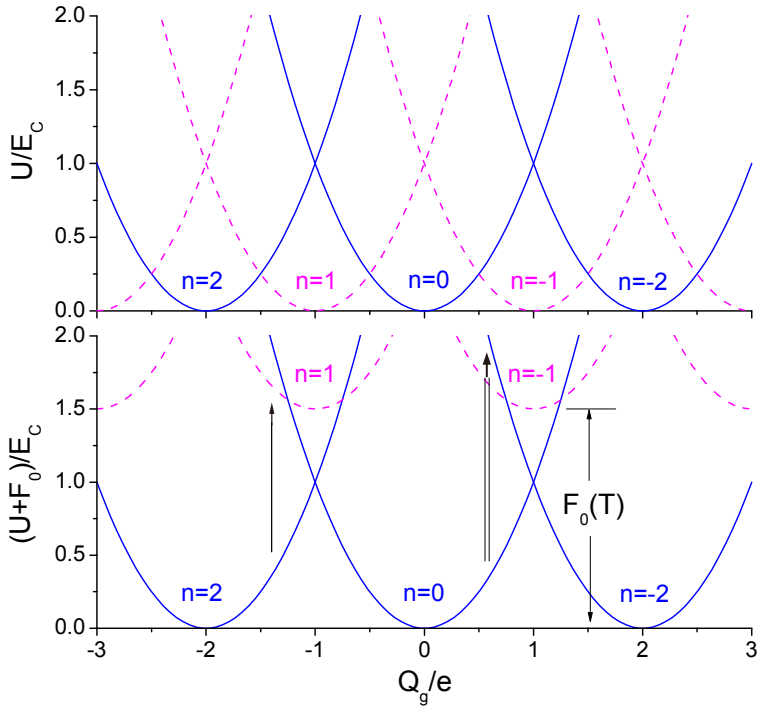

Figure 2.9: The energy of a superconducting SET in different charge states. Bottom panel: superconducting state with lifted odd charge state. Single and double lines are electron and Cooper pair tunneling respectively.

one pair tunnels across the first Josephson junction, the island charge number is changed by $2e$. This type of tunneling is dissipationless, i.e. the energy provided by bias eV must be equal to the energy difference between different charging states.

The quasi-particles can be generated only by a large bias voltage $V > 2\Delta/e$, which can break the Cooper pairs. Once there exists a quasi-particle, the free energy of the sSET with odd charge number is lifted up by $F_0(T)$. As shown in Fig. 2.9, the energy difference between an odd and even charge state is assumed to be $F_0(T) > E_C$. For the electron tunneling (single line), the extra energy $2F_0(T)$ must be provided to break one Cooper pair.

At very low temperature, a sSET should have a $2e$ periodic oscillation of conductance or switching current with respect to the gate charge while sweeping V_g. As temperature increases to a crossover temperature T^*, a crossover from $2e$ to e occurs. This parity effect is induced by the populated charging states with odd numbers, over the states with even numbers [53, 99, 100, 101, 102, 103, 104, 105]. This type of parity change can also be induced by Andreev reflections in a superconductor-normal metal junction device [106, 107].

Note that T^* is normally much smaller than T_c so that $\Delta(T^*) \approx \Delta(0) \gg k_B T$. For all values of Q_g, the non-degenerate ground state has a even number. The odd number state is the first excited state with degeneracy N_{eff} which denotes the total number of excited states in the entire island volume, within an energy gap $K_B T$ above the superconducting gap. The excitations with even or odd number have grand canonical partition functions above the ground state

$$Z_{even} = [(1+e^{-\Delta/k_B T})^{N_{eff}} + (1-e^{-\Delta/k_B T})^{N_{eff}}]/2 \tag{2.51}$$

and

$$Z_{odd} = [(1+e^{-\Delta/k_B T})^{N_{eff}} - (1-e^{-\Delta/k_B T})^{N_{eff}}]/2. \tag{2.52}$$

Thus, the free energy difference between these two states is derived to be

$$F_0(T) = k_B T \ln \frac{Z_{even}}{Z_{odd}} = k_B T \ln \frac{(1+e^{-\Delta/k_B T})^{N_{eff}} + (1-e^{-\Delta/k_B T})^{N_{eff}}}{(1+e^{-\Delta/k_B T})^{N_{eff}} - (1-e^{-\Delta/k_B T})^{N_{eff}}}. \tag{2.53}$$

The exact number of states available for excitations is the integration over the energy above the superconducting gap

$$N_{eff} = 2V\rho(0) \int_{\Delta}^{\infty} \exp[-(\epsilon-\Delta)/k_B T] \frac{\epsilon}{(\epsilon^2-\Delta^2)^{1/2}} d\epsilon, \tag{2.54}$$

where V is the island volume, $\rho(0)$ is the density of states including spin per unit volume at Fermi level and ϵ is the excitation energy. At very low

temperature, N_{eff} and $F_0(T)$ are estimated to be

$$N_{eff} \approx 2\sqrt{2}V\rho(0)(\Delta k_B T)^{1/2} \tag{2.55}$$

and

$$F_0(T) \approx \Delta - k_B T \ln N_{eff}. \tag{2.56}$$

At a certain temperature $T^* = \Delta/k_B \ln N_{eff}$, $F_0(T)$ drops down to zero, causing an equal probability of the system having an odd or even charge number. Note that this is a pure thermal effect and we ignore the existence of quasi-particles. In reality, the quasi-particle poisoning in a sSET is very common if there does not exist any special treatment for building an energy barrier to block the tunneling of quasi-particles onto the island, such as a quasi-particle filter or trap on chip [108, 109].

Defining $\varphi_{1,2}$ as the phase and $E_{J1,2}$ as the Joseohson coupling energy of two Josephson junctions respectively, the total number of Cooper pairs across the sSET is $Q_\phi = (Q_1 + Q_2)/2$, the excess charges on the island is $2ne = Q_1 - Q_2 - Q_g$, where $Q_{1,2}$ are the charges on the first and second junctions and $Q_g = C_g V_g$ is the charge on the gate. The Hamiltonian of the sSET at zero current bias can be written as [110]

$$H_0 = E_C(n - \frac{Q_g}{e})^2 - E_{J1}\cos\varphi_1 - E_{J2}\cos\varphi_2, \tag{2.57}$$

here we exclude the environment related energy term which will be discussed in next chapter.

For the two Josephson terms, the total phase across two junctions is

$$\phi = \varphi_1 + \varphi_2 \tag{2.58}$$

which behaves as a classical variable. On the contrary, the phase of the island

$$\theta = (\varphi_1 - \varphi_2)/2 \tag{2.59}$$

is a quantum variable and obeys the commutation relation with n

$$[\theta, n] = 2i. \tag{2.60}$$

The classical variable ϕ has another commutation relation with Q_ϕ as $[\phi, Q_\phi] = 2ei$. Thus, the sSET has the Hamiltonian

$$H_0 = E_C(n - \frac{Q_g}{e})^2 - E_J(\phi)\cos(\theta - \chi) \tag{2.61}$$

where

$$E_J(\phi) = \sqrt{E_{J1}^2 + E_{J2}^2 + 2E_{J1}E_{J2}\cos\phi} \tag{2.62}$$

and

$$\chi = \arctan(\frac{E_{J1} - E_{J2}}{E_{J1} + E_{J2}}\tan\frac{\phi}{2}). \tag{2.63}$$

Equation (2.61) describes a gate dependent single junction Hamiltonian with quantum variable θ of the island which is effectively isolated from external environment. The eigenstates of this sSET can be solved to be band structures with energy $E_m(Q_g, \phi)$, having two conjugate coordinates: charge and total phase on the island. The bands are $2e$ periodic with gate charge Q_g and 2π periodic with phase ϕ. If the sSET is symmetric with identical junctions, $E_{J0} = E_{J1} = E_{J2}$, the Josephson energy term in the sSET Hamiltonian is simplified to be $-2E_{J0}\cos(\phi/2)\cos\theta$.

2.2.3 sSET in Electromagnetic Environment

The electromagnetic environment has to be taken into account in determining the tunneling of Cooper pairs in a sSET circuit. In the low impedance limit, the I-V curve of the sSET is characterized by a supercurrent branch at a vanishing voltage. The total phase ϕ is well-defined. A bias current I applied to the sSET will add the term $-(\Phi_0/2\pi)I\phi$ to the Hamiltonian. This external current tilts the two dimensional energy along the ϕ direction.

The critical current of the sSET for the mth energy band at gate charge

Q_g is found to be

$$I_C^m(Q_g) = \frac{2\pi}{\Phi_0}\frac{\partial E_m(Q_g,\phi)}{\partial \phi}. \tag{2.64}$$

Being a function of Q_g, this current will show an even parity if there does not exist any quasi-particle excitation on the island. For a specific gate charge, $I_C^m(Q_g)$ is maximized for the lowest band (ground state) and will exhibit $2e$ periodicity with respect to Q_g. At the charge degeneracy point $\pm e$, $I_C^m(Q_g)$ reaches its maximum [65].

This charge modulation of the critical current of the sSET is dependent on the competition of E_J and E_C [66, 111]. Assuming both junctions are identical with a Josephson energy E_{J0}, if E_C is very small and negligible, the critical current is

$$I_C^0 = \frac{2\pi}{\Phi_0}E_{J0}\sin\frac{\phi}{2} \tag{2.65}$$

in the ground state. This result agrees with the calculation for two Josephson junctions in series where the total phase is split equally in half. Note that here, the charging effect is minor so that $I_C^0(Q_g)$ lost the gate charge dependence.

In the opposite case where $E_J/E_C \ll 1$, the maximum critical current at the degeneracy point is reduced to

$$I_C^0(\pm e) = \frac{2\pi}{\Phi_0}\frac{E_{J0}}{2}\sin\frac{\phi}{2}. \tag{2.66}$$

This is exactly half the value of equation (2.65). In the middle of two degeneracy points, the critical current minimum is

$$I_C^0(0) = \frac{2\pi}{\Phi_0}\frac{E_{J0}^2}{4E_C}\sin\frac{\phi}{2}. \tag{2.67}$$

As temperature increases, thermal fluctuations may wash out the supercurrent branch, resulting in a finite resistance due to phase diffusion. In practice, the measured switching current is much smaller than the theoretical prediction [102].

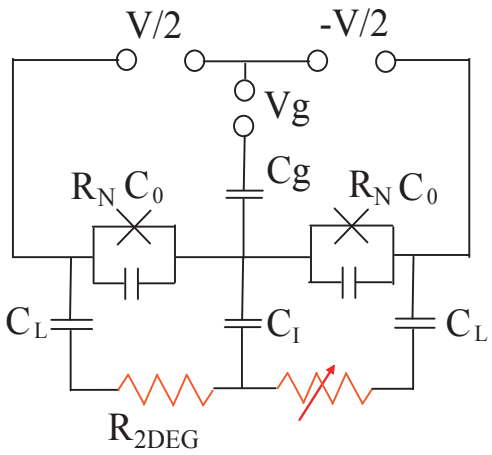

Figure 2.10: The circuit of a sSET capacitively coupled to a metallic ground plane. C_I is the capacitance between the island to the ground plane. C_L is lead capacitance.

In the high impedance limit, the phase ϕ does no longer behave classically and the supercurrent is destroyed by quantum fluctuations. As a consequence of the phase-charge duality, the sSET in the high impedance limit is well described by the charge dynamics. Instead of a supercurrent branch, the I-V curve shows a Coulomb blockade voltage which can also be modulated by the gate charge [69, 70, 111].

Similar to the single small junction in a high impedance environment, this double junction system can be described by the two dimensional Bloch band picture which is represented by two charge variables: $Q_{1,2}$ on the first and second junction respectively. In the limit $E_J/E_C \ll 1$, the total phase of the island ϕ is meaningless, while its conjugate variable, the total charge across the island, Q_ϕ, has very small level of fluctuations. This will cause the voltage on the sSET to be a function of gate charge with a periodicity $2e$ [111].

One special case of the dissipative environment is a two dimensional electron gas capacitively coupled to a sSET. The 2DEG sheet resistance, R_{2DEG}, can be tuned *in situ* while keeping other parameters unchanged.

The tunneling of Cooper pairs is dissipative because of the interaction with the normal metal imaging charges. Using $P(E)$ theory, Wilhelm *et al* calculated the effect of such a dissipative environment for a small E_J/E_C ratio [47], where different environments were considered. The equivalent circuit is sketched in Fig. 2.10.

The sequential tunneling rate of Cooper pairs through one junction is

$$\overrightarrow{\Gamma}(\delta E_{ch}) = \frac{\pi}{2\hbar} E_J^2 P(\delta E_{ch}). \tag{2.68}$$

This rate depends on the change in charging energy during the tunneling process, which in turn depends on the gate charge $Q_g = C_g V_g$ and the bias voltage V. If the excess Cooper pair number on the island is increased from n to $n+1$, we can get

$$\delta E_{ch} = -4E_C(2n - Q_g/e + 1) + eV. \tag{2.69}$$

The real part of the total impedance is the combination of R_{2DEG} and junction capacitance C_0

$$Re(Z_t(\omega)) = \frac{R_{2DEG}}{1 + (\omega R_{2DEG} C_0)^2}. \tag{2.70}$$

The function $P(E)$ can be calculated from the phase-phase correlation function $J(t)$ which is determined by this total impedance. By doing so for both junctions, the I-V characteristics can be obtained. Defining a dimensionless factor of dissipation $g \equiv R_K/R_{2DEG}$, for a low bias voltage and in strong damping regime where $g \gg 1$, the conductance is found to be $G \propto gE_J^2/T^2$ for wide, short leads which satisfy the condition $C_0, C_g \ll C_I \ll C_L$, where C_g is the gate capacitance, C_I and C_L the capacitances between the island and the leads to the metallic plane, respectively.

Another typical case is the long, narrow leads, which can be modeled as a RC transmission lines. The impedance is found to be $Z_{RC}(\omega) = \sqrt{R/i\omega C_{sq}}$ where C_{sq} is the unit square capacitance between the leads and the ground plane. The conductance has the power law with g, T as $G \propto g^{1/3}$ and

	superconducting SET	dc SQUID
Junctions	in series	in parallel
Configuration	island	loop
Modulation	charge	flux
Periodicity	*2e*	Φ_0=*h/2e*
Coupling	capacitive	inductive
Used as	electrometer	magnetometer
Environment	high impedance	low impedance

Figure 2.11: Duality between sSET and dc SQUID.

$G \propto T^{-5/3}$. The dissipation dependence of conductance has been proved to have a good agreement with the experimental result for comparable E_J and E_C [51]. The temperature dependence in the experiment, however, is found to be $\propto T^{-0.9}$. This discrepancy may come from the theoretical assumption of small E_J/E_C ratio, which is far from the experimental condition $E_J/E_C \approx 1$. Another measurement on a sSET in strong charging regime with small $E_J/E_C = 0.2$ has been shown to have a good agreement with the calculation in the Cooper pair co-tunneling regime [30].

2.2.4 Analog Between dc SQUID and sSET

As mentioned above, a single Josephson junction shows the duality of phase and charge in their favorite opposite environment: low and high. The sSET, with well-controlled Hamiltonian and small E_J/E_C, is dominated by the charge variable in a high impedance environment, showing a Coulomb gap voltage modulated by gate charge with a periodicity $2e$. The

nature of the tunneling of Cooper pairs is incoherent, i.e. phase variable has strong quantum fluctuations. A voltage biased sSET can be used as a very sensitive electrometer where Cooper pair tunneling is modulated by gate charge with a periodicity $2e$.

Compared to a dc-SQUID which has two large Josephson junction in parallel, there is a duality between these two different systems [112]. The voltage of a current biased dc SQUID shows a modulation by flux through the SQUID loop with a periodicity Φ_0, allowing the SQUID to function as a magnetometer with a very high sensitivity. Note that the coupling of the signal to the SQUID is inductive. The input impedance to a SQUID is extremely low. The sSET, however, favors a high input impedance with capacitive coupling. Indeed, the analog between these two devices can be understood by the electromagnetic duality transformation of $Q \longleftrightarrow \Phi$, $V \longleftrightarrow I$ and $C \longleftrightarrow L$, as shown in Fig. 2.11.

Both SQUID and sSET can be operated at high frequency for high speed measurements. For instance, a dc SQUID can be operated at microwave frequency via an inductively coupled resonant circuit, as a low noise amplifier [113, 114]. Similarly, a LC resonant circuit at high frequency can also be used in a high speed rf sSET electrometer, as a transformer from the high input impedance to the 50Ω coax line. The output signal is a periodic function of gate charge with a periodicity e for a normal state device and $2e$ for a superconducting SET [62].

Chapter 3

Experimental Methods and Circuit Model

In this chapter, we start with the experimental techniques in fabrication and measurement, including sample preparation, 2DEG resistance measurement, electron-beam lithography and double angle shadow evaporation. We then introduce the device characterization, circuit model, refrigeration and noise cancelation method. The problems happened in the measurement will also be discussed.

3.1 Sample Preparation

3.1.1 Substrate Description

We choose a GaAs/$Al_xGa_{1-x}As$ heterostructure as the substrate, where a two dimensional electron gas (2DEG) is located 100nm below the surface. The back side of the substrate can be attached to a gold coated silicon wafer. By applying a negative back gate voltage (V_{BG}), an uniform electric field is generated, for reducing the density of charge carriers with 2DEG. Thus, the 2DEG sheet resistance (R_{2DEG}) is a function of V_{BG}. Because of the capacitive coupling between 2DEG and the sSET circuit, the total shunting impedance seen by the sSET can be tuned *in situ*.

The heterostructure substrate was fabricated by Prof. Zbigniew Wron-

ski at National Research Council in Ottawa. The substrate was made by growing a layer of $Al_xGa_{1-x}As$ on top of a GaAs substrate using the molecular beam epitaxy (MBE) method. Typically, $x = 0.3$. The heterostructure consists of 500nm of GaAs, 94nm of $Al_{0.3}Ga_{0.7}As$ and 6 nm of GaAs from bottom to the surface. In the growing process, the $Al_{0.3}Ga_{0.7}As$ layer is selectively doped with Si donors located 40 nm above the lower GaAs/AlGaAs interface. This donor layer is used to trap the electrons at the GaAs/AlGaAs interface.

A conduction band offset of about 0.3V forms at the lower GaAs/AlGaAs interface due to a larger band gap of AlGaAs. As a result, a triangle potential well dips below the Fermi energy at the interface. Because the AlGaAs layer is usually electron-doped, some electrons are confined in the potential well and collected by the attractive electrostatic potential due to the positively ionized donors. To reduce the scattering from the donors, the dopant layer is separated from the interface by an undoped AlGaAs buffer layer. Usually, this interface has an atomic-scale thickness and the electrons are confined into a two dimensional space with the free motion parallel to the interface (see Fig. 3.1).

To prepare the substrates for later treatment, we cleaved the substrate into $3\times3mm^2$ squares and glued the surface to one side of a brass rod, for polishing the back side. A small amount of wax, melted on a hotplate, was used as the glue and a protective layer for 2DEG surface. The back side of the substrate was polished down to $\sim200\mu$m on an auto polisher, in order to obtain a larger tuning range of dissipation as V_{BG} was increased. In our experiment, the maximum back gate voltage was 600V. We put the thinned substrates into acetone for hours to dissolve the wax. Sometime, a longer time was needed for removing the wax on the side of substrate completely.

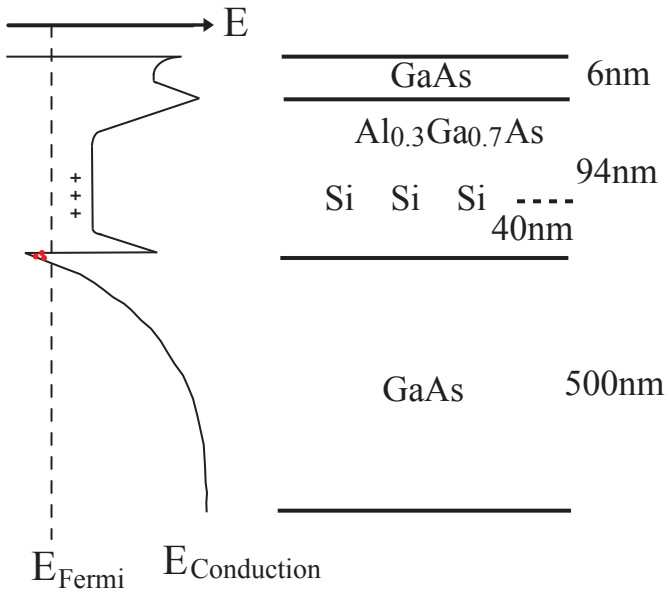

Figure 3.1: Physical structure and the conduction band of GaAs/AlGaAs heterostructure. A 2DEG is formed at the interface of GaAs and AlGaAs.

3.1.2 Ohmic Contact

A good electrical contact to the 2DEG is essential for a reliable measurement. Several methods can be used to make a good contact to the sub-surface electron gas. The technique we used is to make InSn alloy at the corners of the substrate [115]. The mechanism by which InSn makes a good ohmic contact is complicated and not well-understood. A possible explanation is that the alloy InAs (from InSn and GaAs) has an electron affinity to GaAs.

Typical steps for making an Ohmic contact included:

1. Clean sample with ultrasound in acetone and in isopropanol alcohol (IPA) for 5 minutes respectively, for removing any residue left on the surface. After the cleaning, use compressed air to blow dry.

2. Prepare InSn alloy on a clean microscope slide by melting 95% In and 5% Sn by weight (99.999% purity) using a soldering iron at about 700°F.

3. Press InSn onto the substrate surface using the soldering tip at 600°F. A good contact is a natural solder spot with a diameter ∼0.5mm. It may be necessary to press the spot down by tweezers if it is too tall.

4. Place the sample onto a copper heater in a home-made chamber. A thermocouple thermometer is used to monitor the baking temperature. Flush the chamber with a mixture of 20% H_2 and 80% He gas for 10 min to remove the air left inside. The gas flow rate is set to an optimal range, typically 100-150 ml/min.

5. Bake the substrate at 110°C for 1 min to remove adsorbed moisture on the surface.

6. Increase temperature to 400°C and keep the substrate at 400°C for 4 min.

7. Turn off the heater and leave gas flowing until sample is cool back to room temperature.

8. Test the Ohmic contacts at 4.2 K.

In these procedures, we treat the period at 400°C as the baking time, which is critical for making a good Ohmic contact. The starting point of the process of forming InAs is between 300°C and 400°C, thus the actual baking time will be a little longer. The Ohmic contact is made to a very thin electron layer, thus either too short or too long baking time will cause the contacts to fail. Baking time from 3 to 5 minutes worked well for our substrate with 2DEG 100nm below the surface. A typical baking procedure is shown in Fig. 3.2.

The chamber is a home-made $4\times4\times4in^3$ clear plastic box with gas inlet and outlet, and a rubber gasket seal. Two copper wires are attached to the ends of a 2Ω nickel-chrome heating wire which is held inside a copper block with ceramic insulation. The substrates are put on top of the heater and the temperature is monitored by a thermocouple with a accuracy of 1°C. The thermometer is attached to the heater surface close

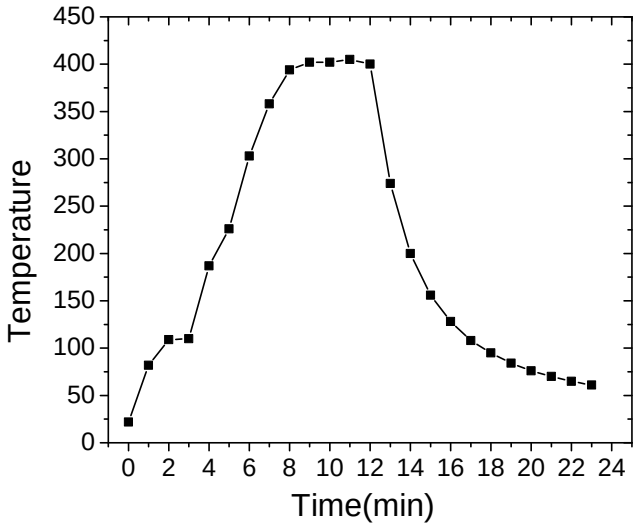

Figure 3.2: Typical baking temperature with time for making Ohmic contact. The duration of the plateau at 400°C is defined as the baking time.

to the samples. An ac current is applied through the wire for heating the 2DEG substrates up. Because of the heat capacity of the heater and a relative small amount of available heater power (∼30W), it takes about 4 minutes to increase the temperature from 100 °C to 400°C. This process is performed in a reducing gas atmosphere, where the H_2 is used to minimize the oxidation of the InSn alloy and the heterostructure.

3.2 Electron Beam Lithography

The electron beam lithography method has been widely used to make structures with a dimension less than 500nm. Unlike photo lithography, where the resolution is limited by the wavelength of light, the resolution of e-beam lithography is limited by the spot size of backscattered electrons from the substrate, which is mainly determined by the beam energy and

the substrate material. In our experiment, we used the bilayer photo resist coating to make the undercut for the double angle evaporation. The dimension of finest structures we could reach was 50nm.

3.2.1 Bilayer Resist Coating

E-beam lithography relies on the selective exposure of the photo resist which is sensitive to the relatively low energy electrons. For a positive resist, the electron beam breaks the bonds in the large molecular weight polymer. The weakened part of the resist has smaller weight and can be dissolved in the developer while the unexposed part remains. Thus, the unexposed area will be dissolved in the developer. The exposed part of a negative resist, however, will be hardened due to the formed bonds between different molecules. Because of the convenient design and higher spatial resolution, positive resist is more widely used.

Bilayer resist coating is commonly used because it is convenient for making an undercut during the process. The actual dimension of the structure is determined by the top layer only and the undercut in the bottom layer makes the lift-off step much easier. In our experiment, the coated lower molecular weight bottom layer is more sensitive to the e-beam than the higher molecular weight top layer. After the exposure, more bottom layer will be removed during the development, leaving a suspended top layer resist with a higher spatial resolution. The undercut profile is affected by the photo resist thickness and their different sensitivity to the electron beam. Thus, a proper combination of two types of photo resist is necessary for a desired undercut, shown in Fig. 3.3.

An alternative method is to choose a different type of bottom layer resist which is not sensitive to the electron beam and the developer. Thus the lithography procedure only makes the pattern on the top layer. After developing the top layer, the designed pattern is made on the bottom layer. Using a special solvent for the bottom layer only, the undercut can be made in a different process. This method has the advantage that the

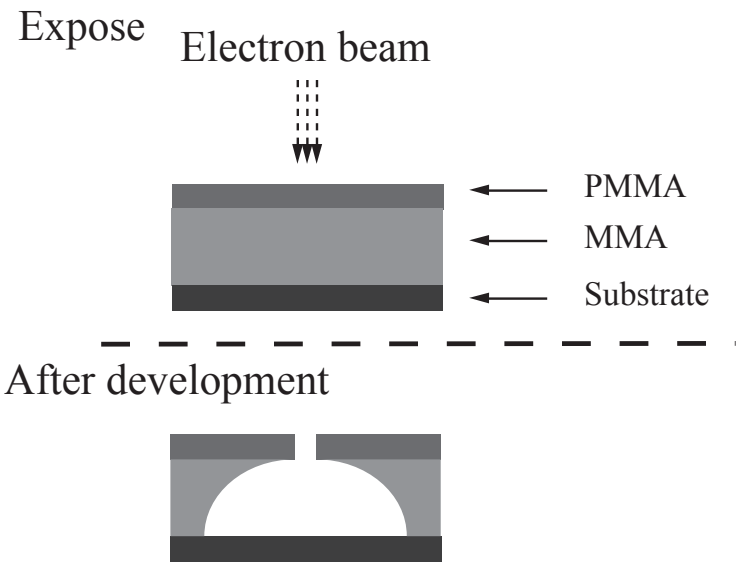

Figure 3.3: Schematic illustration of the exposure of bilayer resist coating in electron beam lithography.

exposure and development parameters can be determined separatively.

In practice, the bilayer method minimizes the chances of touches between the metal deposited on the resist and on the substrate because evaporation is directional so that no metal will be deposited inside the undercut. This ensures a clean edge of the pattern on the substrate. Moreover, the metal thickness is usually less than half thickness of the bottom layer resist. In this case, the lifting off can be finished easily by immersing the sample into the solvent. Increasing the developer temperature or using ultrasound will increase the developing speed. In addition, bilayer resist method also helps to increase the expose accuracy because the top layer is held further away from the substrate, which is a source of the back-scattered electrons.

Two types of resist we used were the copolymer MMA (methacrylic acid) for the bottom layer and 950K PMMA (polymethyl methacrylate, molecular weight 950K) for the top layer, both from MicroChem Corp.

MMA and PMMA were diluted to 8% in Ethyl Lactate and 2% in anisole respectively. The thickness of resist was determined by its concentration, spin speed, substrate size, distance from the spinning axis (only for small sample) and the temperature.

The typical sequence of steps in spinning was

1. Clean sample with acetone and IPA using ultrasound for 5 minutes in each process. Blow dry with compressed air.

2. Glue the sample to a 0.5×0.5 in^2 square copper plate (0.5mm thick) by a mixture of MMA and PMMA. One side of the sample is placed parallel to the edge of the plate and 1mm away.

3. Apply enough MMA (a couple of drops) to cover the entire sample. The spinner is ramped up to 200RPM at 1000RPM/min acceleration rate. After photo resist flows to the edge of the substrate, the spin speed is increased to 3000RPM and lasts for 45s.

4. Check for uniformity of resist and bake the sample on a glass beaker in the oven at 140°C fo 30 minutes.

5. Wait until the sample is cooled down to room temperature and measure the resist thickness at the sample center, on a Nanometrics NanoSPEC 210 system. Its resolution is better than 10nm. The thickness of MMA normally ranges from 260nm to 320nm.

6. Repeat step 3 to 5 for 950K PMMA with a spin speed of 4000PRM. The baking temperature is set to be 170°C. PMMA thickness is 100 ± 10nm.

The substrate was put close to one side of the copper plate for the evaporation. Considering the surface tension of the resist on the substrate edges, the thickness of both resist layers were not uniform over the sample after the spinning. The thickness increased along the longitude direction from the spinning axis. This effect was less significant for the PMMA layer because of its higher viscosity. We only measured the resist thickness at the center where the finest structure (the Josephson junctions and island) was located. The 25μm diameter focus point was moved to the center by eye. In practice, the area with 1mm^2 at the center has the same thickness of the resist. There was always about 10% difference in the bilayer resist

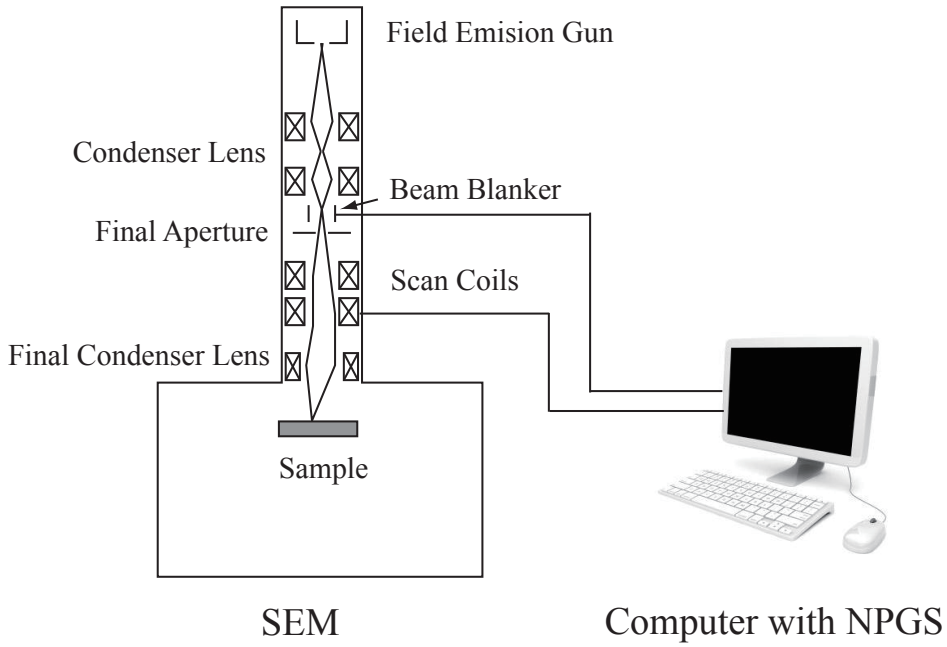

Figure 3.4: A conventional scanning electron microscope converted to an electron beam writer. The computer is equipped with a commercial package, the Nanometer Pattern Generation System (NPGS), which interprets CAD drawings to perform an exposure via controlling the scan coils and a Raith beam blanker.

thickness, but this was just a minor problem affecting the final lithography results. The electron beam exposure time was adjusted for different samples. In general, we only chose the samples with 300±15nm MMA and 100±5nm PMMA for the exposure.

3.2.2 Pattern Generation System

A pattern generation system was used to control a LEO 1530 scanning electron microscope (SEM). This nanopattern generation system (NPGS) and the hardware were obtained from J. Nabity's Lithography Company. The principle is illustrated in Fig. 3.4. The pattern generation (PG) includes pattern design, run file creation and pattern writing.

A pattern was firstly drawn using a CAD program, defining different objects with different colors and layers. The exposure conditions for the different elements of the pattern were put in the run file which controls the exposure parameters, such as the order of exposure, spot and line spacing, the beam current and dosage. To perform an exposure, NPGS used PG to access the information stored in the run file and communicate with the LEO 1530 SEM, controlling both x and y of the beam position within the field of view on the microscope. Note that different magnifications have different fields of view. The beam blanker was biased at a positive voltage (50V) at the same time to deflect the electron beam from reaching sample. The role of blanking the electron beam is to control the exposure time and hence the dosage received by the resist. It also helps to avoid any exposure when moving the sample or changing the SEM settings.

3.2.3 Exposure of Sample

The exposure is the critical step for creating the shadow mask and the junction dimensions. The major steps were as follows:

1. Load the substrate, Faraday cup and high resolution gold on carbon sample.

2. Ramp up the SEM to the desired accelerating voltage (20kV in our case) and get the image of the gold particles (dimension $\sim$10nm). Optimize the focus, aperture alignment and astigmatism for all apertures until the clear gold spheres are seen.

3. Switch to the Faraday cup and measure the beam current for all apertures used in exposure. Beam current could be adjusted $\pm$5% by

changing the extract voltage on the field emission gun.

4. Switch to the sample and find the corners of the copper plate which determine the rotation angles. This is a necessary step since the later evaporation step is aligned to the copper plate.

5. Find four corners of the 2DEG substrate and carefully focus on the upper edge. The working distance (WD) for exposure will be the averaged value of four corners.

6. Turn on the beam blanker and move to the center of the substrate. Adjust the WD and the rotation.

7. Use the NPGS program to adjust the run file setting with the measured beam current.

8. Switch the SEM to the appropriate aperture and magnification for the finest structure and run NPGS to expose.

9. Change apertures and magnifications as needed in order to expose the whole pattern properly.

10. Once the exposure is done, move the sample far from the beam line, even when the beam blanker is kept on. Turn the accelerating voltage back to zero and shut down the SEM.

In our samples, the finest features were written using the 10μm aperture at a magnification 1500×. The leads and bonding pads were written with the 120μm apertures at a magnifications 100×. The beam current was adjusted to be about 40pA and 5.0nA for 10μm and 120μm apertures respectively. If necessary, an intermediate aperture (30μm or 60μm) could be used to write some buffering structures.

Because the smallest structure is ∼50nm wide, it is necessary to set a small spot size and step size in the run file. This ensures that the edge of the exposed structure is smooth and straight enough. A smaller aperture setting also has a larger depth of field, compensating the error in working distance measurement (when focusing on the substrate edge, ±30μm will not make any noticeable difference in the exposed image). We over exposed the pads (250μm×400μm) so that all these large features can be exposed completely.

The scattered electrons could travel up to 1μm distance before they lost their energies inside the resist. Thus, every exposed point is affected by the surrounding circular area with a radius 1μm. For a very narrow linear structure, the center has a different exposure condition from the end. Thus, for the smallest features, this issue has to be taken into account. In our case, the upper and lower junctions have different exposure dosage. By adding the compensating exposure structures to the lower junction for increasing its actual dosage, we were able to obtain the same exposure condition for all junctions.

Since the substrate and resist are highly resistive, over-exposure may leave more electrons inside the resit, causing the incoming electrons to be deflected. In addition, there will be more chance for the arrived electrons staying at the same spot for large beam current, affecting incoming electrons. This effect is crucial for small structures. Thus, proper dosage setting and small beam current are necessary for exposing a fine structure with size $<$100nm. The critical energy needed to expose a volume of positive resist is dependent on the incident electron energy, resist thickness and substrate material properties. The adjustable parameters in the exposure are beam current density and the exposure time, which are determined experimentally.

After exposure, the sample was removed from the SEM, ready for development. We used a 1:3 mixture of Methyl Isobutyl Ketone (MIBK) and IPA as the developer. The sample was put in this developer for 45s at room temperature, followed by a rinse using IPA for 60s. Immediate blow drying prevented any residue from being left on the surface. A careful check under an optical microscope (1000$\times$ magnification) gave us enough information of the quality of the large features and a rough idea of the exposure condition of the structure with size $\sim$100nm. Under or over-exposure can be identified from the size of undercut ($<$0.5μm) through the transparent top layer PMMA. Fig. 3.5 shows a SEM image of a developed sample with 10nm gold coating. When taking this image, the electron beam was scanning on the surface, causing the resist under the

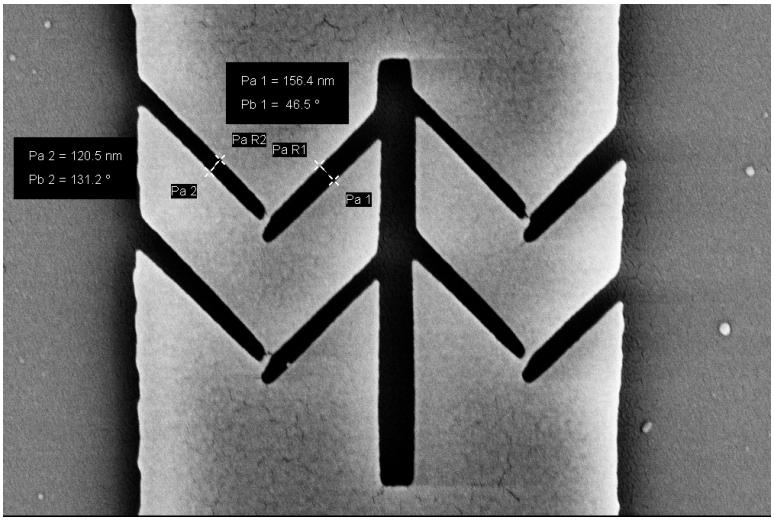

Figure 3.5: A scanning electron microscope image of a developed sample. The line width is much wider than the final dimension of the evaporated Al film.

Au film to be exposed slowly. Thus, the width of the narrow strip becomes wider than the actual dimension of the exposed sample. If all appeared good, the sample was ready for the evaporation and lifting off process.

3.2.4 Shadow Evaporation

Shadow evaporation is a standard process for making ultra-small Al-Al_xO_y-Al junctions [116]. The shadow mask is created by exposing two narrow lines separated by a small gap. This top layer mask is suspended above the connected undercut underneath. A junction can be fabricated by evaporating Al from one direction, oxidizing the surface to create insulating barrier, and evaporating the second layer from the opposite direction. The junction is located at the overlap of the two Al layers, as illustrated in Fig. 3.6. The width of two Al arms determines the junction area. The resist thickness and the evaporation angles determine the shift between two layers of Al. In our case, the thickness of bilayer resist is 300+100nm. Two Al sources are separated 16 inches away,

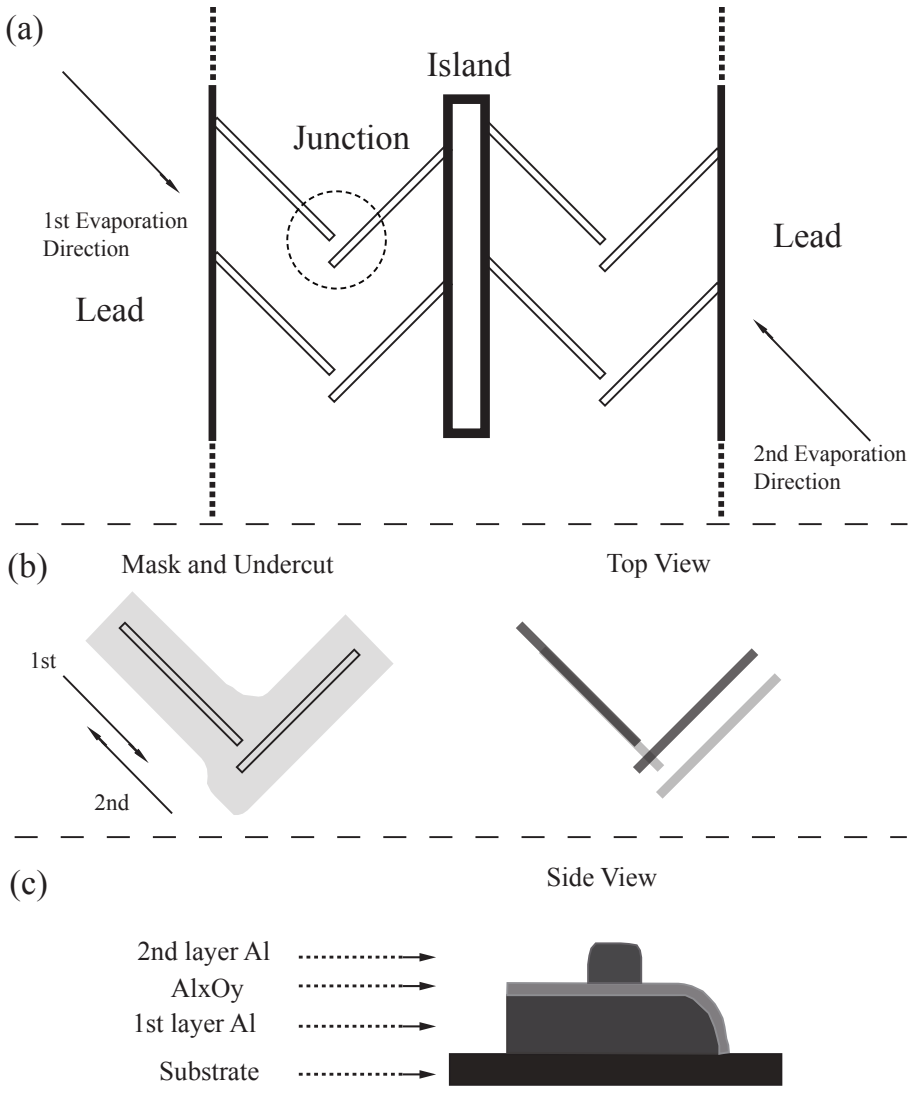

Figure 3.6: (a) The central region of the sSET mask. (b) Details of the junction area. Left: Top layer of the mask with the undercut. Right: Top view of the junction structure after two evaporations from opposite directions. Junctions are formed at the overlays of two perpendicular arms. (c) Side view of the Josephson junction structure.

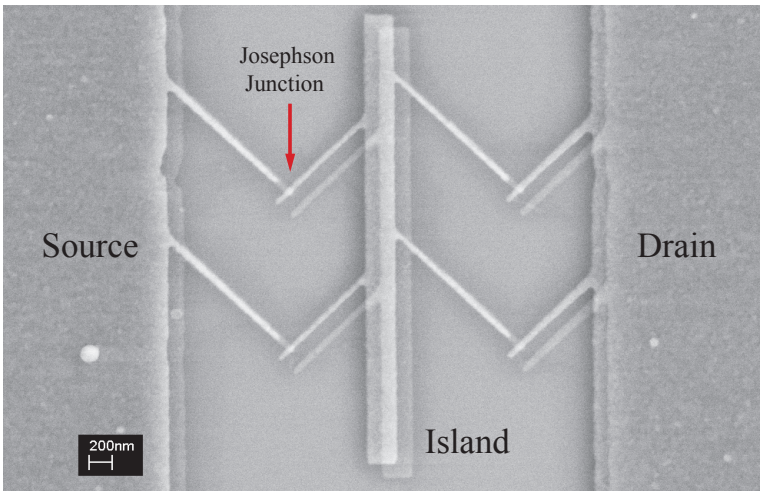

Figure 3.7: A scanning electron microscope image of a sSET.

and the substrate is placed facing down to the middle of two Al sources, 30 inches away. This causes two deposited Al thin films to be shifted 180nm away. Considering a ~50nm wide "bridge", it is safe to make junctions with a dimension up to 100nm. By increasing the photo resist thickness or rotating the substrate, the shift can be increased significantly, for fabricating the Josephson junctions with a much larger size. This large shift even allows the fabrication of more complicated structures such as three angle evaporated junction devices [30, 53].

Evaporation was finished in a thermal evaporator with a film thickness sensor located very close to the substrate. The vacuum system includes a mechanical pump and a diffusion pump with liquid nitrogen cold trap, to prevent oil vapor from diffusing back into the chamber. An optional liquid nitrogen cold trap in the chamber can also help to minimize the water vapor pressure inside. Typically, a vacuum below 8×10^{-7}Torr can be achieved after pumping overnight.

First, high purity aluminum (99.9%) wires were placed in two tungsten baskets firstly. The current through the tungsten was ramped up slowly

until the constant deposition rate (1nm/s) was reached. After finishing the first layer, a gate valve was close. The oxidation was done by introducing a mixture of 10% O_2 and 90% He gas into the chamber. Normally, 100 to 400 millitorr pressure was used for 1 to 5 minutes. Smaller pressure for less time was difficult to control and would bring more uncertainty on the quality of the insulating barrier. The gas was then pumped out by fully opening the gate valve quickly. After pumping out the gas, the vacuum background (8×10^{-7}Torr) was reached in a couple of minutes. The second layer of Al was evaporated using the second Al source. The finished sample was left inside the chamber for at least 2 hours.

The thickness of two layers of Al films were ∼25nm and ∼45nm respectively. The thicker second layer ensures that the Al arm does not break when it is deposited onto the bottom layer. Lifting off was done by putting the sample into acetone at room temperature for 10 minutes. We did not use ultrasound, to avoid any chance of the evaporated Al thin films to be peeled off from the substrate. One example of the structure of our sSET is illustrated in Fig. 3.7. Each Josephson junction normally has a rectangular shape, although we design it to be a square.

Pump oil contamination, sometimes not obvious, can lead to a surprising result of the junction tunnel resistance R_N. It destroys the good quality of the naturally formed Al_xO_y insulating barrier. We have seen a couple of samples with dimension 80nm×80nm had 70kΩ and 78kΩ resistance. We think this was due to oil contamination back into the chamber. Different oxidation parameters have been tested, as shown in Fig. 3.8. The normal state resistance R_N of the Josephson junction was inversely proportional to the junction area with a similar slope for three different pressures. We saw that 200-400 millitorr pressure of the gas was suitable for our fabrication. Smaller pressure will cause a very thin insulating barrier, even a shorted junction. The consistent data in Fig. 3.8 was taken over a couple of years on different substrates: Si, GaAs and 2DEG. Several data points with much higher resistance (>70kΩ) are not shown.

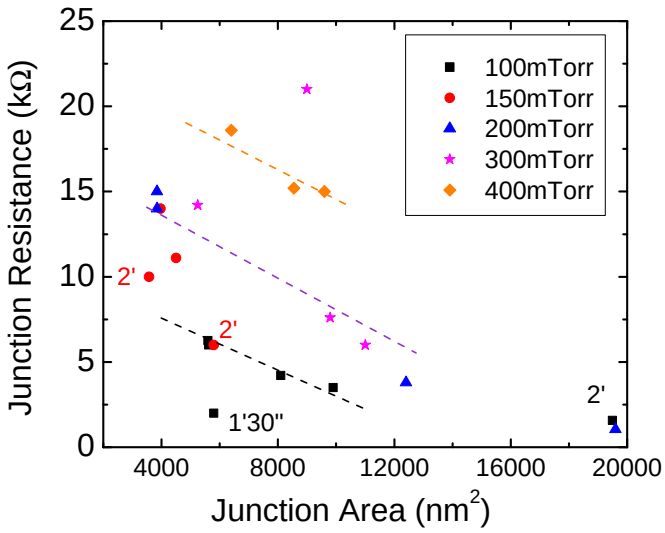

Figure 3.8: Normal state Josephson junction resistance of a set of devices with different oxidation parameters. Oxidation time is 3 minutes except for four labeled data points. Dashed lines are guides for different pressure and oxidation time.

3.3 Device Description

In this section, we show the 2DEG ground plane properties, the capacitive coupling between the sSET and 2DEG, the circuit model and the *in situ* tunable dissipation.

3.3.1 The sSET

As in Fig. 3.7, the overlaps of the perpendicular arms form four Josephson junctions. In fact, the oxide layer is all over the device between two layers of Al. The central island, the leads and bonding pads are effective large junctions with much larger critical current. They are acting as superconducting shorts (no junction effect) at low bias current and voltage. Our sSET consists of two dc-SQUIDs in series and a gate electrode (2DEG)

capacitively coupled to the central superconducting island. The width of the island ranges from 250 to 400nm and the length is from 2 to 4μm, causing a different gate capacitance. The source and drain are 10μm wide and 600μm long, split into two leads to voltage and current bonding pads at each end. The bonding pads are 250μm×400μm rectangles.

Our device have safety shorts connecting two voltage pads across the sSET, for protecting the junctions from being destroyed since small junction with high resistance (>1kΩ) is extremely sensitive to electrostatic discharges. It was necessary to work on the anti-static pad, using ionizing fan to neutralize the devices and the working environment. The safety short was cut using a specially made tool, just before the device was moved to the dilution refrigerator. Wire bonding did not work for aluminum pads because of the natural Al_xO_y oxide surface. We used a piece of indium metal to press a gold(99.9%) wire (25μm diameter) to the pads. Both the pads and metal must be very clean in order to have a small resistance and a reliable connection for thermal cycling. In practice, we could make the dimension of the pressed metal to be smaller than the size of the pad: 150μm. For the Ohmic contacts, it is easy to press the wires into the InSn alloy spots.

The device was glued onto the back gate using diluted GE varnish so that the distance from the 2DEG to the back gate wa as small as possible. A negative back gate voltage (V_{BG}) can be applied, in order to generate a uniform electrical field to the 2DEG. The density of the charge carriers in 2DEG decreases as V_{BG} is ramped up, causing 2DEG sheet resistance (R_{2DEG}) to be increased. The total circuit impedance also increases with V_{BG}. The sample, together with the back gate, was then glued to a sample holder with a 8 pin quick connector, which was made of copper. After pressing the wires to the bonding pads and Ohmic contacts, we moved the sample to the *S.H.E.* dilution refrigerator (base temperature ∼15mK).

An actual experimental setup on the fridge is shown in Fig. 3.9. The sample holder was screwed to a copper plate, attached to the rf-tight copper cylinder cover, which was thermally anchored to the mixing

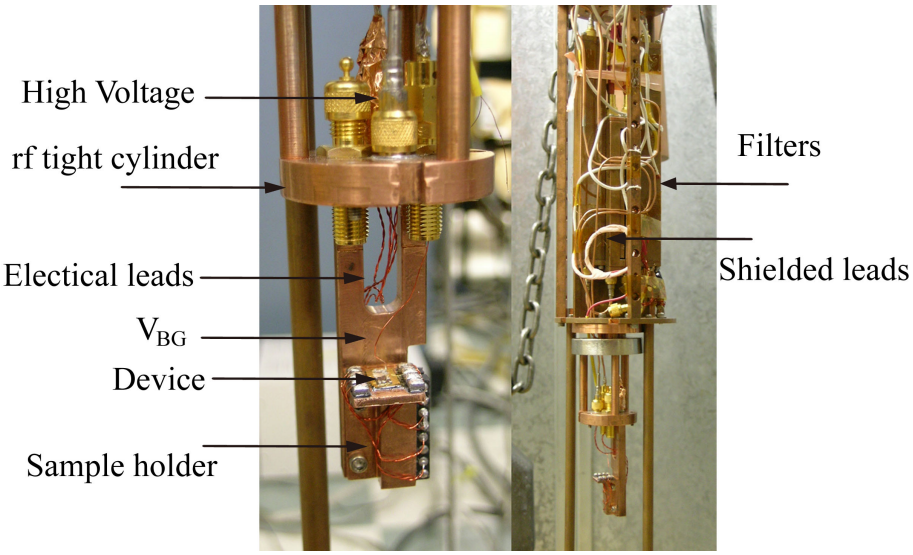

Figure 3.9: The device on the dilution refrigerator.

chamber on the fridge. The cylinder with a superconducting solenoid outside (not shown in the figure) was screwed to this cover after putting the sample on. Inside this copper cylinder, we put a layer of copper powder (30μm size) to absorb any reflected high frequency noise.

A 5cm long solenoid, which contains 3000 turns of NbTi superconducting wire, was wound outside of the copper cylinder. A uniform magnetic field was produced along the z direction. Our device was designed to be located at the center of the solenoid, perpendicular to the magnetic field. Considering the small dimension of two dc-SQUIDs (1μm$\times$1.8μm) and their close location, we believe that the flux through the two SQUID loops was identical. The flux actually is partially focused by the relatively large superconducting thin films (the leads and island). A 0.5 mT magnetic field was needed to produce $\Phi_0/2$ through the loop. All thermal connections were made through copper to copper, from the mixing chamber to the sample holder, so that the thermometer on the mixing chamber was reading the real temperature of the device. All electrical leads running from the filters to the sample were well shielded inside a copper tube.

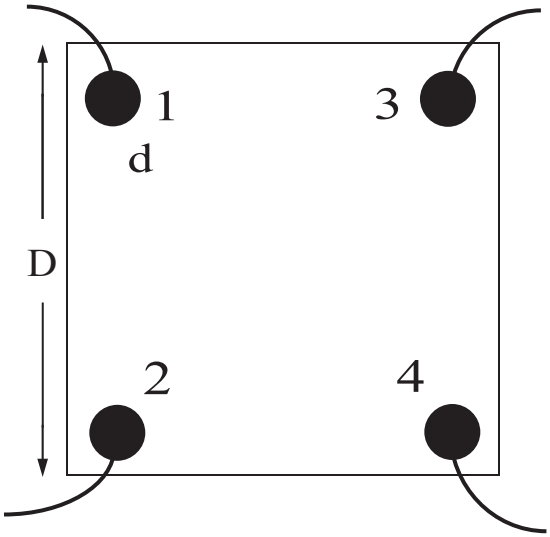

Figure 3.10: Configuration of van der Pauw method used to measure the sheet resistance of the 2DEG. Black dots are the ohmic contacts.

3.3.2 Sheet Resistance of 2DEG

The 2DEG substrate was characterized on a probe at 4.2K after making the Ohmic contacts. High voltage was applied through a 0.085 inch coax line in series with two low pass filters to the back gate. We used Van der Pauw method [117] to measure the sheet resistance of the 2DEG. As shown in Fig. 3.10, it is a four-wire measurement in a current bias configuration. We used a Stanford Research System SR830 digital lock-in amplifier as the voltage source and voltmeter. A small, low frequency ac current (on the order of μA and below 30Hz) was applied through a current limiting resistor (1MΩ) to two adjacent Ohmic contacts. The voltage across the sample was measured across the other two Ohmic contacts. For an approximate square sample, the sheet resistance could be calculated as

$$R_{2DEG} \approx \frac{\pi}{\ln 2} \frac{R_{12,34} + R_{13,24}}{2} \tag{3.1}$$

where $R_{12,34} = V_{34}/I_{12}$ and $R_{13,24} = V_{24}/I_{13}$.

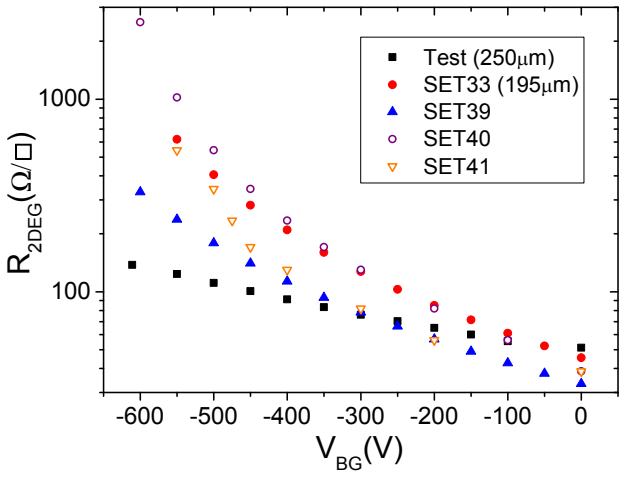

Figure 3.11: 2DEG sheet resistance as a function of back gate voltage with different substrate thicknesses.

The Ohmic contact should be made very small and placed to be close to the edge of the substrate. In our measurement, the error in R_{2DEG} was on the order of d/D, where d and D are the dimension of the Ohmic contact and substrate, respectively. We found that $R_{12,34}$ and $R_{34,12}$ were very close to each other, but $R_{12,34}$ could be several times greater than $R_{13,24}$ for a specific sample due to its rectangular shape. The value of R_{2DEG}, however, was still calculated using Equation 3.1.

The tuning range of R_{2DEG} iss sensitive to the thickness of substrate. Fig. 3.11 plots R_{2DEG} as a function of V_{BG} for a test sample and several devices with different thickness values. As the substrate thickness is reduced down to 200μm, R_{2DEG} can be increased 10 times higher when V_{BG} is ramped to -600V. For a much thinner substrate, we saw a larger tuning range (SET#39). The specific R_{2DEG} data of each sSET will be shown in the next chapter.

Polishing the substrate to be thinner than 200μm would help to increase the tuning range of R_{2DEG}. In our experiment, it is appropriate to keep the 2DEG thickness ~200μm to avoid any damage in the later pro-

cessing steps. Moreover, as R_{2DEG} increases to 5k$\Omega/\square \sim R_Q/5$, the real part of the total impedance will not be a monotonic function of R_{2DEG} at the highest frequency (10^{12}rad/s), i.e. the dissipation can not be characterized by R_{2DEG} any more.

Lateral top metal gates can also be used for confining the electrons beneath the substrate surface, for tuning a local environment coupled to a sSET or creating a quantum dot device [56, 118]. The advantage of this method is the larger tuning range of R_{2DEG} obtained by applying a small voltage (on the order of a volt). In this case, a low temperature filter can be used to reduce the high frequency noise at the gates. However, it is hard to characterize the 2DEG in such a system quantitatively. In our experiments, we have the advantage that R_{2DEG} could be determined experimentally while the measurement was carried out. Moreover, the electron layer, which contribute to the dissipation, see an uniform electrical field because V_{BG} is applied to the large back gate all over the substrate.

In addition, noticeable telegraph noise may exist in this heterostructures substrate with top gates. Because of the small distance between the gate and 2DEG, electron can tunnel through the Schottky barrier under the gate into the conduction band, and possibly be trapped near the active region of the device [119]. These stochastic processes can be reduced by applying a positive bias voltage to the gates while cooling the sample. When the density of ionized donors is decreased, the tunneling rate and hence the noise level are significantly reduced. We tried this bias cooling technique and applied V_{BG}=200V in cooling down the sample, but did not see any improvement in the noise cancelation in the switching current measurement. This may be due to the large gap between the 2DEG layer and the back gate, which reduces the possibility of the random tunneling of electrons. Using this bias cooling method, an offset back gate voltage may be frozen inside the sample, increasing the effective tuning range of R_{2DEG}.

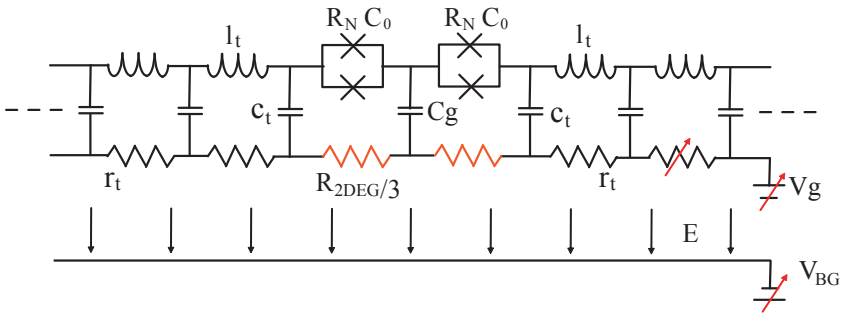

Figure 3.12: Diagram of the sSET coupled to the 2DEG ground plane acting as the gate electrode. R_N and C_0 are the junction resistance and capacitance. C_g, V_g and V_{BG} are the gate capacitance, gate voltage and the back gate voltage, respectively. The leads are modeled as a transmission line characterized by unit capacitance c_t, inductance l_t and resistance r_t.

3.3.3 Lossy Transmission Line

The leads connecting the bonding pads to the SQUIDs have length $l = 600\mu$m and width $w = 10\mu$m. The distance between the leads and the 2DEG grounding plane is d=100nm. Thus, it is appropriate to model the thin, long leads together with the capacitively coupled 2DEG as a microstrip transmission lines.

As shown in Fig. 3.12, we neglect the fringing effects of the electric and magnetic fields for the large ratio of $w/d = 100$. The distributed capacitance between the leads and 2DEG is $c_t \approx \epsilon_0 \epsilon w/d = 10^{-8} F/m$, where $\epsilon \approx 12$ is dielectric constant of $Al_{0.3}Ga_{0.7}As$. The permeability of $Al_{0.3}Ga_{0.7}As$ is $\mu \approx 1$, thus we estimate the inductance per unit length $l_t \approx \mu_0 \mu d/w = 10^{-8} H/m$. The resistance per unit length of 2DEG can be calculated to be $r_t \approx R_{2DEG}/w$, which can be tuned by the back gate voltage. In our experiments, several samples had different tuning ranges because of their different thicknesses. As V_{BG} was increased to 600V, R_{2DEG}

increased up by one order of magnitude, causing the r_t tuning range to be improved from $3-4M\Omega/m$ to $30-40M\Omega/m$.

The impedance of the transmission line is highly dependent on frequency. Here, we are interested in the characteristic frequencies of the sSET dynamics. The first one is the Cooper pair tunneling frequency which is represented by the current through the device. Because the maximum bias current was kept ~10nA, the corresponding frequency was estimated to be as high as $I/2e \approx 3\times10^{10}$Hz or 2×10^{11}rad/s. As the sSET stays in the superconducting state, the phase particle oscillates at the bottom of one potential well at plasma frequency $\omega_{p0} = (2I_C\pi/\Phi_0 C_0)^{1/2}$, on the order of 10^{11}rad/s. The sSET can also enter into the phase diffusion branch with a small voltage, which ranges from hundreds of nV to μV, depending on the damping and temperature. According to the ac Josephson relation $d\varphi/dt = 2eV/\hbar$, the phase evolves at frequencies from 3×10^8 to 10^{10}rad/s. In addition, the intrinsic time constant of sSET for transferring Cooper pairs through the island is $R_N C_0 \approx 2\times10^{-12}s$, corresponding the frequency 5×10^{11}rad/s. Thus, the relevant frequencies are 10^8–10^{12}rad/s.

The complex impedance of an infinite transmission line is

$$z_t(\omega) = \sqrt{\frac{r_t + i\omega l_t}{i\omega c_t}} \tag{3.2}$$

For frequencies lower than r_t/l_t, from 10^{14} to 10^{15}rad/s depending on different r_t in our experiment, the transmission line impedance is dominated by the resistive and capacitive term

$$z_t(\omega) \approx \sqrt{\frac{r_t}{2\omega c_t}}(1-i) \tag{3.3}$$

Including the impedance of the large bonding pads z_p, the impedance of the actual leads with the pad is

$$z_t(\omega)_{lp} = z_t(\omega)\frac{z_p + z_t(\omega)\tanh\gamma l}{z_t(\omega) + z_p\tanh\gamma l} \tag{3.4}$$

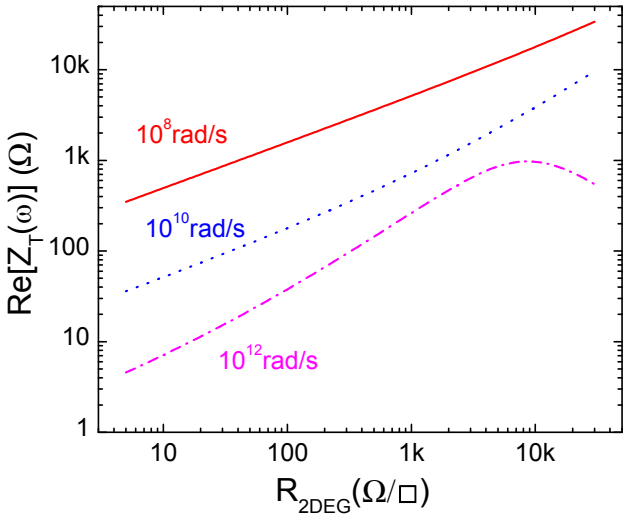

Figure 3.13: The real part of the effective total impedance shunting the sSET as a function of R_{2DEG} at different frequencies.

where $\gamma = \sqrt{(r_t + i\omega l_t) i\omega c_t}$. For the frequency $\omega > 10^8$rad/s in our experiment, $\tanh \gamma l \approx 1$. Thus, the effective impedance including the lead and pad is $z_t(\omega)$ in Equation (3.3).

3.3.4 The Effective Impedance of sSET Circuit

The total impedance shunting the sSET is the combination of the gate capacitance C_g, $R_{2DEG}/3$ which represents the 2DEG resistance between the island and the lead and the transmission line impedance $z_t(\omega)$ (shown in Fig. 3.13). Because one SQUID could effectively isolate the $z_t(\omega)$ and $R_{2DEG}/3$ from the other SQUID, we only consider half of the circuit to calculate the total impedance. The factor 1/3 in the 2DEG resistance is from the lateral spread of the current in the 2DEG from the island to the leads. Because the opened angle seen from the island is $\sim 125°$, thus the contribution of 2DEG resistance is $R_{2DEG}/3$.

The total effective impedance seen by one SQUID is written as

$$Z_T(\omega) = \frac{R_{2DEG}/3 + z_t(\omega) + 1/i\omega C_g}{1 + C_S/C_g + i\omega C_S(R_{2DEG}/3 + z_t(\omega))} \tag{3.5}$$

where $C_S = 2C_0$ is the SQUID capacitance. The real part of this impedance increases monotonically as R_{2DEG} is increased to 5000Ω/□ between the frequencies 10^8 and 10^{12}rad/s (see Fig. 3.13). Thus, the dissipation of the sSET represented by $Re(Z_T(\omega))$ is also a monotonic function of R_{2DEG}. We define the dimensionless dissipation factor as

$$g = \frac{R_K/4}{R_{2DEG}/3} \tag{3.6}$$

where $R_K/4$ is resistance quantum of a Cooper pair. Dissipation is a monotonic function of g from 4 to a maximum value of 650.

3.4 Measurement Technique

3.4.1 The Refrigeration

To observe the quantum properties of our devices, we need to lower the sSET temperature to be $T < E_J(0)/k_B, E_C/k_B$ to reduce the thermal noise. Both the $E_J(0)/k_B$ and the E_C/k_B of the samples range from 300mK to 700mK. All the measurements discussed here were performed on a *S.H.E. Corporation* DRP-36 dilution refrigerator with a base temperature ∼13mK, illustrated in Fig. 3.14. The lowest temperature in our measurement was 15mK after we reduced all possible higher temperature radiations. A detailed description of the mechanism of a dilution refrigeration can be found in Ref. [120]. Here we just give a brief introduction of the operation method.

A dilution refrigerator uses a mixture of ^{3}He and ^{4}He as the cooling media, unlike the normal evaporation cooling of pure ^{3}He or ^{4}He which can reach ∼0.3K or ∼1.2K respectively. If the mixture of ^{3}He/^{4}He with

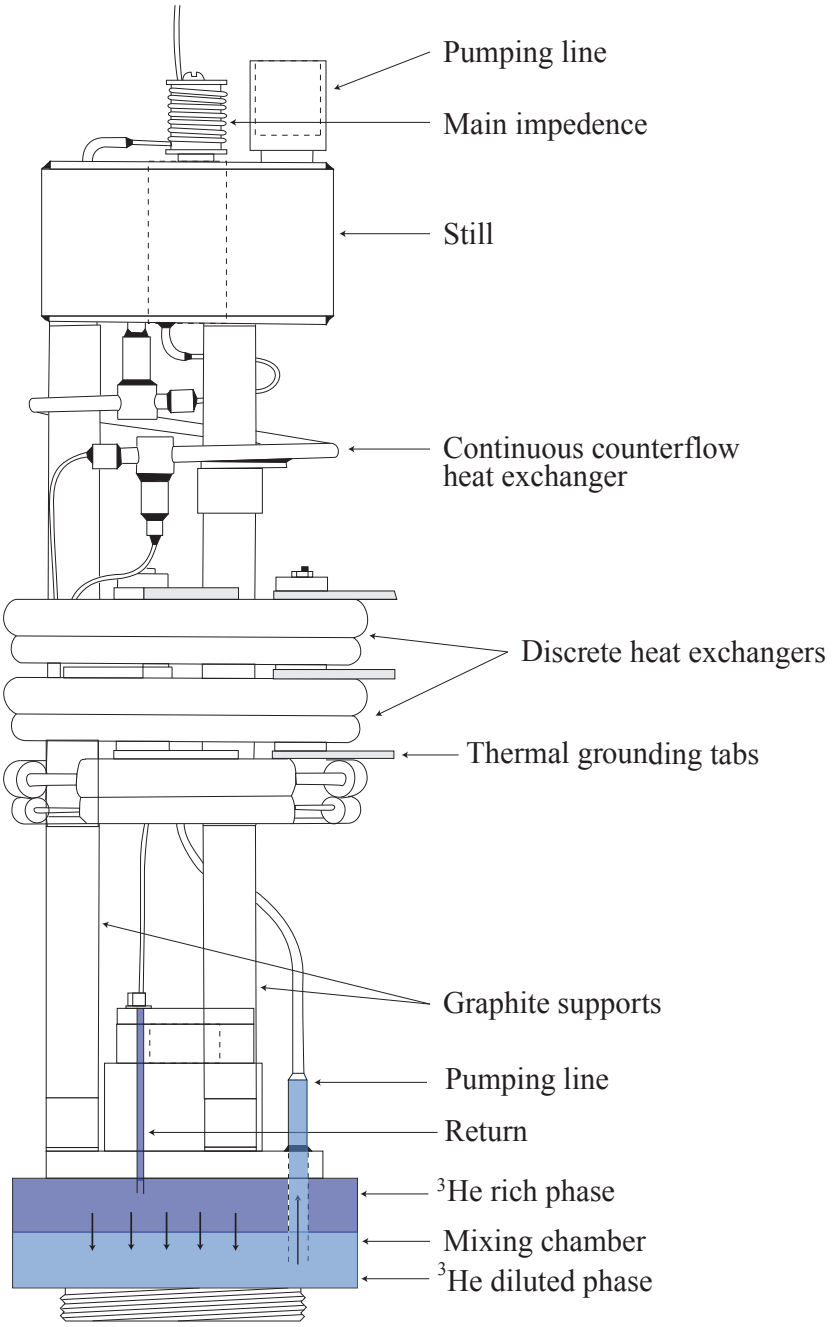

Figure 3.14: The diagram of the dilution unit in the *S.H.E. Corporation* dilution refrigerator used for the measurements contained in this thesis.

more than 6% ^{3}He concentration is cooled below 0.87K, it will separate into two phases: a ^{3}He rich phase on top and a diluted phase (^{4}He with 6% ^{3}He) at the bottom, until the temperature approaches absolute zero. Since the vapor pressure of ^{3}He is much higher than ^{4}He (1000:1), the vapor of the diluted phase will be almost pure ^{3}He. Pumping on the diluted phase results primarily in removing ^{3}He from the liquid. The unbalanced equilibrium is compensated by the diffusion of the ^{3}He atoms from the concentrated phase (see Fig. 3.14). The latent heat of ^{3}He is absorbed in this process when the atoms cross the phase boundary, resulting in a cooling process. This unique property of the mixture allows a very low temperature to be obtained if the mixture is continuously cycled.

On a dilution refrigerator, a phase boundary occurs in the mixing chamber which is the coldest part on this apparatus. However, the evaporation of ^{3}He is performed in another chamber called the still, at a higher temperature ($\sim$0.7K). The vapor pressure of ^{3}He could reach above a couple of millitorr at this higher temperature. This ensures a large circulating rate and cooling power. The separation of pumping and cooling at different temperature is the key for the continuous cooling to mK on a dilution fridge. ^{3}He is pumped out and sent back to the return of the refrigerator after it has been cleaned in a nitrogen and hellium trap. Through a large impedance and heat exchanger, ^{3}He gas is condensed back into the mixing chamber, finishing a closed cycle.

A proper design of heat exchanger is crucial for getting a very low base temperature and for having enough cooling power. By applying still heat, cooling power is increased because of the larger vapor pressure of ^{3}He at higher temperature. The temperature of the still can be 600-800mK. The pumping and return lines pass through the 1K pot, a ^{4}He evaporation unit running at 1.2K, to reduce the heat load to the refrigeration unit. The whole refrigerator is put inside a vacuum chamber which is immersed in a ^{4}He bath. The refrigeration unit is further protected by a copper radiation shield mounted on the 1K pot, to reduce the black body radiation from the ^{4}He environment (4.2K). The ^{4}He bath is stored in a standard dewar.

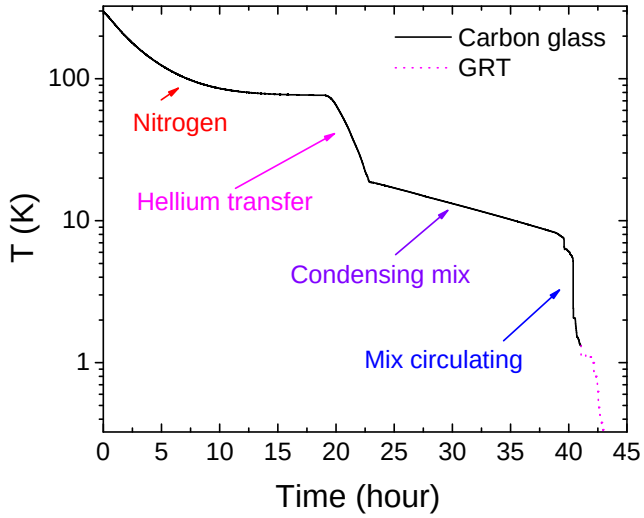

Figure 3.15: A typical cooling down process. Temperature is measured using a carbon glass thermometer from room temperature to 1.4K and a Germanium resistance thermometer below 1.5K .

We used several thermometers to monitor different temperatures on the fridge. A carbon glass resistance cryogenic temperature sensor on the mixing chamber was used when cooling the fridge. It is highly reproducible between 1.4K and 100K and can be used up to room temperature. Another calibrated Germanium resistance thermometer (GRT) was used to measure the mixing chamber temperature between 50mK and 3K. This is the main thermometer in our measurement. Below 50mK, it was calibrated by a ^{60}Co absolute radiation thermometer. Several Ruthenium Oxide thermometers were anchored to the 1K pot, still and heat exchanger to check their temperatures. We used a Lakeshore 370 AC resistance bridge with lock-in amplifier to measure the resistance of the thermometers. This apparatus was also used to apply heat to the still and mixing chamber. The temperature fluctuation at 20mK was approximately $\pm 10\mu$K.

As we mentioned above [119], the excited, free-moving charges inside the 2DEG substrate could induce low frequency noise. When cooling down

the sample, freezing those charges back to their lowest energy equilibrium state decreases this effect. Thus, the speed of cooling process is critical for the free charges to settle down at the freezing point, which is higher than 4.2K. Fig. 3.15 illustrates a typical cooling down process to base temperature. First, we put exchange gas (Ne) into the vacuum can and filled the dewar with 15L liquid Nitrogen. When temperature reacheed 77K, we normally did a leak check and then transferred the liquid Helium after blowing out the extra Nitrogen in the dewar. The cooling rate in this step was constant, ∼20K/hour. After the exchange gas freezed out at 20K, we quickly filled the dewar to full. Some He residue contained in Ne may cause trouble in controlling the fridge temperature, thus pumping out the He was essential before the temperature reached below 10K.

Following the condensation of the mix directly into the still through a bypass pipe, we started to circulate the mixture with the normal procedure. After phase separation happened, the cooling power increased significantly. Due to the decreasing heat capacity of all metal parts on the mixing chamber, the temperature droped quickly. The essential step was Nitrogen cooling because the free moving charges require some time to equilibrate. We slowed down this step by reducing the pressure of exchange gas to ∼700millitorr at the beginning. This increased the period of the first step from ∼8 hours to ∼15 hours. Note that even though the mixing chamber temperature was low, the actual temperature of the sample and the filtering system could be higher. We allowed two more days to cool the whole system down to base temperature, especially for the copper powder filter which was filled by low thermal conductivity epoxy.

3.4.2 Electrical Wiring and Filtering

To perform the measurement, twisted pairs were used to deliver low frequency signals to the sample. We had 12 pairs of wires running through a 25 pin sub-D hermetic connector into the fridge. 0.005" manganin wires were used from room temperature down to 1.2K because of the low

thermal conductivity. NbTi superconducting wires were placed between 1K pot and the mixing chamber. Copper wires were used at base temperature, to make operations such as soldering and heat sinking easier.

Two 0.085" semi-rigid beryllium copper coaxial cables were used between room temperature hermetic SMA feed-throughs and 4.2K. They were connected to one foot long superconducting NbTi coaxial cables below this temperature, for high frequency signal or high back gate voltage. Standard 0.085" copper SMA cables were used after NbTi cables. All wires and coaxial cables were thermally anchored to 4.2K (He bath), 1.2K (1K pot), 700mK (still), 200mK (heat exchanger) and base temperature (mixing chamber) respectively, in order to reduce heat load and thermal noise on the conducting wire. To cool the inner conductor of the NbTi coaxial cables, we put them through several 1 inch long copper blocks at different temperatures. This lowered the inner conductor temperature efficiently through teflon dielectrics.

At low temperature, standard four-probe setup was used to measure the sSET and 2DEG substrate properties, respectively. Eight wires were split into two groups, soldered to two Quad connectors. After room temperature LC filter, RC π filter and copper powder filters at base temperature, all the wires went into the rf-tight sample container. Then, eight wires were divided into four pairs and soldered to a female eight pin quick connector. This connector was glued onto a copper plate which was screwed onto the container cover. On the sample holder, the eight pin male connector was connected to Indium solder joints. 25μm fine gold wires were used to be pressed on to the bonding pads of sSET and four Ohmic contacts. From the copper coaxial cable, the 0.01" copper wire was pressed to the gold plane (back gate) using a piece of Indium.

The electrical connection to a sSET bonding pad was made by Indium pressing. A fresh cut indium cube ($\sim$100μm^3) was first pressed slightly to the pad. After sticking a piece Au wire on another indium cube, we pressed the wire into the first indium metal using a homemade tool. To make good low resistance and reliable contacts, the surfaces of the pad

and the indium must be very clean.

Electrostatics can cause serious damage during wiring and sample handling. A very small discharge can easily blow up the device by either burning the Al narrow arms close to the junctions or making pin holes in the thin oxide layer. We used several ways to reduce the chance of static charge damage:

1. 10 μm wide safety short across the sSET. It is cut by tweezers just before moving the sample to the dilution fridge.

2. Grounding all wire before connecting them to the sample.

3. Handling the sample on an anti-static pad.

4. Using an ionizing fan to neutralize static charges accumulated on the sample surfaces before pressing Indium on the sample pads.

It is critical that touching sample at the beginning because the charges accumulated on the insulating substrate will not be dissipated easily by other ways. Blowing the ionizing fan for one hour is needed. In practice, the sample holder was mounted on a larger metal block for stability. The working area was on one anti-static pad grounded to the dilution refrigerator. Grounding braid was used to ground the operator to the same potential reference. In transferring the sample to the fridge, all grounding wires needed to be connected together until the measurement is performed.

High frequency noise is a significant concern in low temperature, small signal measurements. Low electron temperature is obtained only via the thermal coupling to the substrate. The rf-tight container and the metal fridge body acts as a shield for high frequency radiation. However, all these means do not prevent the electromagnetic noise from equipment at higher temperatures from passing through the signal lines. Thus, an extensive filtering system is required to block these out of equilibrium noise entering into the system.

For a single electron or Cooper pair charging device, Vion *et al* have calculated the filters required to prevent high frequency noise which significantly affects the single charge tunneling [121]. For a large effective

impedance seen by the sSET, a stronger noise attenuation is needed. In general, the experimental setup must have more than 150dB power attenuation above 400MHz for a base temperature 20mK. Dissipative filter such as metal powder filter [84] or Thermocoax filter [122] is widely used in small Josephson junction circuits due to the absence of self resonance.

At room temperature, we used two LC filters with 1MHz cutoff frequency in series. The low temperature filters include one two-stage RC Π filter and one copper powder filter. In the RC filter, each channel has three low temperature 5.1nF capacitor soldered to ground and two 3kΩ metal film resistors in series. The dimension of this filter is $0.4\times1\times6\text{in}^3$. The copper powder filter consists of a $0.65\times0.65\times6.5\text{in}^3$ Cu block with four taped holes (diameter 0.15in) and two Quad connectors at each end. One rod (0.06inch diameter) was firstly made of the mixture of low viscosity Stycast 1266 and naturally oxidized copper powder (grain size $\sim30\mu$m). The volume and weight ratio were 1:1 and 2:1. We then wound a 250 turn spiral coil of 0.005" manganin wire around the rod. After putting the rod with coil into the hole, we filled the hollow space with the same mixture. The total length of the wire was 2.3m. The mechanism of noise attenuation is the eddy current within the small skin depth which can dissipate high frequency noise due to the high resistance.

Each signal line in RC filter and powder filter was separated by metal to prevent crosstalk between different channels. The filters were tested at room temperature and 4.2K. A RC filter has more than 140dB attenuation above 10MHz but a broad peak at 2.4GHz due to its self resonance. A powder filter has more than 120dB attenuation above 2GHz (see Fig. 3.16). Note that the attenuation is smaller at 4.2K because of the smaller skin depth at low temperature.

Filters were measured on a spectrum analyzer with noise floor -120dB. With 20dB input, we are able to see 140dB power attenuation (the flat regions in Fig. 3.16). Copper powder filter starts to work at 1GHz, due to the small amount of copper powder contained in the mixture and short wire. We tried a different design which shows more than 100dB

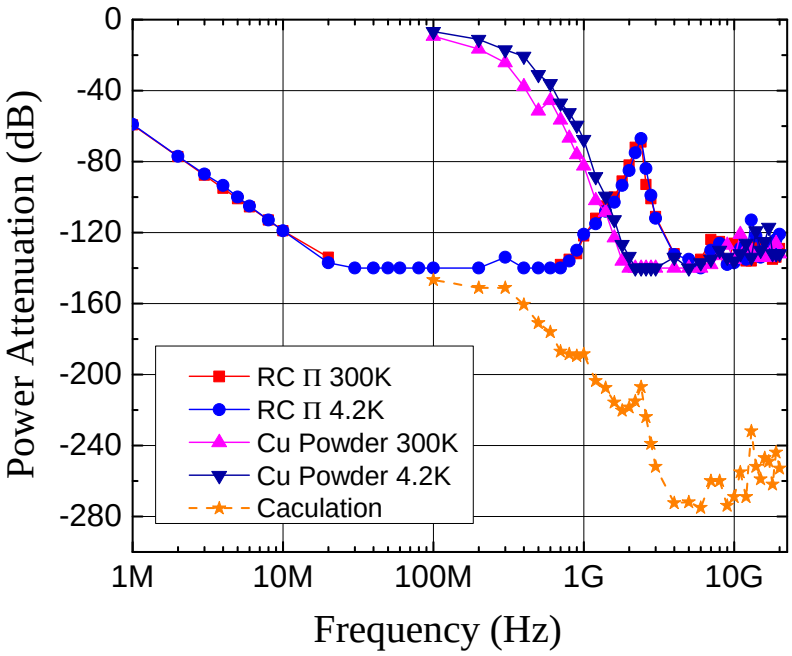

Figure 3.16: Power attenuation of RC Π filter and copper powder filter at room temperature and 4.2K. Calculation is the sum of the attenuations of two filters. Flat regions of the data are the noise floor of the spectrum analyzer (140dB).

attenuation above 200MHz, however, it caused other problems in our measurement. Above 2GHz, the powder filter goes deeply into the noise floor, compensating for the attenuation peak of RC filter. The actual performance was better than the calculation, i.e. at least 170dB power attenuation from 400MHz to 20GHz. Different metal powders have been tested to compare the low temperature performance of the filters [123]. Stainless steel powder filter has larger attenuation than copper powder because of the higher resistive surface. Considering the better thermal conductivity, we still chose the copper powder to make our filters.

To reduce very low frequency and dc electromagnetic noise, we used one room temperature Mu-metal (high permeability nickel-iron alloy)

shield and three cryogenic Mu-metal layers. In addition, the copper radiation shield attached to 1K pot was electro-plated with a layer of lead. Once the lead becomes superconducting, it can attenuate the static electromagnetic noise. Thus, we have a very clean environment suitable for the low noise measurement.

We did not put any low temperature filter for high back gate voltage. Instead, two room temperature low pass RC Π filters in series were placed just before fridge. The first filter consists of two 100MΩ resistors and three capacitors. The large current limiting resistor ensure no large current can flow through the sample or fridge if the high voltage line is shorted somewhere inside the fridge. The second filter has two smaller resistors (50kΩ) with three 1μF capacitors to reduce the broadband white noise from the 100MΩ resistors.

Fig. 3.17 depicts the experimental configuration, except for the different current sources and voltmeter used in conductance and switching current measurement. Current or voltage leads were fed into the fridge through twin BNC cable to reduce the common mode noise. Large current limiting resistors were placed before the LC filter. The voltage output was amplified first by a PAR 113 amplifier and then sent to a high frequency universal counter or the BNC 2090 voltmeter. The dilution refrigerator was set as the ground reference, which could be floating or be the same as the building ground. Battery powered electronics were used to avoid 60Hz noise in the main power line. However, the temperature controller, lock-in amplifier and counter still used ac power with special filters. These 60Hz apparatus could be isolated from the ground reference. All experimental data was sent to the computer through a GPIB cable and two optical isolators, for blocking the digital noise.

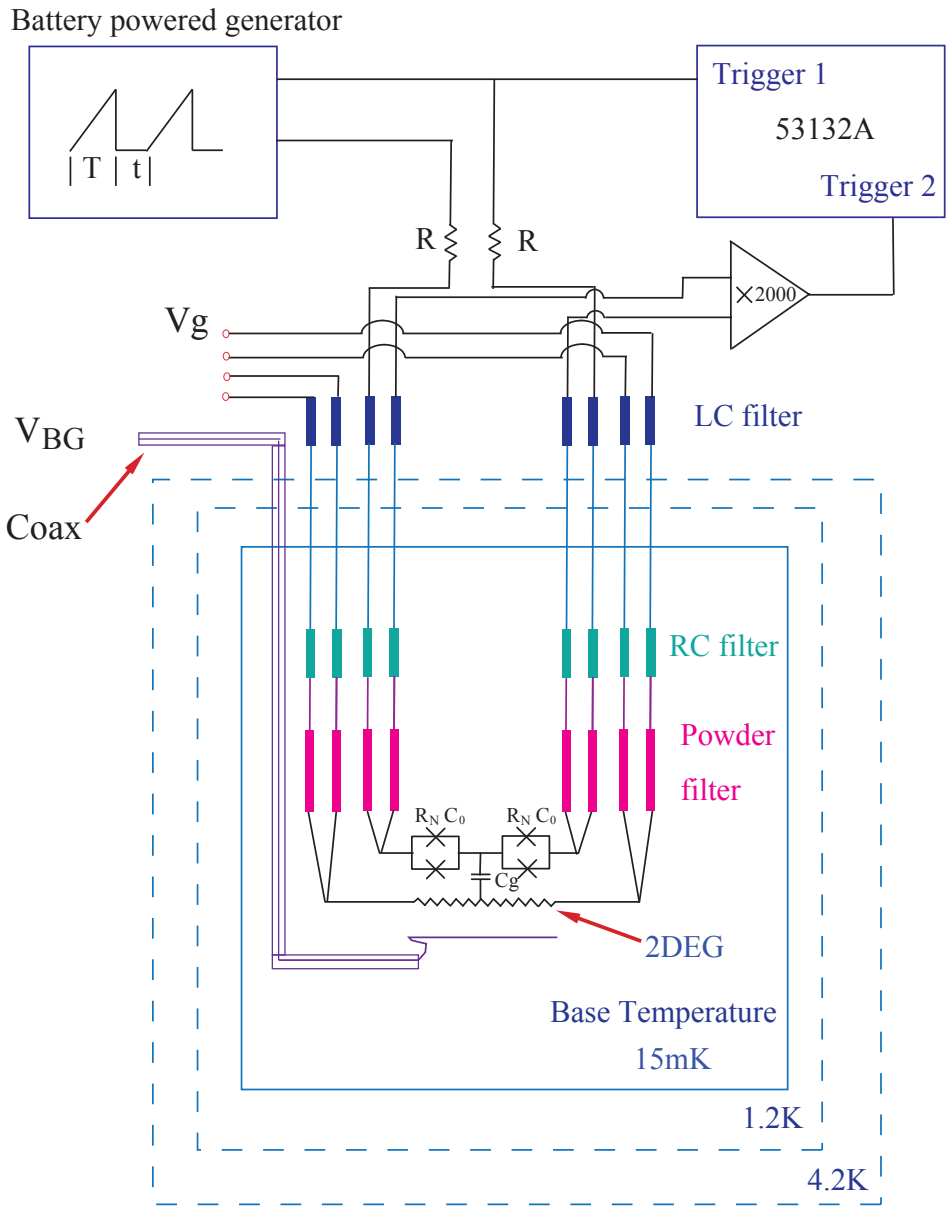

Figure 3.17: Experimental configuration in our measurement.

Chapter 4

Experimental Results

In this chapter, we will start with the characterization of the devices and the tunable Hamiltonian. Then we show the main experimental results for switching current (I_{SW}) on two devices, in the classical Josephson regime and the charging regime, respectively. I_{SW} was measured as a function of dissipation and gate charge at different temperatures, showing distinct behaviors in two different regimes. The results qualitatively agree with two different theoretical models of a classical junction and a sSET in the dissipative environment. The transport properties of a high tunnel resistance sSET show a $2e$ periodic function with respect to gate charge in the strong charging regime. Finally, we will discuss the effect of quasiparticle poisoning and phase diffusion in the measurement.

4.1 Description of Measurement

4.1.1 Device Parameters

Typical I-V characteristics are illustrated in Fig. 4.1 with different flux through the SQUID loop. The switching current I_{SW} is the maximum supercurrent flowing through the device. The sSET switches into the $2\Delta/e$ voltage plateau once bias current $I = I_{SW}$. As I increases continuously,

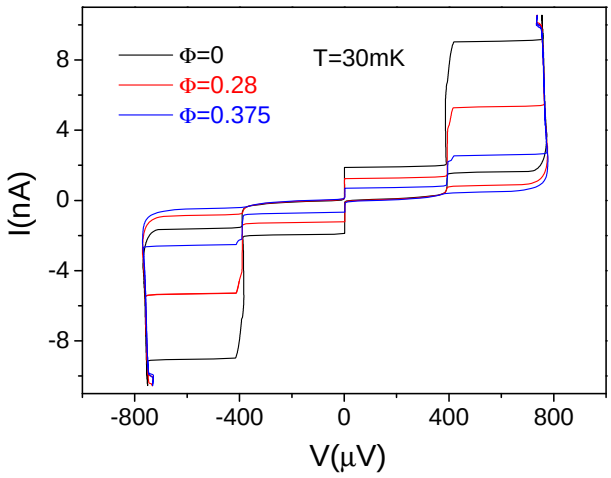

Figure 4.1: I-V curves of sSET#41. T=30mK, g=532. Two voltage states are $2\Delta/e$ and $4\Delta/e$.

the sSET switches into $4\Delta/e$ voltage states. The I-V curve then gradually evolves into the Ohmic behavior with a $1/R_N$ slope when current is ramped up further. As the bias current decreases, the sSET returns back to $2\Delta/e$ and then zero voltage state at a much smaller retrapping current I_r. When the sSET is in the finite voltage state, the dominant part of dissipation is governed by the low frequency impedance, which is on the same order of junction normal state resistance R_N. This low damping causes I_r to be much smaller than I_{SW}.

We obtained R_N of the SQUID from the slope of I-V curve above the transition temperature, at 2K with zero magnetic field. Here all four Josephson junctions are assumed identical, having the same critical current and capacitance. From the SEM image and the measurement, we see the deviation from this assumption is less than 5%. R_N is also consistent with the linear fit of base temperature I-V curve at large bias current where the Ohmic I-V relation has the slope $1/R_N$. The critical current of the SQUID is calculated to be $I_C^0 = \pi\Delta(0)/2eR_N$, here $\Delta(0)$ is the superconducting energy gap at zero temperature.

Table 4.1: Parameters of three sSETs studied in this thesis. R_N, I_C^0 and E_J^0 are the normal state resistance, fluctuation free critical current and Josephson coupling energy of the SQUID at zero magnetic field. E_C is the charging energy.

Sample	R_N (kΩ)	I_C^0 (nA)	C_S (fF)	C_g (fF)	E_J^0/k_B (mK)	E_C/k_B (mK)	g	Regime
33	10.3	29	0.50	2.1	680	290	61.8-464	Classical
39	31.5	9.2	0.30	1.3	210	490	59-580	Charging
41	14.9	20	0.57	1.5	490	350	58.3-532	Charging

The SQUID loop is formed by two narrow superconducting arms, central island and the lead (see Fig. 3.7). Considering the small loop size (1μm×1.8μm) of the SQUID, its geometrical inductance is estimated to be <10pH [124]. The kinetic inductance of the narrow superconducting thin film can also be calculated to be <100pH. Thus, these inductances are not significant compared to the Josephson inductance of the SQUID, $L_J = \Phi_0/(2\pi I_C^0)$, which is on the order of 10nH. Thus, each SQUID can be seen as a single Josephson junction with fully flux dependent critical current $I_C = I_C^0|\cos(\pi\Phi/\Phi_0)|$, where Φ is the flux through the SQUID loop.

The corresponding Josephson coupling energy is $E_J(\Phi) = E_J^0|\cos(\pi\Phi/\Phi_0)|$ where $E_J^0 = (\Phi_0/2\pi)I_C^0$ is the fluctuation free SQUID Josephson energy at zero magnetic field. By applying a small magnetic field, we obtain the modulation of switching current with flux through the loop, shown in Fig. 4.2. The sinusoidal fitting of I_{SW} agrees with the theoretical prediction. Note that here I_{SW} is much smaller than the critical current I_C^0. The device parameters of three sSETs are shown in Table 4.1.

The junction dimension is estimated from the SEM image. Using a specific capacitance 45fF/μm^2 [55, 125], we can calculate the junction capacitance. The gate capacitance is obtained from the periodicity of switching current or the conductance with respect to gate voltage (see Fig. 4.13 and 4.14) as $C_g = e/V_g$ or $2e/V_g$. The total capacitance of the island is $C_\Sigma = 2C_S + C_g$ and the charging energy is $E_C = e^2/2C_\Sigma$.

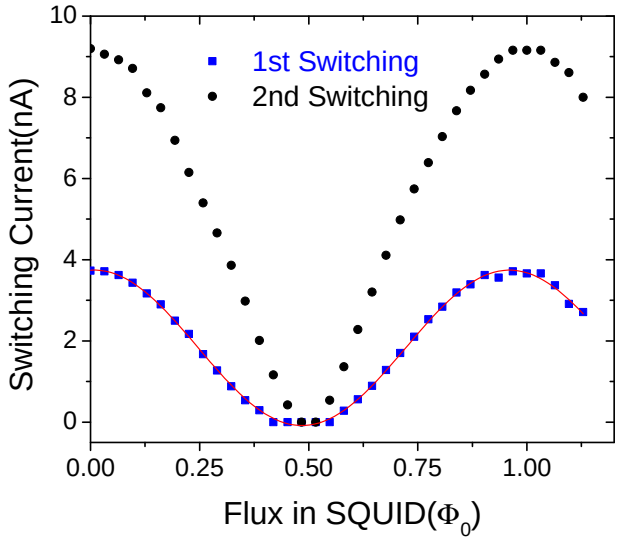

Figure 4.2: Flux modulation of two currents of sSET switching into $2\Delta/e$ and $4\Delta/e$ voltage states. T=40mK, g=464. Bottom data is the switching current I_{SW} with a sinusoidal fitting.

Similar to Equation 2.57, after adding the dissipation and bias current terms, the Hamiltonian of the whole circuit is written as

$$H_0 = E_C(n - \frac{Q_g}{e})^2 - 2E_J \cos(\frac{\phi}{2}) \cos\theta - 2E_J \frac{I}{I_C^0}\phi + H_{envi}, \tag{4.1}$$

where $\phi = \varphi_1 + \varphi_2$ is the total phase across the sSET and regarded as a classical variable. φ_1 and φ_2 are the phases of two respective SQUIDs. $\theta = (\varphi_1 - \varphi_2)/2$ is the conjugate variable to n and $\cos\theta$ couples two quantum states differed by one Cooper pair. H_{envi} is dissipation related energy, due to the real part of total impedance seen by the sSET $Z_T(\omega)$, which is determined by R_{2DEG}. Dissipation is inversely proportional to R_{2DEG} and the dissipation factor $g = 3R_Q/4R_{2DEG}$. At $V_{BG} = 0$, g is maximized in our experiment.

We have different knobs to adjust each term in the Hamiltonian. The charging related energy can be tuned by the gate voltage to the 2DEG.

This voltage is applied from a battery or a National Instrument BNC 2090 DAC output through a 10000:1 voltage divider. To avoid the grounding loop and current noise within the 2DEG, we only use one Ohmic contact as the V_g electrode, leaving the other three open. Josephson energy can be controlled by the small magnetic field $B = \mu_0 nI$, where n=6×10^4/m is the linear density of the NbTi wires of the solenoid and I is the driving current from the 2090 DAC passing through a 500Ω resistor. It is calculated that a current of 6.5mA is necessary to produce the 0.5mT field (corresponding to $\Phi_0/2$) to lower E_J down to zero. Due to the focusing effect from the 10μm wide superconducting lead, it requires only ∼3.0mA current for generating a $\Phi_0/2$ flux through the loop. To reduce the residue field and flux noise, we used multi-layers of mu-metal shields. The I-V curves are symmetric for applied positive and negative magnetic field to the SQUID, showing the negligible residue magnetic filed. V_{BG} is used to tune the dissipative energy. As V_{BG} is increased from 0 to -600V, the decrease of g is different for three samples (see Table 4.1). The tuning of dissipation is not dependent on temperature from base temperature to $\sim 1K$.

4.1.2 Experiments and Data Analysis

We use current bias configuration to measure the transport and switching current. Bias current is applied from a battery powered triangle wave function generator through two symmetric 100MΩ resistors. This differential setup produces $\pm I$, for keeping the island potential at zero so that the effective gate voltage to the island is only controlled by the applied V_g. The voltage across the sSET is amplified by a PAR 113 amplifier with a gain setting at 2000. The amplified is sent to the 2090 DAC voltmeter for recording. Each electrical lead to the voltage, current pads and Ohmic contacts has a total ∼45nF capacitance to the ground. This relatively large distributed capacitance with the resistance of the cable and resistors in the filters, from room temperature connector to the end at base temperature, is good for noise cancelation but also leads to a long time constant of the

circuit.

Switching current statistics are measured with the same setup by applying a set of triangle current pulses. The voltage across the sSET is amplified and sent to an Agilent 53132A universal counter with a 200MHz sampling frequency. In fact, we only use the first quarter of the triangle wave because the switching current has been obtained once bias current reaches I_{SW}. Two trigger signals to the counter are set to be 0 and 50mV which corresponds to a 25μV voltage on the sSET. In the supercurrent branch, the voltage is approximate zero. After the sSET switches, the voltage reaches 190μeV. The time interval Δt in which the sSET stays in supercurrent branch is collected and sent to the computer. With known constant current ramp rate dI/dt, $I_{SW} = dI/dt\Delta$t. We allow the maximum bias current to be slightly greater than I_{SW} (5nA for sSET#33 with $E_J/E_C =$ 2.3 for instance) so that the sSET will not escape into the $4\Delta/e$ state. Up to 5000 switching events at a repeating with a frequency of 5Hz are collected for good statistics. In Fig. 4.3, the cumulative data points show a histogram of I_{SW} and the escape probability function $P(I)$ as a function of I_{SW}. The histogram is fitted in a Gaussian equation. It is convenient to characterize the dissipation or gate dependence of the switching current at a given temperature by two values: the mean $< I_{SW} >$ and the standard deviation ΔI_{SW}.

To obtain the escape rate $\Gamma(I)$, we use the method developed by Fulton and Dunkleberger [78]. The sweeping current is divided into multiple channels with equal width ΔI for this analog to digital conversion. The escape probability $P(I)$ and the current ramping rate dI/dt determine the escape rate as

$$\Gamma(I) = \frac{1}{\Delta I}\frac{dI}{dt}\ln\left[\sum_{i\geq I} P(i) \Big/ \sum_{i\geq I+\Delta I} P(i)\right]. \tag{4.2}$$

In our experiment, the measured $\Gamma(I)$ falls into the range from 10s^{-1} to 10^4s^{-1} because of the low sweeping rate. ΔI should be chosen to be

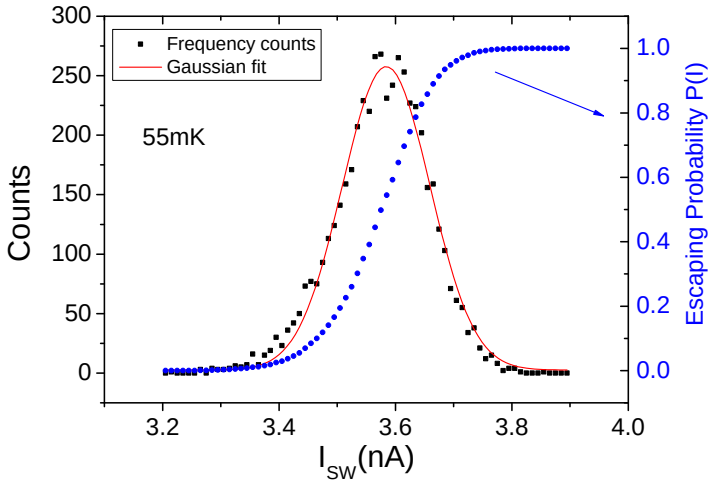

Figure 4.3: An example of I_{SW} histogram and the escape probability as a function of current at 55mK, E_J/E_C=2.3 and g=464. The solid line is a Gaussian fitting of the data.

appropriate based on the measured current range. For sSET#33, we chose ΔI=0.01nA for E_J/E_C=2.3, 0.005nA for E_J/E_C=1.6 and 0.002nA for E_J/E_C=1.2, respectively. These selections ensure a smooth distribution of I_{SW} and a large number of the escape events in each ΔI. Note that as the temperature and g change, the range of I in which a given range of $\Gamma(I)$ occurs also changes for fixed dI/dt and ΔI.

4.2 Classical Regime

4.2.1 Effect of Dissipation on I_{SW}

For sSET#33, we did not see a clear evidence of gate dependence of I_{SW}, i.e. V_g didn't affect I_{SW}. Thus, this device stays in the classical Josephson regime where the charging effect can be negligible. We set $V_g = 0$ for the whole switching current measurement. In Fig. 4.4, the I_{SW} histograms are shown for three different dissipations. As g increases, the

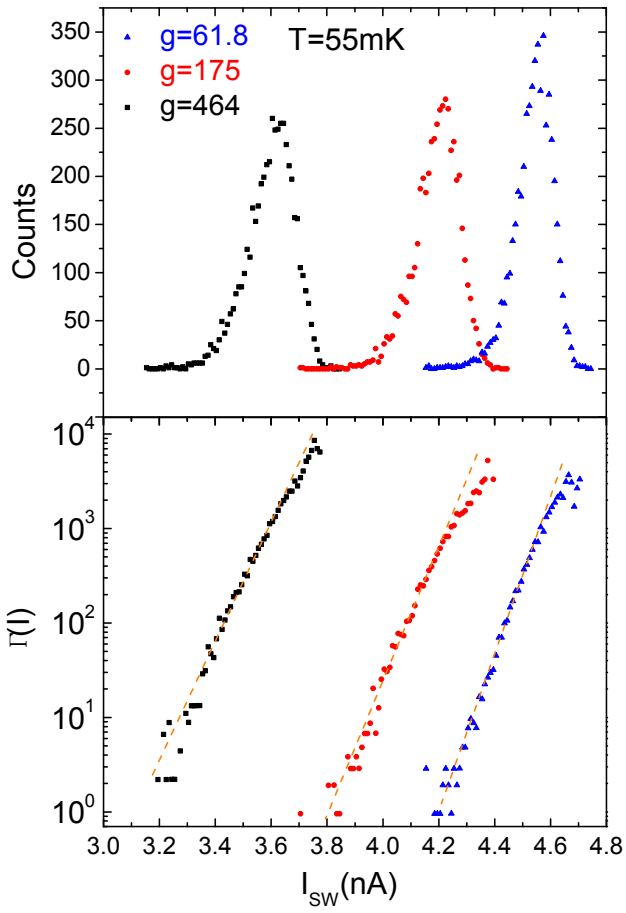

Figure 4.4: I_{SW} histogram (top) and escape rate $\Gamma(I)$ (bottom) as a function of I_{SW} for g=61.8, 175 and 464 respectively.

histogram moves to a lower switching current and becomes wider. Thus the mean switching current $< I_{SW} >$ decreases as dissipation increases. The deviation of the linear fitting of $\Gamma(I)$ at the highest tunneling rate (the tail of the histogram) is due to the phase diffusion involved in the switching.

It has been shown that phase diffusion and retrapping must be included to calculate the escape rate [126, 127]. In our measurement, the switching current is only 15% of the critical current at 20mK and g=464, due to

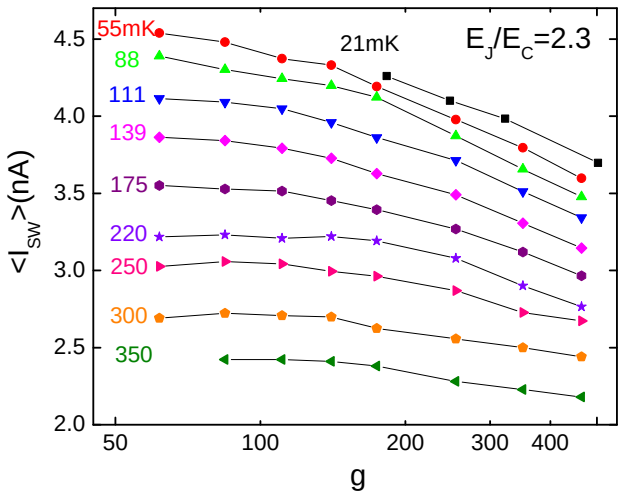

Figure 4.5: I_{SW} as a function of g for different temperatures, E_J/E_C=2.3.

the strong charging effect and quantum fluctuations [44, 66]. Although the sSET can be seen to be a single Josephson junction, the effective capacitance is difficult to estimate. Thus, we don't have an accurate effective critical current and capacitance for the calculation. Thus, we will only focus on the mean switching current $< I_{SW} >$ and the standard deviation of the histogram ΔI_{SW}.

$< I_{SW} >$ is plotted as a function of g at different temperatures for $E_J/E_C = 2.3$ in Fig. 4.5. As g increases from 62 to 464, $< I_{SW} >$ decreases monotonically in this low impedance, strong damping limit. We use the data at $g = 62$ as the reference. When temperature is increased from $T = 0.08E_J^0/k_B$ (55mK) to $0.5E_J(0)/k_B$ (350mK), the relative change of $< I_{SW} >$ decreases from 21% to 10%. Above 450mK, the dissipation dependence of I_{SW} becomes very weak due to strong thermal fluctuation, comparable to E_J/k_B. Note that the data from 21mk to 44mK were collected in different cool down and the tuning of g is different.

Although $< I_{SW} >$ decreases with g, this will not directly lead to a

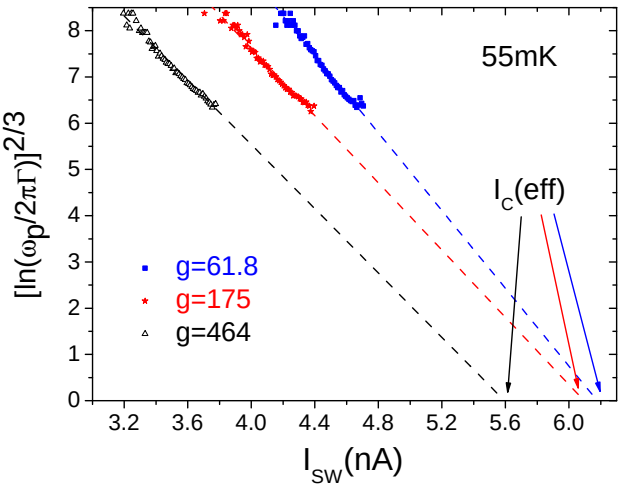

Figure 4.6: $(\ln \omega_p/2\pi\Gamma)^{2/3}$ vs I_{SW} for three g at 55mK, E_J/E_C=2.3. The dashed lines are linear fitting.

decreased effective critical current $I_C(eff)$ and corresponding Josephson energy. From the escape rate $\Gamma(I)$, we can derive $I_C(eff)$ of the sSET. Based on Equation 2.15, 2.16 and 2.19, we see $[ln(\omega_p/2\pi\Gamma)]^{2/3}$ is a linear function of switching current. The intercept of the linear fitting on current axis is $I_C(eff)$, where escape rate is zero. Fig. 4.6 shows an example at 55mK. Three values of $I_C(eff)$: 6.35, 6.29 and 5.81nA are obtained, corresponding to g values of 61.8, 175 and 464, respectively. The amplitude of the decrease is only 9%, much smaller than the value of 21% for $< I_{SW} >$. Here we treat $\omega_p = \omega_{p0}$ because ω_p is weakly dependent on I if I is not close to I_C^0. Although the fittings deviate from the data at highest escape rate, $I_C(eff)$ is mostly determined by the very low $\Gamma(I)$ where the energy barrier is equal to the effective Josephson energy $E_J^0(eff) = 2eI_C(eff)/\hbar$.

The main result of this device is the decreasing $I_C(eff)$ as g increases for all temperatures. Despite the effect of dissipation on $I_C(eff)$ being

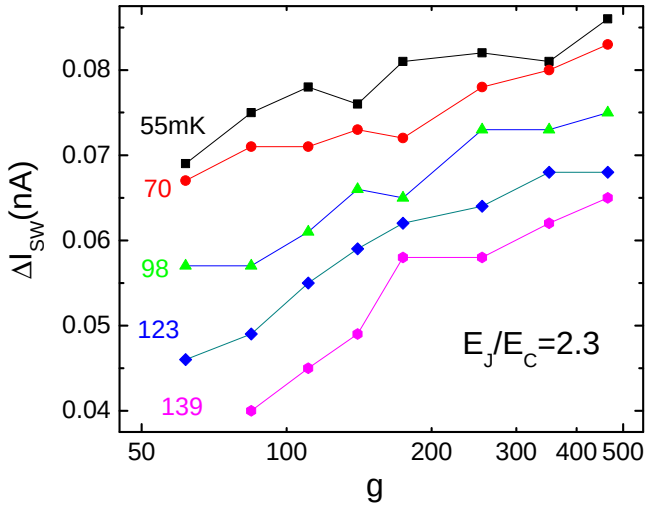

Figure 4.7: ΔI_{SW} as a function of g for a set of temperatures, E_J/E_C=2.3.

much smaller than that on $< I_{SW} >$, we observe that as dissipation increases, the effective Josephson energy $E_J^0(eff)$, as well as the energy barriers for escape, decreases monotonically. At higher temperature, thermal noise is comparable to the energy barrier, or even greater than it, thus the influence of dissipation on $I_C(eff)$ becomes very weak.

Not only do the envelopes of I_{SW} histogram move to lower current values, but also they become wider as g increases. We plot the standard deviation of the histogram, ΔI_{SW}, as a function of the dissipation factor in Fig. 4.7. The data below 44mK are not shown because they are hard to be identified from 55mK symbols. ΔI_{SW}, representing the fluctuation of I_{SW}, increases with dissipation for all temperatures. If we normalize ΔI_{SW} to $< I_{SW} >$ for different dissipations, this behavior becomes more pronounced. We interpret this to be the consequence of the reduced effective Josephson energy and escape energy barrier. In this device, the phase is less localized with smaller effective Josephson energy, causing the fluctuation to be raised.

From the duality point of view, the charge number is conjugate to phase variable. In this classical Josephson regime, because phase is well-defined, quantum fluctuations of the charge are significant. As g increases, dissipation compresses the charge fluctuations. As a consequence, charge is more localized, causing more phase fluctuations. Thus, the dissipative contribution to ΔI_{SW} increases if we keep all other parameters constant, driving the histogram wider.

4.2.2 Temperature Dependence of I_{SW}

For a classical large junction with negligible charging energy, the escape has three different mechanisms. Below the crossover temperature T_{cr}, macroscopic quantum tunnelinl/g (MQT) is dominating. The switching current histogram is temperature independent in this region. As temperature increases, the switching evolves into a thermal activation regime where ΔI_{SW} scales with $T^{2/3}$. The switching current histogram becomes wider with T. If temperature increases continuously, the higher thermal phase diffusion and retrapping probability drives the thermally activated escape into the third region where ΔI_{SW} starts to decrease when temperature increases. In this region, temperature not only helps the phase particle to escape, but also to trap the particle back to the bottom of one potential well, causing ΔI_{SW} decrease. This phenomenon is strongly affected by the dissipation and has been observed in different types of Josephson junction circuits [95, 126, 128, 129].

A set of I_{SW} histograms and corresponding values of $[\ln \omega_p/2\pi\Gamma]^{2/3}$ for different temperatures are plotted in Fig. 4.8. We see the histogram becomes narrower when temperature increases. In the bottom panel, at higher temperature, the larger deviation in the linear fitting indicates a stronger phase diffusion induced by thermal effect at higher T. The effective critical current and the effective Josephson energy, derived from the fitting, also decreases as temperature increases. This is the natural result of the narrowed I_{SW} histogram as temperature increases.

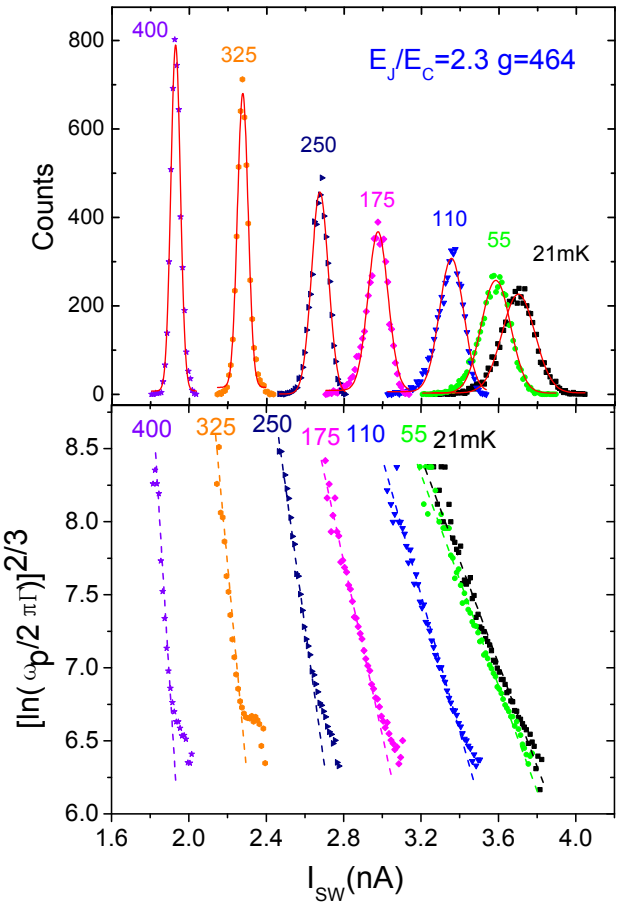

Figure 4.8: I_{SW} histogram and $(\ln \omega_p/2\pi\Gamma)^{2/3}$ for different temperatures. E_J/E_C=2.3 and $g = 464$.

In Fig. 4.9, ΔI_{SW} is plotted as a function of temperature for different E_J/E_C and dissipation. The main result is that ΔI_{SW} decreases as T increases above 50mK for both E_J/E_C cases. Below this temperature, however, we can not make a definite statement based on the scattered three data points. The negative slope of ΔI_{SW} is the main consequence of phase diffusion involved in the thermal escape mechanism. In a small Josephson junction circuit, phase diffusion is significant even at very low

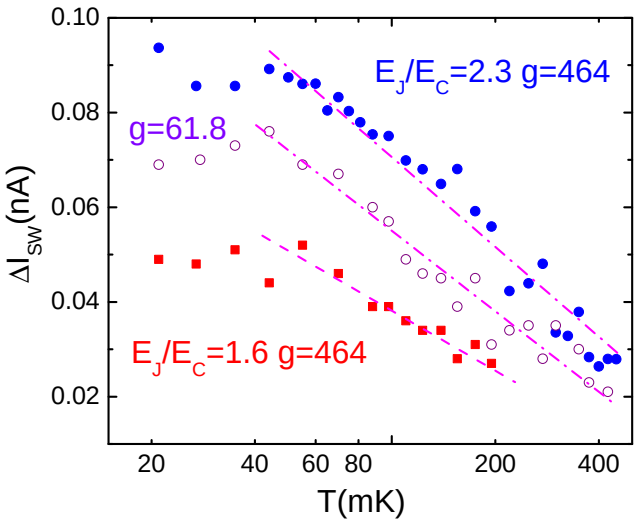

Figure 4.9: ΔI_{SW} of switching current histogram as a function of temperature. Blue dot and green triangle: E_J/E_C=2.3, g=464, 61.8, red square:E_J/E_C=1.6, g=464. Dashed lines are guides for eye.

temperature. Due to the strong damping at microwave frequencies, ΔI_{SW} shows a decreasing relation with temperature even in the MQT regime where phase diffusion is also involved in the escape process [130].

For sSET#33 with $E_J/E_C = 2.3$, the plasma frequency of the SQUID is estimated to be $\sim 4\times10^{11}$rad/s, and the effective impedance seen by the sSET is 30-140Ω as g decreases from 464 to 61.8. In this strong damping circuit, the crossover temperature T_{cr} from thermal activation to MQT is estimated to be between 20mK and 100mK. Low temperature (<50mK) behavior of ΔI_{SW} in Fig. 4.9 suggests a different escape mechanism in this temperature range. We think that a possible explanation is that the junction starts to enter the MQT starting at 50mK, thus thermal phase diffusion rate is compressed significantly. Note that we didn't see a clear difference of the crossover temperature for different values of g although T_{cr} is highly dependent on the damping. For the smaller E_J case, the crossover temperature is also lowered. The flat region of ΔI_{SW} starts at

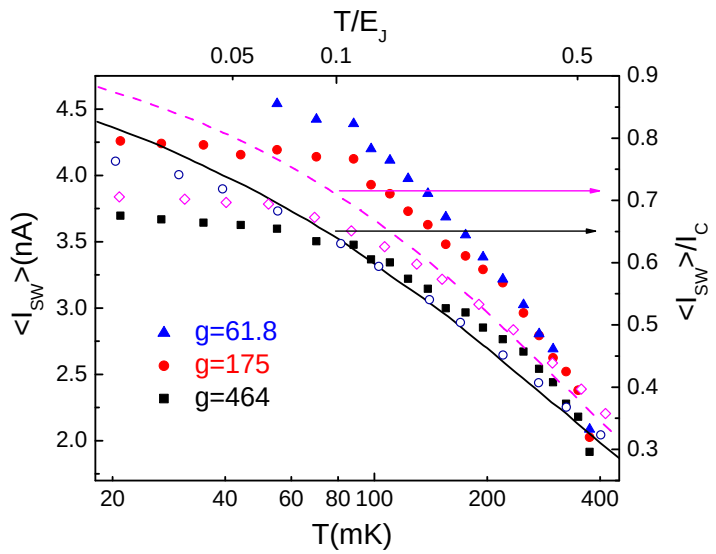

Figure 4.10: $< I_{SW} >$ as a function of T for three dissipation, E_J/E_C=2.3 (left and bottom axis). Circle and solid line: experimental result and theoretical calculation of a single Josephson junction with a shunting resistance $R_S = 70\Omega$ and g=370; diamond and dashed line: $R_S = 540\Omega$ and g=48. Data are reproduced from Ref. [49] (right and top axis).

~40mK, consistent with our interpretation.

Considering the absence of gate charge dependence of switching current, the sSET is considered to act as a single Josephson junction. To compare our results with the relevant theory of the effect of dissipation on switching current, we redraw $< I_{SW} >$ as a function of temperature for different dissipations in Fig. 4.10. Similar to the behaviors of ΔI_{SW}, $< I_{SW} >$ has a weak but noticeable temperature dependence below ~50mK. We do not have the data for lowest value of g below 50mK. The change of $< I_{SW} >$ due to dissipation is greater at low temperature, but decreases as more thermal noise is introduced.

The circle, diamond, solid and dashed line are the experimental data and theoretical calculations, of the switching currents, of two Josephson junctions with $E_J/E_C \approx 8$, in a frequency dependent dissipative envi-

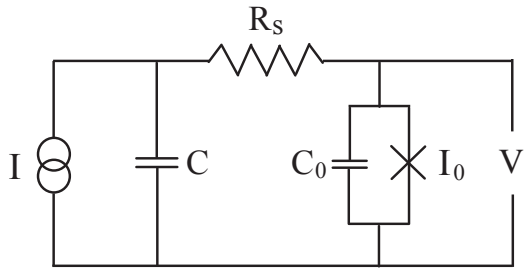

Figure 4.11: The equivalent circuit of a single Josephson junction in a frequency dependent dissipative environment, adopted from [49].

ronment composed of shunting resistance R_S and capacitance C (from [49, 131]). The circuit in Fig. 4.11 is analogous to our circuit model. Defining two damping parameters $\alpha_0 = \Phi_0/2\pi R^2 I_0 C_0$ and $\alpha = C/C_0\alpha_0$, where I_0, C_0 are the critical current and capacitance of the junction with $C \gg C_0$ and $R_S \ll R_Q$. In the strong damping regime $\alpha_0 \gg 1$, the escape rate is found to be

$$\Gamma \propto \exp[-B]. \tag{4.3}$$

The parameter B is the effective energy barrier for escape and is dependent on the damping factor as $B \propto \alpha$. Thus, for higher R_S (smaller dissipation), the larger barrier will lead to a larger switching current. Since two samples with different damping have different critical current and I_{SW}, a normalized value is used to compare within the theory. The junction with stronger damping ($R_S = 70\Omega$) agrees well with the calculation (solid line), however, the sample with smaller damping has a dramatic deviation at low temperature $T < 0.1E_J/k_B$. In high temperature region, where thermal activation dominates, $< I_{SW} >$ increases as R_S increases for both samples.

In the low temperature range, a much lower I_{SW}/I_C is seen in the smaller damping sample ($\alpha_0 = 3$) while the assumption of the calculation

requires $\alpha_0 \gg 1$. For weak damping, the crossover temperature between the MQT and thermal activation regime, T_{cr}, is higher. Thus, the sample with higher R_S starts to enter MQT regime at $T \sim 0.1E_J/k_B$, showing the temperature independent region. In terms of dissipation, I_{SW}/I_C increases as g is increased. This result is opposite to the observation at higher temperature because of the dominant thermally activated escape mechanism.

Our experiment has the advantage of *in situ* tunable dissipation, where the capacitor between the leads and 2DEG can be seen same as the shunting capacitor in Fig. 4.11 since it is much larger than the junction capacitance. The dissipative distributed 2DEG resistance acts as the effective shunting resistance for the sSET. We can use a single sample to test the theoretical prediction by tuning dissipation only, while keeping other parameters of the circuit unchanged. The experimental data qualitatively agrees well with the theory in the thermal activation regime.

At very low temperature, the sSET may enter the quantum tunneling regime. From base temperature, increasing dissipation will decrease the height of the effective energy barrier, causing switching current to be reduced. Moreover, the dissipation dependence of ΔI_{SW} in Fig. 4.7 is also a natural result of the theory: the relative change of the barrier height B and consequently the slope of $\Gamma(I,T)$ with respect to I increases as dissipation increases, causing ΔI_{SW} increases with g.

As discussed above, our results can be understood as the compression of quantum charge fluctuations associated with the well-defined phase variable in classical Josephson regime. It is understood that the switching current and effective Josephson energy decreases as dissipation increases in both thermally activated regime and quantum tunneling regime. This suggests that the theory in [49] may be extended to the MQT regime.

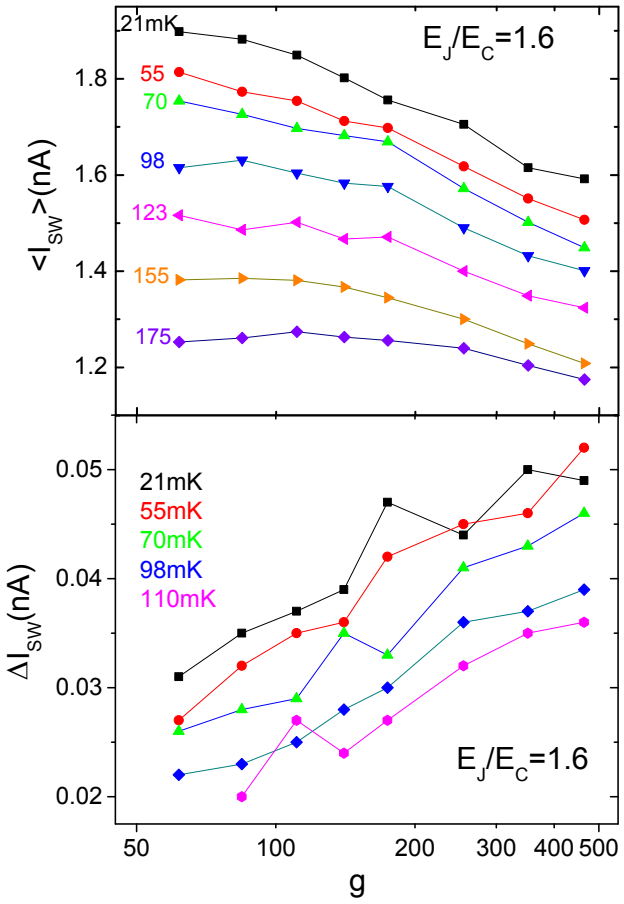

Figure 4.12: $< I_{SW} >$ and ΔI_{SW} as a function of g for a set of temperatures, E_J/E_C=1.6.

4.2.3 Smaller E_J Cases

A magnetic field was applied to tune E_J down, for values of E_J/E_C to be 1.6 and 1.2. We also tried an even smaller $E_J/E_C < 1$, but the thermal noise at low temperature is comparable to the effective Josephson energy. This causes a significant fluctuations in I_{SW} histograms. Both $E_J/E_C = 1.6, 1.2$ cases show similar behavior of I_{SW} with respect to dissipation, as the larger ratio of $E_J/E_C = 2.3$. This indicates that the sSET stays in the classical

regime even in the case where the Josephson energy is lowered to be same as charging energy. Here, we focus results for the medium value of $E_J/E_C = 1.6$, shown in Fig. 4.12.

As E_J/E_C is reduced from 2.3 to 1.6 and 1.2, the relative change of $< I_{SW} >$ due to dissipation decreases. Moreover, $E_J(eff)$ obtained from the escape rate drops faster than the decrease of E_J, due to the stronger charging effect on the phase variable [44]. We did not find any sign of the crossover from classical Josephson regime to charging regime in this sample, having a normal state resistance $R_N = 10.5k\Omega$ for each SQUID. In the tuning range of g from 464 to 61.8 corresponding to R_{2DEG} values from 41.8 to 314$\Omega/\square$, $< I_{SW} >$ increases as dissipation decreases.

We address the question whether the sSET can enter into the charging regime with a high shunting impedance. We have estimated that the highest $Re[Z_T(\omega)]$ is only 140Ω at the plasma frequency for g=61.8, but $Re[Z_T(\omega)]$ can be increased to $\sim$ 1000Ω at microwave frequency. If the sSET goes into the charging regime in this high impedance environment, this will be the so-called dissipation driven phase transition.

4.2.4 Gate Capacitance

We did not obtain any gate charge oscillation of $< I_{SW} >$ in this sample. The gate capacitance, however, is still crucial for calculating the charging energy. It is important in determining the dynamics of a sSET which can show a charging effect even for $E_J/E_C > 1$ in low impedance environment [132]. To obtain the exact value of gate capacitance, we measured the ac resistance as a function of gate voltage and observed a 1e periodic oscillation. The sSET is current biased in the unsymmetrical situation with I=1.5nA at 3.77Hz, which is about 1/3 of the switching current at base temperature. In this case, the island potential is not designed to be zero as current flows through the sSET. This causes the island effectively having potential difference relative to the 2DEG ground plane. As a consequence, the sSET has a measurable resistance at small bias current. From the

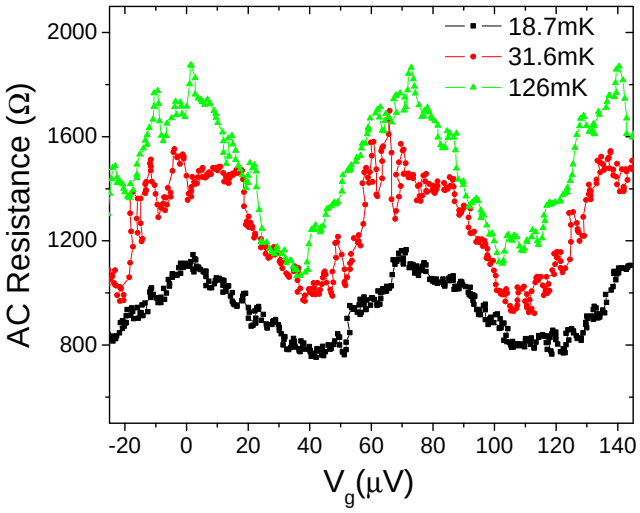

Figure 4.13: Ac resistance vs gate voltage V_g at different temperatures. E_J/E_C=2.3 and g=464.

periodicity of the gate voltage oscillation of ac resistance in Fig. 4.13, we can get the gate capacitance $C_g = e/V_g = 2.3fF$. Together with the estimation of junction capacitance from the SEM image, we calculated the charging energy of this sample.

4.2.5 Summary

To summarize, the sSET#33 with $E_J^0/k_B \approx 680mK$ and $E_J^0/E_C = 2.3$ shows that its dynamics is determined by the classical phase variable in a low impedance dissipative environment. For all values of $E_J/E_C = 2.3, 1.6$ and 1.2, the switching current and corresponding effective Josephson energy decrease as dissipation decreases. The effect of dissipation on $< I_{SW} >$ becomes smaller for smaller E_J case. As temperature is increased, thermal noise reduces the change of $< I_{SW} >$ due to dissipation. Moreover, the standard deviation of I_{SW} histogram becomes larger at higher g and decreases as temperature increases, indicating that the phase diffusion is

involved in the escape processes. The experimental results agree qualitatively with the theoretical calculation of a single Josephson junction in low impedance dissipative environment.

4.3 Charging Regime

In this section, we will describe the experimental results for SET#41 with a higher tunneling resistance. This sample shows a 1e gate charge oscillation of $< I_{SW} >$ and ΔI_{SW}. The distinct observation of switching current with dissipation, different from the sSET#33 in classical Josephson regime, can be understood in terms of the compression of quantum phase fluctuations in charging regime.

4.3.1 Effect of Dissipation and Charge Modulation

The parameters for this device are shown in Table 4.1. The switching current is only $\sim 10\%$ of I_C^0 for $C_g V_g/e = 1/2$ and g=532 at base temperature 15mK, due to the stronger charging effect in this device. As a comparison, the switching current is 15% of I_C^0 for sSET#33. The island has a smaller size (0.3μm×2μm) which results in a smaller gate capacitance. The mean switching current $< I_{SW} >$ shows a gate voltage oscillation, having a period $V_g = 110\mu$V which corresponds to a 1e periodicity. Thus $C_g = e/V_g$=1.5fF is directly obtained from this result. For different gate voltage and dissipation at different temperatures, 1200 or 2000 switching events of I_{SW} were collected for the statistics.

We set the gate voltage interval to be 2.5μV or 5μV for a good data density. After each histogram was obtained, V_g was adjusted to a different value and the device was allowed to equilibrate for 10s. Each scan covered several period, and took 8 hours at fixed values of dissipation and temperature. Some random offsets or slow drift of switching current, as the gate voltage is swept, can be attributed to the relaxation of background charges [133]. We did not use these data points in proceeding data

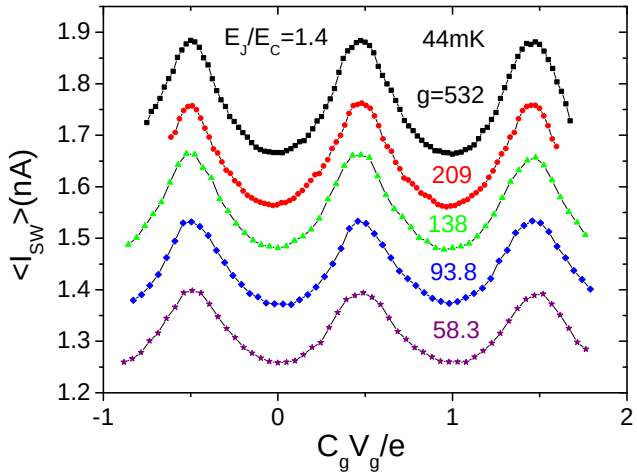

Figure 4.14: $< I_{SW} >$ as a function of gate charge for different dissipations. $E_J/E_C = 1.4$ and T =44mK.

analysis.

An example of $< I_{SW} >$ oscillations with respect to gate charge under different dissipation is shown in Fig. 4.14. Here gate charge number is obtained from the gate voltage using $n_g = C_g V_g/e$. $< I_{SW} >$ shows a 1e periodic oscillation with respect to gate charge, with the maximum at $n_g = n + 1/2$ and the minimum at $n_g = n$, defined as $< I_{SW} > (max)$ and $< I_{SW} > (min)$, respectively. The amplitude of the oscillation increases with dissipation, indicating a stronger charging effect. However, the effective impedance decreases as dissipation is increased. Because the charging nature is pronounced with a higher impedance environment, this discrepancy can not be explained well.

Because sSET#41 is in the charging regime, the charge number now is a good quantum variable. As a consequence, its conjugate variable, the total phase across the sSET which determines the Josephson coupling energy strength, has large quantum fluctuations. As more dissipation is introduced, quantum phase fluctuations are compressed, causing the phase to be more localized. Thus, the effective E_J represented by phase

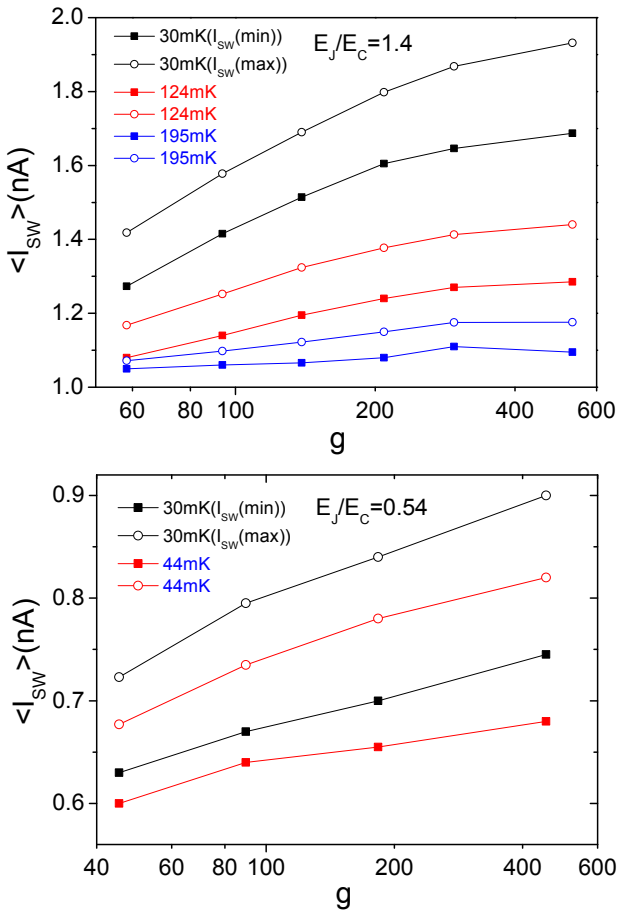

Figure 4.15: Dissipation dependence of $< I_{SW}(max) >$ and $< I_{SW}(min) >$ for different temperatures. Top: $E_J/E_C = 1.4$, bottom: $E_J/E_C = 0.54$.

variable increases with dissipation. In the measurement, as dissipation factor g increases, $< I_{SW} >$ increases for a specific gate charge number.

To check the quantitative increase of switching current with dissipation, we draw $< I_{SW}(max) >$ and $< I_{SW}(min) >$ as a function of g at certain temperatures for both cases of E_J/E_C. In Fig. 4.15, we see that the enhancement of $< I_{SW} >$ due to dissipation is pronounced at lower temperatures. At a higher temperature, thermal noise decreases the effect of dissipation on the switching current. Because a quantitative theory on

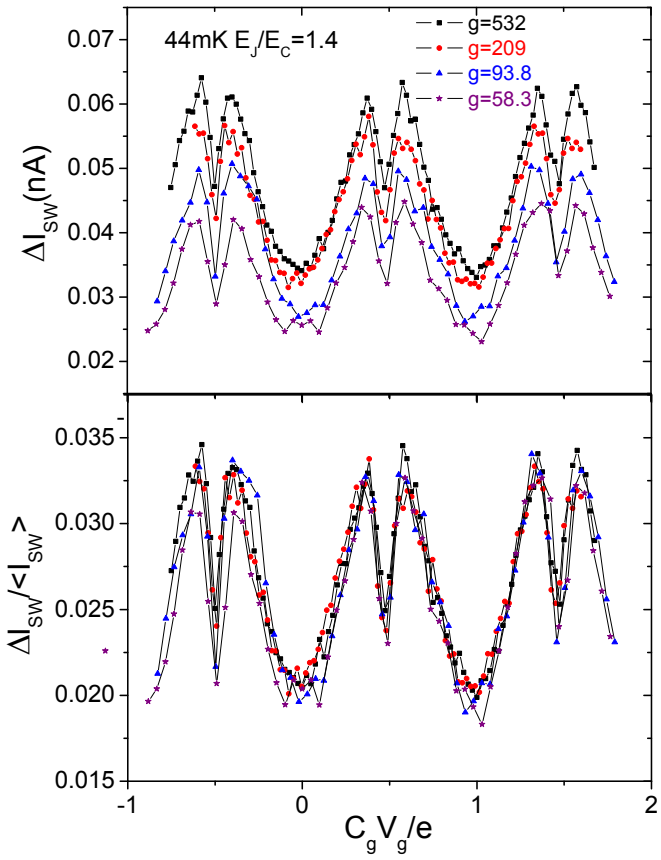

Figure 4.16: ΔI_{SW} oscillation with respect to gate charge number for different dissipation. Top panel: raw data, bottom panel: Normalized value. $E_J/E_C = 1.4$.

switching current in a dissipative environment in low impedance limit is still lacking, we only show that our results agree with the theory qualitatively [47].

Not only is $< I_{SW} >$ modulated by gate charge, but we see that the standard deviation of the I_{SW} histogram is also a periodic function of gate charge. In Fig. 4.16, ΔI_{SW} has a similar 1e periodic oscillation with n_g. We also observe that ΔI_{SW} shows a very sharp dip at $n_g = C_g V_g/e = 1/2$ (mod 1) for different g and temperatures. ΔI_{SW} has several

different sources: thermal noise, quantum phase fluctuations and charge fluctuations. Although the dynamics of the sSET is dominated by Cooper pairs with charge 2e, the charge related energy has the degeneracy point at $n_g = 1/2$ because of the existence of quasi-particle poisoning. When the gate charge is tuned to be close to the degeneracy point, switching current reaches its maximum, showing less phase fluctuation. Moreover, the energy dispersion with respect to charge is also flat and the sSET is less sensitive to the back-ground charge noise. Thus, the compression of these two noise sources for ΔI_{SW} cause this sharp dip. Note that at the degeneracy point, the sSET is unlikely excited from the ground state band to the first excited band due to the large band because of the comparable E_J and E_C. In our experiment, we did not find any signature of this tunneling across the band gap, and the sSET stays in the ground state. At higher temperature, this charge dispersion of ΔI_{SW} is more clear. The gate voltage modulation of $< I_{SW} >$ has almost disappeared, but ΔI_{SW} still shows a 1e periodicity of the dip (see Fig. 4.18).

To see how switching current is affected by gate charge, we draw the histogram for three distinct points on the $\Delta I_{SW} - C_g V_g/e$ curve: the valley where $n_g = 0$, the turning point where $n_g \approx 0.42$ and the dip where $n_g = 0.5$ respectively in Fig. 4.17. At $n_g = 0$ and 0.5, I_{SW} shows a very narrow histogram for both smallest and largest dissipation. For $n_g \approx 0.42$, however, there is a dramatic fluctuation in switching current histogram, either due to the quantum fluctuation of phase or the background charge noise. The switching current histogram may be composed by multiple histograms. Once the gate charge number is tuned to be greater than this point, the contribution of the total noise is reduced rapidly, causing the sharp drop of ΔI_{SW}. The behaviors of I_{SW} are similar for both low and high dissipation, however, higher g drives I_{SW} to a higher value.

For any fixed gate charge, ΔI_{SW} increases with dissipation. This behavior is opposite to that for sSET#33 whose ΔI_{SW} decreases as $< I_{SW} >$ is increased. Thus $I_C(eff)$ and the corresponding effective E_J, derived from the escape rate, will increase more than the raw values of $< I_{SW} >$,

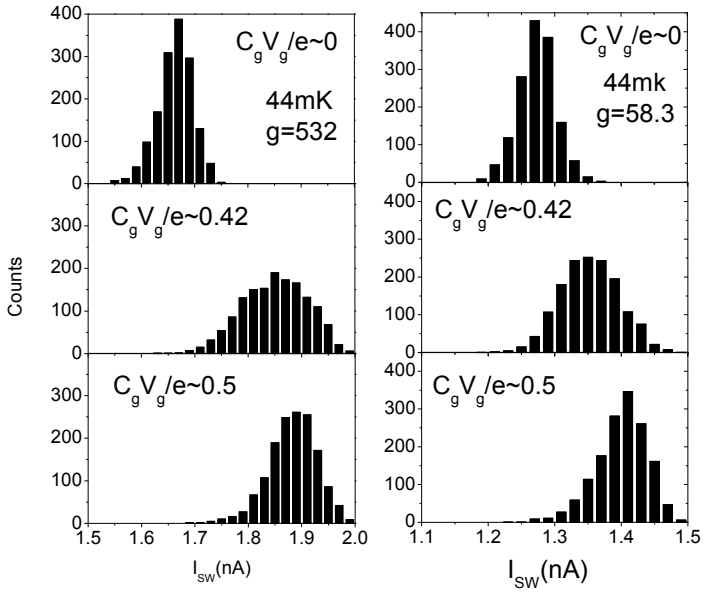

Figure 4.17: I_{SW} histogram at specific gate charge numbers under different dissipations. $E_J/E_C = 1.4$ and $T = 44$mK.

causing a better contrast than that seen in sSET#33.

The amplitude of ΔI_{SW} has a weak dependence on dissipation at very low temperature. The value of ΔI_{SW}, normalized to $< I_{SW} > (max)$ for different dissipations, overlap each with other in the bottom panel of Fig. 4.16. By contrast, the higher temperature data of ΔI_{SW} shows a strong dissipation dependence, increasing as g increases (see Fig. 4.18 for results at 195mK). These indicate that different mechanisms dominate the dynamics of switching current in different temperature ranges. We will discuss this issue in detail in the next section.

As temperature increases, the valley of ΔI_{SW} at $n_g = 0$ becomes indistinguishable from the other gate charge numbers, except for the region close to $n_g = 1/2$ (see Fig. 4.18). The dispersion of ΔI_{SW} with respect to gate charge is lost, however it does show a clear periodic function as gate voltage is swept. Note that the sSET at the charge degeneracy point is not

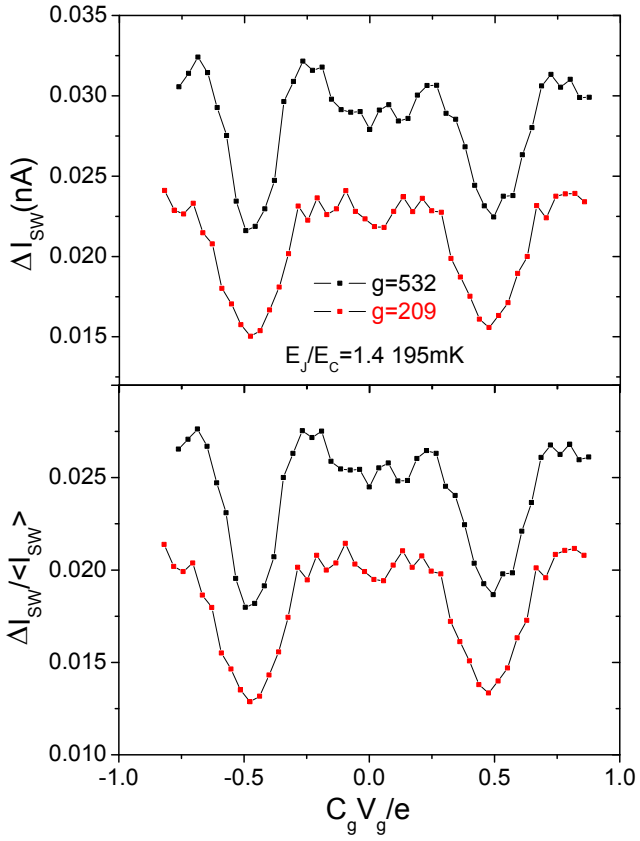

Figure 4.18: ΔI_{SW} as a function of gate charge number for different dissipations. Top panel: raw data, bottom panel: relative amplitude. $E_J/E_C = 1.4$ and T=195mK.

sensitive to thermal fluctuations at high temperature, where background charge noise is also reduced significantly.

For a smaller value of Josephson energy case ($E_J/E_C = 0.54$), $< I_{SW} >$ has similar dependence on dissipation, increasing with g. We made these measurement only for four different g values, as shown in Fig. 4.19. Surprisingly, as E_J/E_C is decreased from 1.5 to 0.54, $< I_{SW} >$ doesn't drop

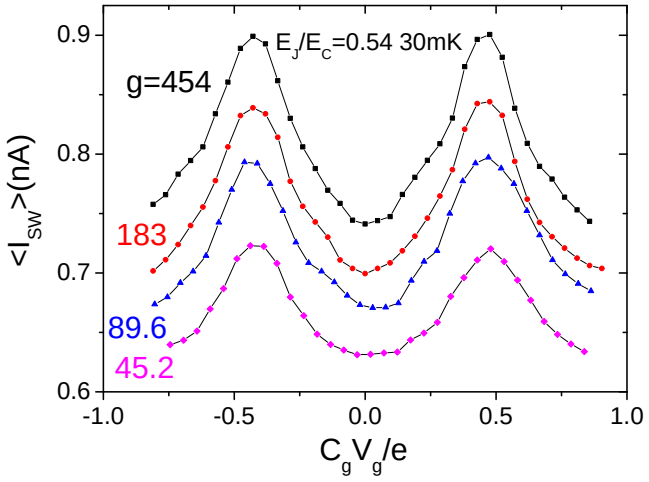

Figure 4.19: Gate charge oscillations of $< I_{SW} >$ for different dissipations. $E_J/E_C = 0.54$ and T=30mK.

correspondingly. For example, $< I_{SW} >$ is 1.93nA and 0.9nA for two E_J/E_C ratio respectively at 30mK for g=532. Comparing to sSET#33, if E_J/E_C is reduced by the same amount, $< I_{SW} >$, $I_C(eff)$ and corresponding effective E_J decrease more quickly than E_J/E_C, due to the compression on Josephson energy from the strong charging effect.

4.3.2 Temperature Dependence of $< I_{SW} >$

As temperature is increased, thermal fluctuations in both phase and charge increase, reducing the charge oscillation and $< I_{SW} >$. In Fig. 4.20, the gate charge oscillations of $< I_{SW} >$ at different temperatures are shown. Above 220mK, the sSET does not show charging behavior anymore for $E_J/E_C = 1.4$. Dissipation, however, has a big impact on switching current at a much higher temperature $\sim E_C/k_BT = 350mK$, improving $< I_{SW} >$ as g increases. At this temperature, the charging energy is still the most important parameter in determining the dynamics of the sSET. Once charge variable plays a major role in the Cooper pair tunneling, dissipation

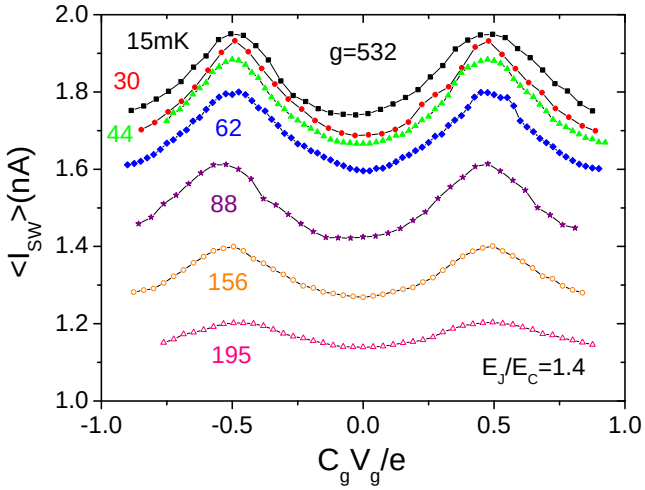

Figure 4.20: Gate charge oscillation of $< I_{SW} >$ at certain temperatures. $E_J/E_C = 1.4$ and g=532.

compresses quantum fluctuations in the phase, even in the case where the gate charge dependence of $< I_{SW} >$ is absent.

$< I_{SW} > (max)$ and $< I_{SW} > (min)$ is shown in Fig. 4.21 as a function of temperature for E_J/E_C=1.4. As temperature increases, the amplitude of the oscillation decreases. At $T > 0.6E_C/k_B$, this charge modulation is washed out. However, in the case of E_J/E_C=0.54, thermal noise starts to affect the effective Josephson coupling energy at a lower temperature because $E_J < E_C$.

Both ΔI_{SW} of $I_{SW}(max)$ at $n_g = 1/2$ and $I_{SW}(min)$ at $n_g = 0$ are plotted as a function of temperature in Fig. 4.22. We see two different slopes for $\Delta I_{SW}(max)$ in the top panel, showing two different temperature ranges in which escape mechanism may be different. The crossover temperature is $T^* \approx 150mK$ which is much lower than the temperature above which $< I_{SW} >$ charge oscillation disappears. This indicates that the escape dynamics is not a direct result of the charging effect.

It has been pointed out that phase diffusion may exist at a temperature which can be lower than the T_{cr} between MQT and thermal activation

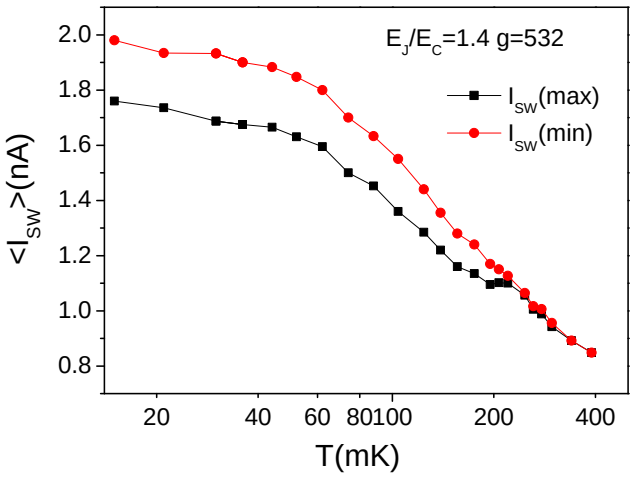

Figure 4.21: $< I_{SW} > (max)$ and $< I_{SW} > (min)$ vs temperature for $E_J/E_C = 1.4$ and $g = 532$.

regime, for small Josephson junction circuit [130]. Thus, quantum phase diffusion in MQT regime plays a different role as compared to the thermal regime, causing the different slope of ΔI_{SW} as a function of T. Although our results are different from those in detail in [130], we still believe that T^* is the indication of the crossover between quantum and thermal phase diffusion.

T_{cr} of sSET#41 is estimated to be $\sim 10-50mK$ in the dissipation tuning range. We attribute this discrepancy $T_{cr} \ll T^*$ to the existence of phase diffusion above the zero voltage state. As seen in the I-V curve, phase diffusion with very small voltage is mixed into the supercurrent branch. In our measurement, both of them are considered as the switching current because of the 25μV threshold voltage setting. The phase diffusion region with voltage less than 25μV is measured as the switching current. The calculation of T_{cr} is based on the strong damping from the 2DEG which is assumed to have a good capacitive coupling to the sSET at plasma frequency. If the sSET stays in the pure supercurrent branch before it switches, the microwave frequency impedance is small and the damping

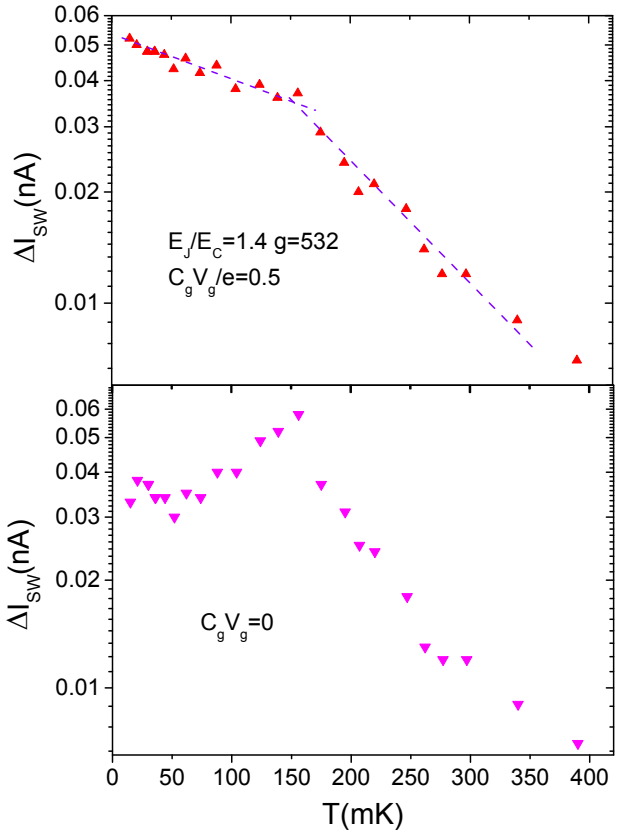

Figure 4.22: ΔI_{SW} of $I_{SW}(max)$ (top panel) and $I_{SW}(min)$ (bottom panel) histograms as a function of temperature. $E_J/E_C = 1.4$ and $g = 532$.

is strong. However, the corresponding frequency of phase diffusion is low and the coupling to dissipation is much weaker. Thus, we over-estimated the damping of the sSET. The actual T_{cr} is higher than the estimation.

Quantum phase diffusion below $\sim 150mK$ shows less temperature dependence of ΔI_{SW}, consistent with the classical Josephson junction in quantum tunneling regime where ΔI_{SW} has a very weak temperature dependence. Above the crossover temperature, thermal phase diffusion plays the major role. Temperature does not only help the sSET escape into the finite voltage state, but helps it being retrapped back into the

supercurrent branch more efficiently, causing the large slope. $\Delta I_{SW} \sim T$ relation on the bottom panel in Fig. 4.22 also confirms the different tunneling mechanism as the peak at $\sim 150mK$. Because ΔI_{SW} of $< I_{SW} >$ (max) at the dip is not sensitive to the charge fluctuations, we interpret our data mainly based on its temperature dependence.

4.3.3 Summary

We observed strong evidence of the single charging effect of sSET#41 with comparable Josephson and charging energy. $< I_{SW} >$ and ΔI_{SW} show a 1e gate charge oscillation for different dissipations. Even for $E_J/E_C = 1.4$, the dynamics is dominated by the charge variable, causing strong fluctuations in the phase. Introducing dissipation causes the phase to be more localized, resulting in the enhanced $< I_{SW} >$. Because ΔI_{SW} increases with dissipation, the effective critical current $I_C(eff)$ and corresponding E_J increases more quickly than $< I_{SW} >$. The sharp dip of $\Delta I_{SW} \sim C_g V_g/e$ at $n_g = 1/2$ proves that the fluctuations of charge variable is minimized at the degeneracy point. Moreover, the temperature dependence of ΔI_{SW} at the dip has smaller slope at low temperature, showing the clear evidence of quantum diffusion in quantum tunneling regime. Above the crossover temperature, thermal phase diffusion causes the larger slope in the plot of ΔI_{SW} versus T, which decreases as temperature increases.

4.4 High R_N Limit

Comparing sSET #33 with $R_N/R_Q = 0.4$ to sSET #41 withh $R_N/R_Q = 0.58$, sSET#41 has been in the single charge regime even for the case $E_J/E_C = 1.4$. The quasi-particle poisoning also cause the absence of 2e periodicity in the switching current. If we continuously increase the tunnel resistance R_N and decrease E_J/E_C ratio, will the sample show 2e periodicity in transport properties in low impedance environment? In the high R_N limit, the role of dissipation may match the theory which assumes a very small E_J/E_C [47].

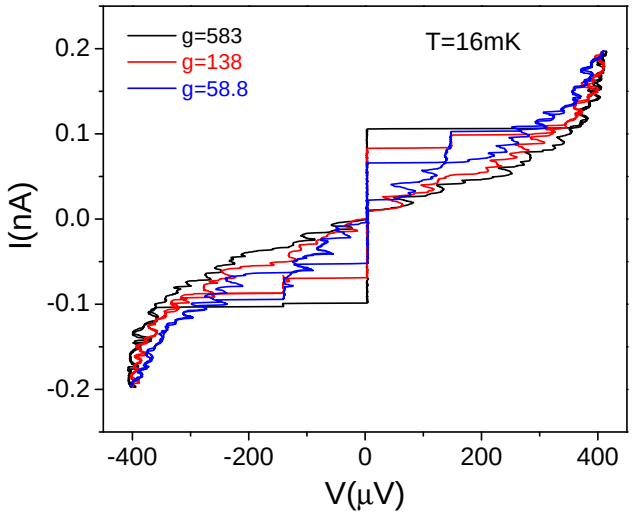

Figure 4.23: I-V curves of sSET#39 in current bias configuration for three different values of g. T=16mK and V_g=0.

In this section, we will give the experimental results of sSET#39 with higher $R_N/R_Q = 1.2$ and smaller $E_J/E_C = 0.4$. In fact, this sample was measured before sSET#41. After we became confident that it was in the charging regime, we went to the regime where E_J is comparable to E_C.

4.4.1 Transport Properties

The parameters of this device are also shown in Table 4.1. The I-V curves are measured using the same four-probe technique in both current bias and voltage bias configurations. The current biased I-V curve is very similar to previous samples, except that the supercurrent is very small. We only show an example with different dissipation in Fig. 4.23. $< I_{SW} >$ increases with g, as the consequence of dissipation compressed quantum phase fluctuations. ΔI_{SW} also show similar behavior as seen in sSET#41.

In the large dissipation limit, as current is ramped up, the voltage directly switches into $2\Delta/e$ voltage state with barely visible stair-like

feature in the middle. As g decreases, sSET switches into a voltage state $\sim 140\mu$V at a lowered switching current and then into the 2Δ state at a higher current. The decrease of I_{SW} in the first case is significant compared to that in the second switching due to the effect of strong damping at microwave frequency. Once the voltage across the sSET is finite, the dissipative coupling to 2DEG is very weak. Tuning the 2DEG will not change the dissipation and the second current jump in the middle significantly. Actually, the step at $\sim 140\mu$V is due to the energy exchange between the sSET and environment, which is the mechanism for incoherent tunneling of Cooper pairs. When the supplied energy from bias current matches one resonant mode of the environment, increasing bias current will not increase the voltage across the sSET. Instead, the energy goes into the environment, causing the stair-like behavior. This will be discussed in detail later for a voltage biased case, showing sharp current peaks at the same voltage.

It is convenient to bias the device using a voltage source because of the very small supercurrent. In a voltage biased sSET with small E_J/E_C ratio, Cooper pair tunneling causes several current transport mechanisms, having very rich structures on the I-V characteristics: the supercurrent at zero voltage [64, 102], resonant Cooper pair tunneling peaks at finite voltages [134, 135] and Josephson quasi-particle current above $2\Delta/e$ [136, 137]. Results from the experiment on the influence of dissipation can be compared to the well established theoretical calculation in this regime [30, 42, 47, 56].

The voltage is fed into the sSET through a voltage divider at room temperature. The current is amplified by a low noise current preamplifier (Ithaco 1211). The output from Ithaco 1211 is sent to a PAR 113 amplifier and is recorded by the BNC 2090 DAC. In fact, the voltage from the source is distributed on the sSET, filters, the leads and the input impedance of current amplifier. Thus, the actual voltage across the sSET is measured by another PAR 113 amplifier. The sSET is not biased symmetrically because the ground reference is set to be the chassis of the current amplifier, in

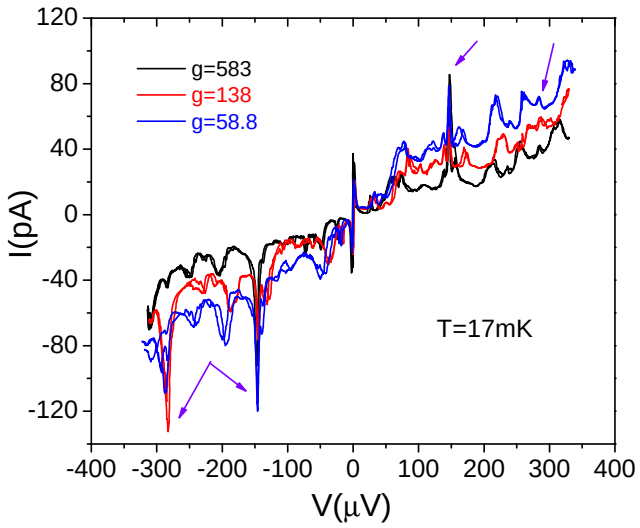

Figure 4.24: I-V curve in voltage bias situation for three different dissipations. $T=17$mK and $V_g=0$.

order to minimize its output voltage drift.

As shown in Fig. 4.24, the current arising at zero voltage deemed as the "supercurrent", is created by the coherent Cooper-pair tunneling since E_J is not negligible compared to E_C. In this voltage bias case, the supercurrent ∼40pA is much smaller than the value obtained in the current bias configuration. The effective gate voltage fluctuates when V_g is set to be zero, causing a small averaged supercurrent.

To test the tuning of the effective Josephson energy of the SQUID, we show the small voltage region of the I-V curve at different magnetic fields in Fig. 4.25. The supercurrent is tuned from its maximum ∼40pA to zero and then is recovered back when flux is increased to Φ_0. This full flux modulation of the current proves the junctions have very similar parameters.

Fig. 4.26 illustrates the large scale I-V curve with or without gate voltage. The current is measured at a slow voltage ramping rate (2mHz),

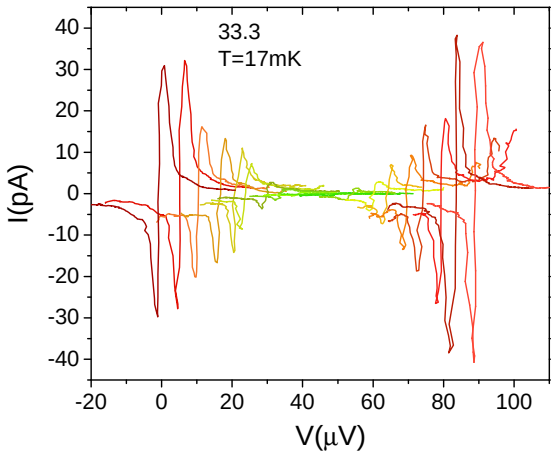

Figure 4.25: Modulation of Supercurrent branch of the sSET with flux in the SQUID loop. T=20mK, V_g=0, g=583. Left to right: Φ=0 to $\Phi = \Phi_0$, offset for clarity on voltage axis.

showing a very rich structure of current peaks at various bias voltage. At V>2Δ/e, the Josephson quasi-particle (JQP) current is significant, showing a broad peak until $\sim 600\mu$V. The current of JQP is carried by a cycle which consists of one Cooper pair tunneling through one junction and two quasi-particle tunneling through the other junction. At the charge degeneracy point, two macroscopic charge quantum states superposed by Josephson coupling can be identified from the spectroscopy of the photo-assisted JQP peaks [6].

Since the sSET is voltage biased in the un-symmetric situation, the JQP current peak heights are different for positive and negative bias. As the bias is slowly swept, we applied a fast gate voltage oscillation (0.4Hz). The current shows all the possible values with respect to gate voltage as an envelope on the curve. In this case, the JQP current peaks are symmetric for different voltages. The inset of this figure depicts the corresponding current at small voltages. The oscillating gate voltage causes the supercurrent peak to be smaller than the constant V_g due to

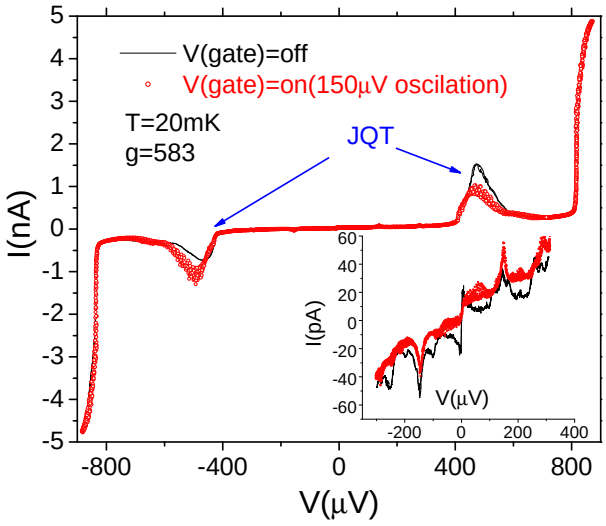

Figure 4.26: Voltage biased I-V curves at 20mK, $g=583$. The amplitude of sweeping gate voltage is 150μV. Inset: small voltage region shows the suppercurrent branch.

the averaging.

For small bias voltage V<2Δ/e, the contribution from quasi-particle tunneling on the current can be neglected. To see all the details of the sub-gap current peaks, we carefully measure the current when slowly ramping bias voltage (1mHz) and quickly sweeping gate voltage (2Hz). The I-V curves in Fig. 4.27 show all the possible current values for three different values of g. At certain values of bias voltage, the relative amplitude of current is maximized. If we voltage bias the sSET at this value, the gate charge oscillation of current will show the largest contrast, no matter whether the period is 1e or 2e.

In the low impedance case, $Re[Z_T(\omega)] << R_Q$, a very rich current pattern is seen in the I-V characteristics in Fig. 4.28. If we set the gate charge at a constant number, a single trace shows the strong gate voltage dependent supercurrent, and other current peaks (indicated by arrows) at finite voltage $V < 2\Delta/e$. These current peaks are due to the resonant

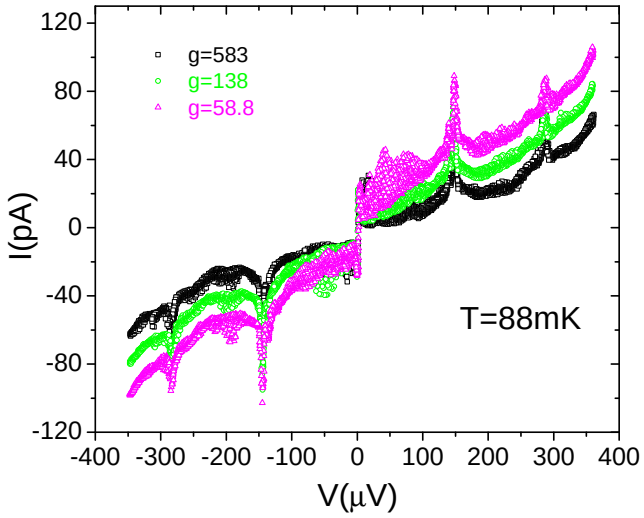

Figure 4.27: I(V, V_g) data at 88mK in small voltage region for different dissipation. Current is measured when slowly sweeping bias voltage and quickly sweeping V_g.

tunneling of Cooper pairs [135, 138] from the resonance of some internal energy levels of the transistor. The signature of this type of tunneling is that the peak positions are dependent on gate voltage because this type of resonance is determined by both bias and gate voltage.

Another type of current peaks are also shown in Fig. 4.27 and 4.28. As gate voltage is applied, the sharp current peak at $\pm 140\mu$V and $\pm 280\mu$V stay at the same position. Thus, these current peaks are not related to the internal resonant modes of the sSET. From the P(E) theory, current could arise from the energy exchange between the sSET and the environment. In our experiment, the dissipative environment is composed of superconducting leads with the capacitively coupled 2DEG plane, modeled as an infinite, lossy transmission line. If the energy from the voltage source matches some resonant modes of the environment, the sSET can feed the same a mount of energy to the environment or absorb the energy from the

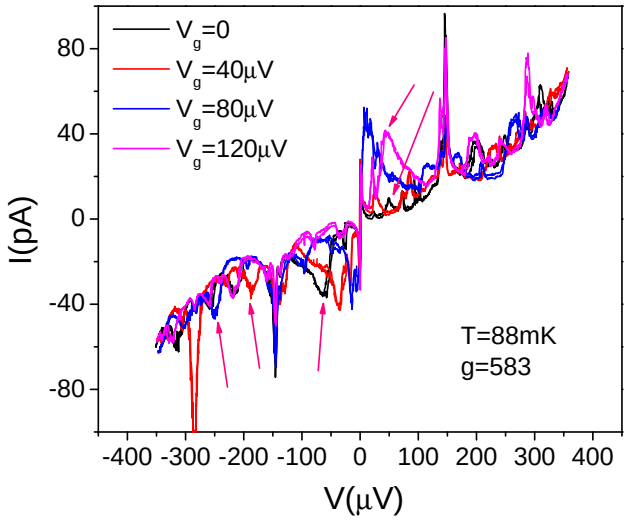

Figure 4.28: I-V characteristics with different gate voltage V_g for island charge numbers: 0, 1/3e, 2/3e and e respectively. Arrows point out some of the V_g dependent resonant tunneling current peaks.

environment, thus resulting in a current peak. As bias voltage is increased, the second current peak should be twice the value of the first one and so on. Note that the peaks at $\pm 280\mu$V are close to the broad JQP current peak and are hidden in some cases.

As g increases, these environment assisted currents stay at their original positions, but decrease with dissipation. This proves that the resonant modes of environment are mostly determined by the capacitance and inductance of the transmission line, but not the resistive component. The sSET favorite higher impedance environment at smaller g. Thus, the background and environment assisted current increases for smaller damping, as depicted in Fig. 4.27. Note that the resonant Cooper pair tunneling current peaks are broader than the sharp, environment assisted current peaks. If we change the dimensions of the transmission line, the characteristic resonant frequency will also change. As a result, these current

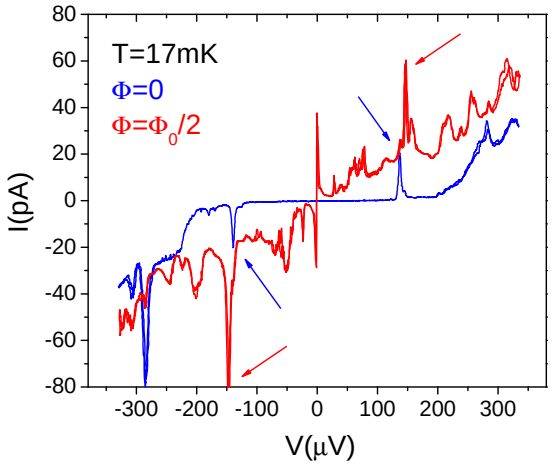

Figure 4.29: I-V curve with different flux through the SQUID loop. $T = 17$mK, $V_g = 0$, and $g = 583$.

peaks will occur at different voltages.

Because the resonant Cooper pairs tunneling peaks are determined by the excitation of internal energy levels of the sSET, the amplitudes and positions should be affected by the tuning of E_J and E_C. By changing the flux in the SQUID, two I-V curves corresponding to maximum and minimum E_J/E_C are shown in Fig. 4.29. In the case of $E_J \sim 0$, the supercurrent and resonant tunneling current peaks disappear as Cooper pair tunneling is compressed completely. The first environment assisted current peak is also reduced to $\pm 130\mu$V when $\Phi = \Phi_0/2$. The second one remains at the original position. We don't know why these two peaks show different behavior, however, both of them have a large contrast to the background.

If the sSET is biased at a different voltage, the amplitude of current oscillation with respect to gate voltage is different. We collected the $I - V_g$ curves of sSET#39 from low bias voltage to 500μV at low temperature in Fig. 4.30. At small bias, $I - V_g$ curve shows a very rich structure, due to the competition between the free energy of odd and even parity. Clear

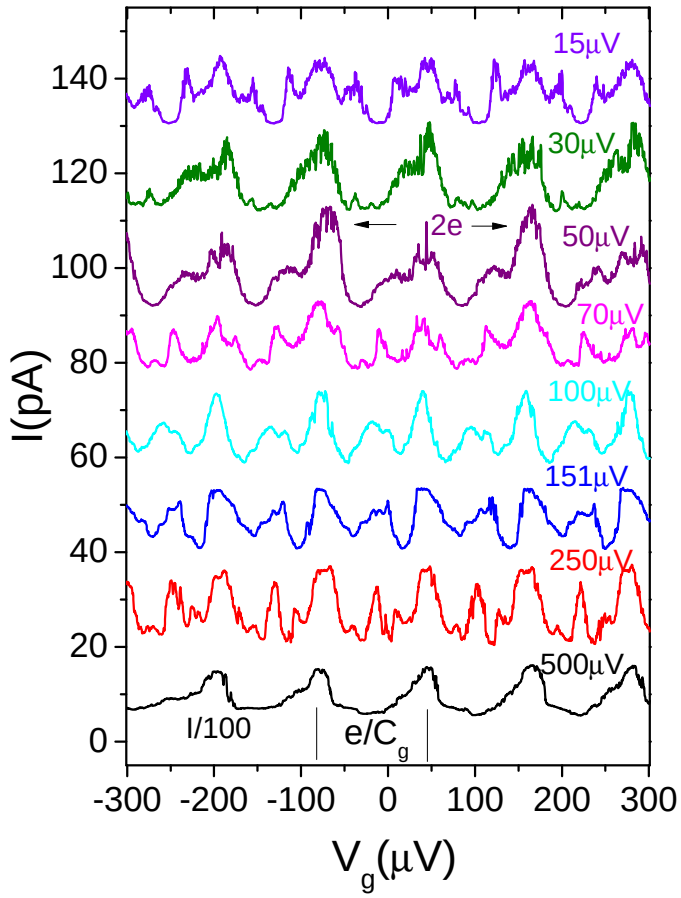

Figure 4.30: Modulation of the current by the gate voltage at different bias voltage (offset for clarity), the scale of black line is reduced to 1/100. $T = 17$mK and $g = 583$.

2e periodicity only appears for some specific bias voltages, for instance, 50μV and 70μV. As the bias voltage is increased, 2e periodicity is masked gradually by 1e periodicity as the sSET goes into the JQP region. A sufficiently high bias voltage of 500μV breaks the Cooper-pairs, causing quasi-particle tunneling to be dominant.

This 2e to 1e period change is used to determine whether the gate charge oscillation of sSET#41 is 2e periodic, although two devices have small deviations of the gate capacitance. One reason for the measurement on this high resistance sample is to obtain the exact value of the gate capacitance because we do not have strong magnetic field to drive the sSET to normal state where the device has a pure 1e periodic transport. Comparing the data of sSET#39 to sSET#41, we are confident that the charge oscillation of $< I_{SW} >$ for sSET#41 is 1e periodic. Moreover, because sSET#33 has a larger island with dimensions 0.35μm×4μm, the conductance oscillation with gate voltage has the period $V_g = 75\mu$V and $C_g \approx$2.1fF. As the island area is reduced from 1.4μm^2 to 0.7μm^2 for sSET#39, the corresponding capacitance drops to 1.3fF.

At low bias voltage and low temperature, Cooper-pair tunneling is the only mechanism for producing current through the sSET. The even number charge state has a lower free energy than the odd state. As temperature increases, the energy difference between these two states drops monotonically down to zero at a certain temperature. Thus a 2e periodicity of the $I - V_g$ curve at low temperature will evolve into a 1e periodicity with increasing temperature. Unfortunately, we did not finished this measurement before the sample was broken.

Dissipation also plays an important role on the switching current which is shown in Fig. 4.23. Considering the small $E_J/E_C = 0.4$ and large $R_N = 31.5k\Omega$, the sSET has a good quantum charge number and large quantum fluctuation in the phase variable. As dissipation increases, $< I_{SW} >$ increases as the quantum fluctuations in phase are compressed. The environment also affects the parity effect, as illustrated in Fig. 4.31. Current is measured at small bias voltage of 20μV as gate voltage is swept for different dissipations. We see a clear 2e periodicity of current with respect to gate charge at higher g. With increasing effective impedance, surprisingly, a small peak corresponding to the odd parity arises gradually. We do not have a clear picture why this phenomenon occurs.

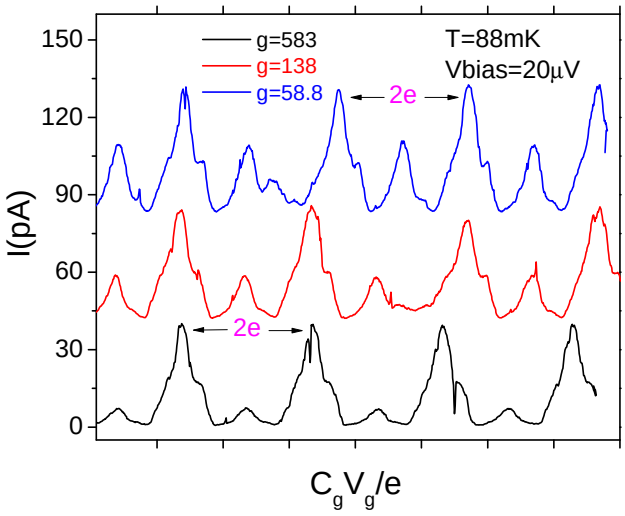

Figure 4.31: Modulation of the current by the gate charge for different g at 88mK (offset for clarity). The bias voltage is set to 20μV.

4.4.2 Summary

In this high tunneling resistance limit where charging energy is dominating, the transport properties are measured in a voltage biased configuration. Not only does the supercurrent increases with dissipation, but also the 2e parity is affect by the environment. Different current peaks on I-V curve are generated from resonant tunneling or energy exchange with dissipative environment. From the preliminary results, we conclude that the 2e periodic charge modulation exist in our sSET, but is washed out by the low impedance and strong Josephson behaviors for sSET#41 with intermediate tunnel resistance.

4.5 Discussion

4.5.1 Switching Current Measurement

When experimental data is being collected, Joule heating is always an important issue since it can increase the electron temperature significantly, adding thermal noise and causing the actual temperature to be unpredictable. In the supercurrent branch, the dissipated energy is negligible. After the sSET switches into the finite voltage state, however, the heating power is on the order of 10^{-12}W. We keep the period in the voltage state as short as possible by setting the maximum sweeping current to be a little larger than the I_{SW}. Note that the voltage state here is V=$2\Delta/e$. When the sSET goes back to zero voltage state, we have to ensure that the sSET equilibrate completely before the next escape event. The sweeping frequency of bias current is set to be low enough so that the sSET is cooled back to the bath temperature after each data point is collected. For sSET#31, at base temperature and E_J=2.3, we didn't see the Joule heating effect for maximum sweeping frequency 8Hz. Due to this, we swept the current at 5Hz in the switching current measurement.

There are two different well established methods for escape rate measurement of a Josephson junction device. We used the method developed in [78] where current is ramped up at a constant rate to I_{SW} at which the junction switches to the finite voltage state. A large number of switching events are accumulated to produce good statistics and to calculate the tunneling rate $\Gamma(I)$ from equation 4.2. Apparently, higher sweeping rate leads to a larger escape rate. Because the sweeping signals go through twisted pair wires and low pass filters, this method works well up to the order of kHz.

To increase the measurement speed, a different setup, called the pulse and hold method, can be used in a much faster experiment such as the readout for a quantum state [10, 20]. Instead of the long ramp of current from zero to the value of switching current, a set of trapezoidal current

pulses are applied to the junction. The magnitude of bias current is close to that of the switching current such that the junction is very sensitive to any perturbation. A very small trigger, such as the decay of a qubit from the excited state, will cause the junction to switch into the finite voltage state. The switching probability is obtained by measuring a set of resulting voltage pulses. Of course, the height and duration of the current pulses have to be modified for specific samples and experimental setup in order that switching events are easily identified and distinguished from the output voltage [139].

4.5.2 Noise Temperature

As mentioned above, the data for the switching current of sSET#33 were collected in different cooling down cycles. In the first measurement, we found I_{SW} lost temperature dependence below ~50mK for $E_J/E_C = 2.3$. If this is the crossover temperature from thermal regime to macroscopic quantum tunneling, T_{cr} will drop accordingly as E_J is lowered by applying magnetic field. However, all E_J cases showed this same saturation below 50mK, indicating this is the effective noise temperature of the system. Even the bath is cooled down to a lower temperature, the electrons and Cooper pairs are still at this noise temperature. We attribute the reason for this to the filtering system, which couldn't attenuate the noise efficiently.

The sSET circuit requires strong noise attenuation at low temperature [121]. For instance, the base temperature of our fridge is 15mK, corresponding to the frequency 300MHz. Above this frequency, we have to build an ultra-clean environment for the sSET, in order to measure its dynamics at 15mK. On the last stage of the fridge, one RC π and one copper powder filter have the same temperature as the sample. Thus, these two filters will not introduce noise with frequencies higher than device.

Between the copper powder filter and the sample holder, there is a 7 inch long distance connected by a copper tube of 0.085 inch diameter

with copper wires inside. We then added two copper powder filters which were made differently from the one being used. The manganin wire in the old setup was very loose, thus leaving space between adjacent turns of the solenoid. Because the new filters are shorter (2.5 inch long), we wound the manganin wires tightly together so that the effective wire was still long enough. We also used the brand new Stycast 1266 which has a much lower viscosity so that we could mix more copper powder into the epoxy. All these improvement gave a filter with much lower cut off frequency and more efficient attenuation with a shorter length [140, 141]. For instance, 80db power attenuation starts at frequency ∼1.5GHz in the older filter comparing to ∼200-300MHz in the newer setup. Each new filter has a noise attenuation greater than 140dB (noise floor) above 400MHz.

Surprisingly, we found a worse result with the two more additional filters in line. The measured switching current was much smaller than for the older setup at the same temperature, indicating the sample actually is seeing more noise. After removing the newer filters and applying strong microwave signal to the sSET, we saw similar behaviors happened in the I_{SW} measurement. This tells us that adding two new filters did not lower the noise attenuation. The wires inside the copper tube is effectively a low pass filter because of the impedance mismatch for high frequency signal. Thus, high frequency noise can not pass through to reach the sSET. Although we do not know the actual power attenuation, the high frequency noise is attenuated more efficiently with the copper tube wiring than the two new copper powder filters. A possible explanation for the bad performance of new filters is the high cut-off frequency from the effective capacitance between two adjacent turns of wire. We estimated that the cut-off is ∼40GHz which is above the highest frequency 20GHz of our spectrum analyzer. Although this filter has enough noise attenuation below 20GHz, it is not suitable for the junction because of its much higher plasma frequency.

Then we modified the RC π filter by replacing two small metal film resistors (500Ω) with two 3kΩ resistors. This decreases the 3dB roll

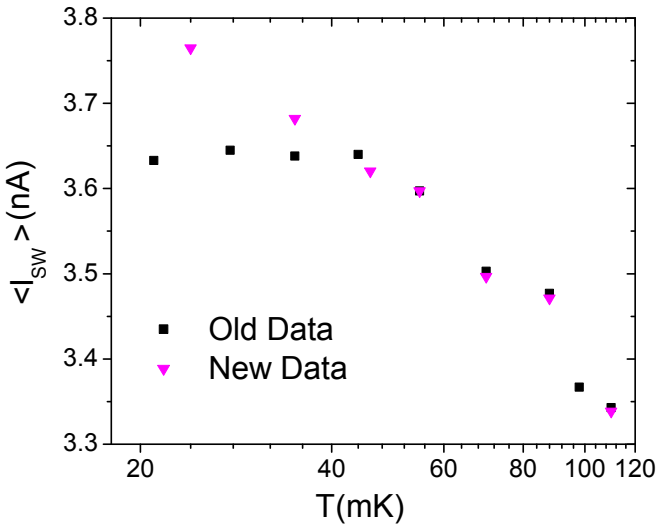

Figure 4.32: Two set of $< I_{SW} >$ data in low temperature range with old and new filters.

off frequency from ~56kHz to ~10KHz, improving the high frequency performance. Moreover, the equivalent noise voltage on the device is reduced because the filters are in series with the sSET. This treatment actually improved the low temperature results of the switching current of sSET#33. As shown in Fig. 4.32, $< I_{SW} >$ increases as we decrease the temperature below 50mK. Thus we reduced the system noise temperature to below the base temperature of the fridge. This is also confirmed in latter measurements.

4.5.3 Quasi-particle Poisoning

When the sSET is at very low temperature, Cooper pair tunneling dominates if we neglect the possibility of having any unpaired electron on the island. For instance, $I_{SW}(n_g)$ is maximized when charge states differing by one Cooper pair are degenerate, yielding a 2e periodic modulation of the gate induced charge numbers $n_g = C_g V_g / e$. The maximums occur at

$n_g = \pm e, \pm 3e, \cdots$, compressed exponentially as the gate charge is far from the degeneracy point.

In reality, there is always some out of equilibrium quasi-particles involved in the tunneling process, having a dramatic influence on the parity of the transistor. The sSET will have a 1e period of I_{SW} or conductance with the maximum at $n_g = 0, \pm e/2, \pm 3e/2 \cdots$. We have discussed the temperature dependence of the parity effect, where a free energy difference $F_0(T)$ between odd and even state can be dominated by thermal noise. In our measurement of sSET#33 and #41, we only see a 1e periodic function with respect to gate charge even at base temperature. These two samples have comparable Josephson and charging energy associated with strong quantum fluctuations in both variables. In other word, the charge states with certain numbers are not well-defined. Here, we will discuss the dynamics of the quasi-particle poisoning.

The quasi-particle tunneling rate from the leads to the island can reach as high as $\sim 50kHz$ in a standard transistor, measured by the rf-SET method [142, 143]. The essential way to reduce the poisoning is to build a higher energy profile of the island, acting as an energy barrier for the quasi-particle. If the exponentially reduced tunneling rate is smaller than the measurement speed, 2e charge oscillation will be recovered. Different methods have been tested for this task, like oxygen doping the superconducting island [108], fabricating a thinner island [109] and using a different material with higher gap [144]. Via building an energy barrier, the quasi-particles will be trapped out of the island, causing a favorite even charge state [145]. Improving the impedance of the environment can also affect this parity effect, changing the 1e periodic function of transport to 2e period [146, 147].

In our experiments, we measured the switching current, not exactly the critical current, as a function of gate charge. There are several characteristic timescales: t_{sw} is the switching times of the transistor from zero voltage to finite voltage state, t_{oe} is the odd-even equilibration time in the island, $t_r \sim 30ms$ is the time constant of the 5Hz current ramping rate.

Because the relatively long time constant of our sSET circuit, t_r is the longest time comparing to the others although we don't know the exact value of t_{sw} and t_{oe}.

In the case of $t_r \gg t_{sw} \gg t_{oe}$, during the process of switching, the sSET can be thought to evolve in an average potential corresponding to the odd and even states of the island. The switching current is then a sort of average between two values of these two states. The shape of the gate charge modulation of the switching current at low temperature is predicted by Matveev *et al* [99]. At higher temperatures, the poisoning leads to a complex pattern of the gate charge dependence, with a non-monotonic dependence on temperature.

If we assume $t_r \gg t_{oe} \gg t_{sw}$, at any value of bias current, the island stays in both the odd and even state. Because switching is the fastest phenomenon, the switching current will correspond to the minimal "critical current" of the odd or even state of the island. This causes a 1e periodic modulation of the switching current exactly as if the gap between two charge states does not exist. Comparing with our data of sSET#33 and #41, we are certain that our measurement is in this regime, where the effect of poisoning is significant.

In addition, the bias current can be ramped at a very high frequency satisfying $t_{oe} \gg t_{sw} \gg t_r$. The island changes its parity on time scales longer than the measurement. A single measurement will give the switching current corresponding to either even or odd parity. A large number of switching events will show two values of switching current corresponding to either odd or even state [108, 65].

By decreasing the ratio of E_J/E_C, the quasi-particle poisoning also can be efficiently reduced due to well-defined charge state, like sSET#39. If the sSET stays in the even state, a quasi-particle may tunnel off or on the island, changing the parity to odd. Since the even state has a lower energy and this sudden tunneling has a time interval much longer than t_{oe}, the sSET will equilibrate back to the ground state quickly through the tunneling of another electron. As a consequence, the 2e periodic

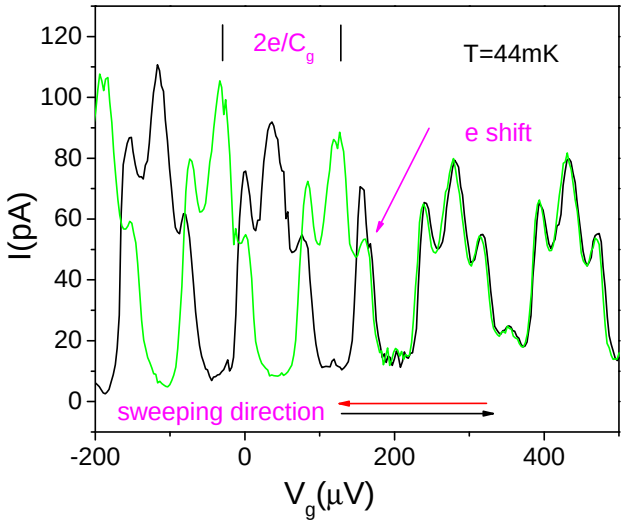

Figure 4.33: e shift of $I-V_g$ curve of sSET#40, T=44mK and g=503.

transport as a function of gate charge still remains and shows an abrupt half periodic shift.

sSET#40, which has one Josephson junction open resulting in an unbalanced sample, was measured in a voltage biased situation. The single junction tunnel resistance is $R_N = 24.0k\Omega$, $E_J/k_B \approx 296mK$ and capacitance $C_0 = 0.28fF$. From the 2e period of $I-V_g$, gate capacitance is $C_g = 2e/V_g = 2.1fF$. Thus, we estimate the charging energy to be $E_C/k_B \approx 315mK$. Because this substrate is a little thinner, R_{2DEG} can be tuned from 38.6Ω/□ to 2510Ω/□ and the smallest g is reduced to 7.7. Due to the larger resistance of the single junction on one side of the island, we see a 2e periodic function of current. As shown in Fig. 4.33, the current is measured with bias voltage $V_b = 20\mu$V, as gate voltage is swept at 1mHz. When repeating these scans, we observed the one electron shift in the curves corresponding to the sudden parity change on the island, having a time scale of a couple of hours. The tunneling of a conduction electron to the localized states within the insulator at the surface of the

island might be the reason of this parity change [106]. Thus, increasing material quality of the superconducting island can reduce this unwanted parity change significantly.

4.5.4 Phase Diffusion

Although phase diffusion plays an important role in the dynamics of a sSET, we didn't see any clear feature in the I-V curve because of the relative low voltage amplifier sensitivity (3μV) and the low impedance environment. As E_J/E_C ratio is lowered or the effective impedance seen by the sSET increases, the phase diffusion processes will become significant, causing a noticeable finite voltage branch. In Fig. 4.34, we plot the phase diffusion branch in both current and voltage biased I-V curve.

From the top panel, we see that as current is increased, the total phase of the sSET first oscillates in the bottom of a potential well, corresponding to the supercurrent region. As bias current is increased further, the phase starts to escape out the bottom and roll down to the next well. If the energy fed from the bias current does not exceed the energy dissipated in this process, then the particle could be trapped in the next well and the voltage will go back to zero. A small voltage is the average of frequent multi-phase diffusions. Its probability increases as bias current is increased continuously, causing the increased voltage. The voltage oscillations that we observed are more likely due to the phase diffusion in the time domain. The corresponding voltage biased curve is shown in the bottom panel as a clear finite conductance region. At $V \approx \pm 135\mu V$, there is another high conductance region in the top panel, shown as two steps. In the voltage biased I-V curve, two broad peaks appear at the same positions, caused by the exchange of energy between the sSET and some resonant mode of the environment. Also, we see the hysteresis almost disappear completely when phase diffusion becomes stronger.

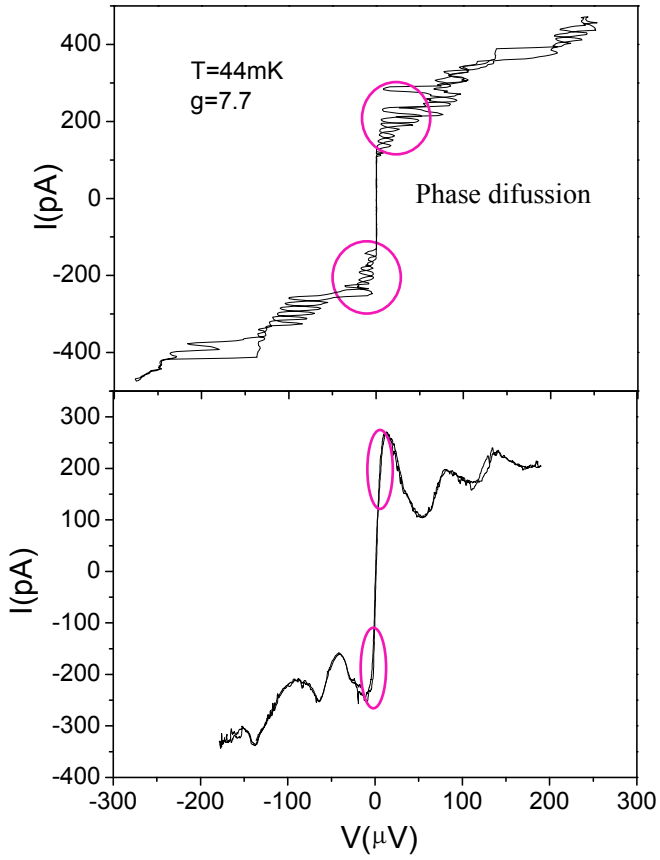

Figure 4.34: Top and bottom panel: phase diffusion in current and voltage biased cases of sSET#40. T =44mK, $R_{2DEG} = 2510\Omega/\square$.

Chapter 5

Conclusions and Outlook

To conclude, we measured superconducting single electron transistors, with comparable Josephson coupling energy E_J and charging energy E_C, in an *in situ* tunable dissipative environment. In the low impedance environment limit, the dissipation is fulfilled by capacitively coupling the sSET to a two dimensional electron gas plane. The sSET consists of two SQUIDs connected in series, with the central island capacitively coupled to the 2DEG acting as the gate. This special design allows us to tune each energy term in the Hamiltonian individually while keeping others constant. The sSETs show a clear supercurrent branch in the I-V characteristics and a gate charge oscillation of switching current. The switching current statistics and transport are measured as a function of dissipation and gate charge at different temperatures.

The main result for two representative samples sSET#33 and #41 is summarized in Fig. 5.1. If the sSET stays in the classical Josephson regime where the total phase is well-defined, $< I_{SW} >$ does not exhibit a gate charge modulation. As dissipation increases, $< I_{SW} >$, effective I_C and corresponding E_J decreases, as the consequence of dissipation compressed quantum charge fluctuations. In the charging regime, charge becomes a good quantum number, quantum fluctuations of the phase variable is significant. The periodic gate charge modulation of $< I_{SW} >$ and ΔI_{SW} shows

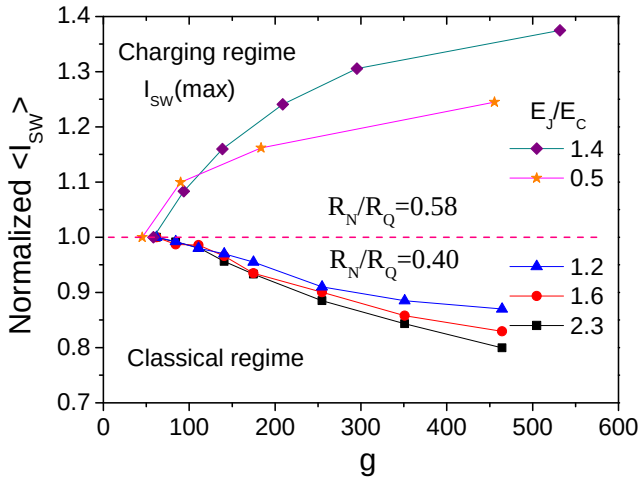

Figure 5.1: Normalized $< I_{SW} >$ of sSET#33 and sSET#41 as a function of g in classical and charging regime. Top: $T = 30$mK; bottom: $T = 55$mK.

a pronounced charging effect. For fixed gate charge numbers, quantum fluctuations of the phase are compressed with dissipation, causing the enhanced $< I_{SW} >$.

From the charge phase duality point of view, we see dissipation always reduces quantum fluctuations. In the charging regime, we find that charge variable is localized and that dissipation reduces quantum phase fluctuations, causing a better-defined phase and Josephson energy. In the classical regime with a good phase variable, charge has strong quantum fluctuations. Dissipation compresses this type of fluctuation, causing a decreased switching current and Josephson energy. We see that the transition between these two regimes is found to be $R_N = R_Q/2$, as shown in Fig. 5.1.

In the classical regime, the reduction of $< I_{SW} >$ due to dissipation becomes smaller at higher temperature, due to thermal noise effect on phase variable. Also, the effect of dissipation is stronger for a larger E_J/E_C ratio. ΔI_{SW} decreases monotonically with temperature above 40mK, showing a strong role of thermal phase diffusion in the escape process.

Our results qualitatively agree with the theory of a single Josephson junction in a frequency dependent dissipative environment.

In the charging regime, we find that ΔI_{SW} shows a 1e periodicity with respect to gate charge, with a sharp dip at $C_g V_g/e = 1/2$. The temperature dependence of ΔI_{SW} has two slopes, indicating quantum phase diffusion at low temperature and classical thermal phase diffusion in the higher temperature region. The influence of dissipation is consistent with the theory of a sSET capacitively coupled to a dissipative environment in the charging regime.

Because two relevant theories are based on different assumptions: one is in the Josephson regime and another is in the charging regime. In our experiment, we find two sSETs having very similar parameters, stay in different regimes. In the limit that E_J is comparable with E_C, both phase and charge have significant quantum fluctuations. We find that the regime in which the device stay is very sensitive to the quantum fluctuations in phase or charge variable. A detailed theory which can explain the self-consistent observations in this thesis with a clean picture, need to be determined by future work.

We can also conclude that whether the sSET is in classical or charging regime is not mainly determined by the competition of E_J and E_C, but rather by the tunnel resistance of the SQUID. In a low impedance environment, the phase is strengthened by dissipation for the sSET in charging regime, but weakened in classical Josephson regime. This give us a new method to determine whether phase or charge is good variable in such a system.

There are still several questions arising in our experiment. If we can tune the R_{2DEG} over a much larger range by polishing off the substrate more, the dissipation can become very weak. In this higher impedance environment, will dissipation have the same impact on I_{SW} of the sSET in classical regime? If I_{SW} switches from being increased to reduced as dissipation decreases, this will be the so-called dissipation driven phase transition. Moreover, at very large R_{2DEG}, the effective impedance of

the environment starts to decrease at the highest frequency, making the experiments more suspicious. To avoid this problem, we can reduce the plasma frequency of the sSET by making the shunting capacitance larger. However, this on-chip treatment will bring more coupling items to the 2DEG and make the circuit more complicated.

Whether the sSET in classical regime can enter the charging regime by decreasing effective Josephson energy is still not clear. We see that in the regime $E_J/E_C \sim 1$, the devices still behaves in the classical regime. Because the switching current in the very small E_J case will be reduced significantly due to the charging effect, the temperature corresponding to E_J may be comparable to thermal noise even at very low temperature.

The dissipation dependence of $< I_{SW} >$ of sSET#41 is greater for $E_J/E_C = 1.4$ than $E_J/E_C = 0.54$. In our model, the smaller E_J/E_C has stronger charging effect. The increase of $< I_{SW} >$ due to dissipation should be larger.

If we can observe 2e charge modulation of the switching current, will we see the dip of ΔI_{SW} as well? In terms of quasi-particle poisoning, introducing normal metal in the leads close to the sSET can efficiently reduce the tunneling rate and recover the 2e periodic modulation, however this normal metal might hide the intrinsic dip of ΔI_{SW} at the degeneracy point.

To solve these questions, more careful measurements should be carried out. One possible solution is to increase the superconducting energy gap of the island, building a natural energy barrier for the quasi-particle. If the even parity is recovered, the switching current will be significantly increased at $C_g V_g/e = 1$. With this improvement, on would have a large signal in the measurement even for a much smaller E_J/E_C. This would allow one to tune the parameters of the device to a larger range, from $E_J/E_C < 1$ to $E_J/E_C > 1$.

Bibliography

The numbers at the end of each entry list pages where the reference was cited. In the electronic version, they are clickable links to the pages.

[1] Y. Makhlin, G. Schön, and A. Shnirman, Rev. Mod. Phys. **73**, 357 (2001). 2

[2] J. Clarke and F. K. Wilhelm, Nature(London) **453**, 1031 (2008). 2

[3] A. V. Timofeev, M. Meschke, J. T. Peltonen, T. T. Heikkilä, and J. P. Pekola, Phys. Rev. Lett. **98**, 207001 (2007). 2

[4] Q. Le Masne, H. Pothier, N. O. Birge, C. Urbina, and D. Esteve, Phys. Rev. Lett. **102**, 067002 (2009). 2

[5] Y.-F. Chen *et al.*, Phys. Rev. Lett. **107**, 217401 (2011). 2

[6] Y. Nakamura, C. D. Chen, and J. S. Tsai, Phys. Rev. Lett. **79**, 2328 (1997). 2, 112

[7] Y. Nakamura, Y. A. Pashkin, and J. S. Tsai, Nature(London) **398**, 786 (1999). 2

[8] J. R. Friedman, V. Patel, W. Chen, S. K. Tolpygo, and J. E. Lukens, Nature(London) **406**, 43 (1999). 2

[9] C. H. van der Wal *et al.*, Science **290**, 773 (2000). 2

[10] I. Chiorescu, Y. Nakamura, C. Harmans, and J. Mooij, Science **299**, 1869 (2003). 2, 120

[11] J. M. Martinis, M. H. Devoret, and J. Clarke, Phys. Rev. Lett. **55**, 1543 (1985). 2, 15

[12] Y. Yu, S. Han, X. Chu, S.-I. Chu, and Z. Wang, Science **296**, 889 (2002). 2, 16

[13] J. M. Martinis, S. Nam, J. Aumentado, and C. Urbina, Phys. Rev. Lett. **89**, 117901 (2002). 2, 16

[14] D. J. Van Harlingen *et al.*, Phys. Rev. B **70**, 064517 (2004). 2

[15] Y. Nakamura, Y. A. Pashkin, T. Yamamoto, and J. S. Tsai, Phys. Rev. Lett. **88**, 047901 (2002). 2

[16] O. Astafiev, Y. A. Pashkin, Y. Nakamura, T. Yamamoto, and J. S. Tsai, Phys. Rev. Lett. **93**, 267007 (2004). 2

[17] F. Yoshihara, K. Harrabi, A. O. Niskanen, Y. Nakamura, and J. S. Tsai, Phys. Rev. Lett. **97**, 167001 (2006). 2

[18] J. M. Martinis *et al.*, Phys. Rev. Lett. **95**, 210503 (2005). 2

[19] Z. Kim *et al.*, Phys. Rev. Lett. **106**, 120501 (2011). 2

[20] D. Vion *et al.*, Science **296**, 886 (2002). 3, 120

[21] G. Ithier *et al.*, Phys. Rev. B **72**, 134519 (2005). 3

[22] J. Koch, V. Manucharyan, M. H. Devoret, and L. I. Glazman, Phys. Rev. Lett. **103**, 217004 (2009). 3, 4

[23] V. E. Manucharyan, J. Koch, L. I. Glazman, and M. H. Devoret, Science **326**, 113 (2009). 3

[24] J. Koch *et al.*, Phys. Rev. A **76**, 042319 (2007). 3

[25] J. A. Schreier *et al.*, Phys. Rev. B **77**, 180502 (2008). 3

[26] A. O. Caldeira and A. J. Leggett, Phys. Rev. Lett. **46**, 211 (1981). 3, 22

[27] A. Caldeira and A. Leggett, Annals of Physics **149**, 374 (1983). 3, 22

[28] J. S. Penttilä, U. Parts, P. J. Hakonen, M. A. Paalanen, and E. B. Sonin, Phys. Rev. Lett. **82**, 1004 (1999). 3, 4, 26

[29] C. P. Herrero and A. D. Zaikin, Phys. Rev. B **65**, 104516 (2002). 3

[30] S. V. Lotkhov, S. A. Bogoslovsky, A. B. Zorin, and J. Niemeyer, Phys. Rev. Lett. **91**, 197002 (2003). 3, 4, 5, 6, 38, 55, 110

[31] H. Miyazaki, Y. Takahide, A. Kanda, and Y. Ootuka, Phys. Rev. Lett. **89**, 197001 (2002). 3

[32] K.-H. Wagenblast, A. van Otterlo, G. Schön, and G. T. Zimányi, Phys. Rev. Lett. **79**, 2730 (1997). 3

[33] A. J. Rimberg *et al.*, Phys. Rev. Lett. **78**, 2632 (1997). 3, 4

[34] Y. Takahide, R. Yagi, A. Kanda, Y. Ootuka, and S.-i. Kobayashi, Phys. Rev. Lett. **85**, 1974 (2000). 3

[35] L. Capriotti, A. Cuccoli, A. Fubini, V. Tognetti, and R. Vaia, Phys. Rev. Lett. **94**, 157001 (2005). 3

[36] G. Liu, Y. Zhang, and C. N. Lau, Phys. Rev. Lett. **102**, 016803 (2009). 3

[37] H. Grabert, U. Weiss, and P. Hanggi, Phys. Rev. Lett. **52**, 2193 (1984). 4

[38] R. L. Kautz and J. M. Martinis, Phys. Rev. B **42**, 9903 (1990). 4, 25

[39] G. Schon and A. D. Zaikin, Physics Reports **198**, 237 (1990). 4, 18

[40] M. H. Devoret *et al.*, Phys. Rev. Lett. **64**, 1824 (1990). 4, 22

[41] S. M. Girvin, L. I. Glazman, M. Jonson, D. R. Penn, and M. D. Stiles, Phys. Rev. Lett. **64**, 3183 (1990). 4, 22

[42] G. L. Ingold and Y. Nazarov, in *Single Charge Tunneling*, edited by H. Grabert and M. Devoret, Plenum Press, New York, 1992. 4, 22, 110

[43] G.-L. Ingold, H. Grabert, and U. Eberhardt, Phys. Rev. B **50**, 395 (1994). 4, 24

[44] H. Grabert, G.-L. Ingold, and B. Paul, EPL (Europhysics Letters) **44**, 360 (1998). 4, 24, 85, 95

[45] G.-L. Ingold and H. Grabert, Phys. Rev. Lett. **83**, 3721 (1999). 4

[46] H. Grabert and G.-L. Ingold, Superlattices and Microstructures **25**, 915 (1999). 4, 24

[47] F. K. Wilhelm, G. Schön, and G. T. Zimányi, Phys. Rev. Lett. **87**, 136802 (2001). 4, 5, 6, 37, 100, 108, 110

[48] E. Turlot *et al.*, Phys. Rev. Lett. **62**, 1788 (1989). 4, 14

[49] D. Vion, M. Götz, P. Joyez, D. Esteve, and M. H. Devoret, Phys. Rev. Lett. **77**, 3435 (1996). 4, 14, 92, 93

[50] S. Corlevi, W. Guichard, F. W. J. Hekking, and D. B. Haviland, Phys. Rev. Lett. **97**, 096802 (2006). 4, 26

[51] J. B. Kycia *et al.*, Phys. Rev. Lett. **87**, 017002 (2001). 4, 5, 6, 38

[52] L. S. Kuzmin, Y. V. Nazarov, D. B. Haviland, P. Delsing, and T. Claeson, Phys. Rev. Lett. **67**, 1161 (1991). 4, 24, 26

[53] P. Joyez, P. Lafarge, A. Filipe, D. Esteve, and M. H. Devoret, Phys. Rev. Lett. **72**, 2458 (1994). 4, 5, 32, 55

[54] T. Holst, D. Esteve, C. Urbina, and M. H. Devoret, Phys. Rev. Lett. **73**, 3455 (1994). 4

[55] M. Watanabe and D. B. Haviland, Phys. Rev. Lett. **86**, 5120 (2001). 4, 26, 79

[56] W. Lu, A. J. Rimberg, and K. D. Maranowski, Appl. Phys. Lett. **81**, 4976 (2002). 4, 62, 110

[57] W. Lu, A. J. Rimberg, K. D. Maranowski, and A. C. Gossard, **77**, 2746 (2000). 4

[58] R. M. Lutchyn, V. Galitski, G. Refael, and S. Das Sarma, Phys. Rev. Lett. **101**, 106402 (2008). 4

[59] K. Likharev and A. Zorin, Journal of Low Temperature Physics **59**, 347 (1985). 4, 18

[60] D. V. Averin and K. K. Likharev, Journal of Low Temperature Physics **62**, 345 (1986). 4, 18

[61] T. A. Fulton and G. J. Dolan, Phys. Rev. Lett. **59**, 109 (1987). 4

[62] R. J. Schoelkopf, P. Wahlgren, A. A. Kozhevnikov, P. Delsing, and D. E. Prober, Science **280**, 1238 (1998). 4, 39

[63] M. H. Devoret and R. J. Schoelkopf, Nature(London) **406**, 1039 (2000). 4

[64] L. J. Geerligs, V. F. Anderegg, J. Romijn, and J. E. Mooij, Phys. Rev. Lett. **65**, 377 (1990). 5, 110

[65] D. J. Flees, S. Han, and J. E. Lukens, Phys. Rev. Lett. **78**, 4817 (1997). 5, 35, 125

[66] A. B. Zorin, Phys. Rev. Lett. **76**, 4408 (1996). 5, 35, 85

[67] P.-M. Billangeon, F. Pierre, H. Bouchiat, and R. Deblock, Phys. Rev. Lett. **98**, 126802 (2007). 5

[68] W. Lu, K. D. Maranowski, and A. J. Rimberg, Phys. Rev. B **65**, 060501 (2002). 5

[69] M. Watanabe, Phys. Rev. B **69**, 094509 (2004). 5, 36

[70] S. Corlevi, W. Guichard, F. W. J. Hekking, and D. B. Haviland, Phys. Rev. B **74**, 224505 (2006). 5, 36

[71] A. Barone and G. Paterno, *Physics and Applications of the Josephson Effect* (Wiley-VCH, 1982). 10

[72] M. Tinkham, *Introduction to Superconductivity*, 2nd ed. (McGraw-Hill, New York, 1996). 10

[73] B. D. Josephson, Physics Letters **1**, 251 (1962). 10

[74] V. Ambegaokar and A. Baratoff, Phys. Rev. Lett. **10**, 486 (1963). 10

[75] S. Shapiro, Phys. Rev. Lett. **11**, 80 (1963). 11

[76] W. C. Stewart, Appl. Phys. Lett. **12**, 277 (1968). 11

[77] D. E. McCumber, J. Appl. Phys. **39**, 3113 (1968). 11

[78] T. A. Fulton and L. N. Dunkleberger, Phys. Rev. B **9**, 4760 (1974). 14, 82, 120

[79] P. Silvestrini, S. Pagano, R. Cristiano, O. Liengme, and K. E. Gray, Phys. Rev. Lett. **60**, 844 (1988). 14

[80] L. D. Jackel *et al.*, Phys. Rev. Lett. **47**, 697 (1981). 14

[81] R. F. Voss and R. A. Webb, Phys. Rev. Lett. **47**, 265 (1981). 14

[82] M. H. Devoret, J. M. Martinis, and J. Clarke, Phys. Rev. Lett. **55**, 1908 (1985). 14

[83] S. Washburn, R. A. Webb, R. F. Voss, and S. M. Faris, Phys. Rev. Lett. **54**, 2712 (1985). 14

[84] J. M. Martinis, M. H. Devoret, and J. Clarke, Phys. Rev. B **35**, 4682 (1987). 14, 73

[85] H. A. Kramers, Physica **7**, 284 (1940). 14

[86] J. Clarke, A. N. Cleland, M. H. Devoret, D. Esteve, and J. M. Martinis, Science **239**, 992 (1988). 15

[87] A. Wallraff, T. Duty, A. Lukashenko, and A. V. Ustinov, Phys. Rev. Lett. **90**, 037003 (2003). 16

[88] S.-X. Li *et al.*, Phys. Rev. Lett. **89**, 098301 (2002). 18

[89] F. Balestro, J. Claudon, J. P. Pekola, and O. Buisson, Phys. Rev. Lett. **91**, 158301 (2003). 18

[90] L. S. Kuzmin and D. B. Haviland, Phys. Rev. Lett. **67**, 2890 (1991). 21

[91] D. V. Averin, Y. V. Nazarov, and A. A. Odintsov, Physica B **165**, 945 (1990). 24

[92] M. Iansiti, M. Tinkham, A. T. Johnson, W. F. Smith, and C. J. Lobb, Phys. Rev. B **39**, 6465 (1989). 25

[93] A. T. Johnson, C. J. Lobb, and M. Tinkham, Phys. Rev. Lett. **65**, 1263 (1990). 25

[94] J. M. Martinis and R. L. Kautz, Phys. Rev. Lett. **63**, 1507 (1989). 25

[95] J. M. Kivioja *et al.*, Phys. Rev. Lett. **94**, 247002 (2005). 25, 88

[96] A. Steinbach *et al.*, Phys. Rev. Lett. **87**, 137003 (2001). 25

[97] A. N. Cleland, J. M. Schmidt, and J. Clarke, Phys. Rev. Lett. **64**, 1565 (1990). 26

[98] M. Watanabe and D. B. Haviland, Phys. Rev. B **67**, 094505 (2003). 26

[99] K. A. Matveev, M. Gisselfält, L. I. Glazman, M. Jonson, and R. I. Shekhter, Phys. Rev. Lett. **70**, 2940 (1993). 32, 125

[100] M. T. Tuominen, J. M. Hergenrother, T. S. Tighe, and M. Tinkham, Phys. Rev. Lett. **69**, 1997 (1992). 32

[101] M. T. Tuominen, J. M. Hergenrother, T. S. Tighe, and M. Tinkham, Phys. Rev. B **47**, 11599 (1993). 32

[102] T. M. Eiles and J. M. Martinis, Phys. Rev. B **50**, 627 (1994). 32, 35, 110

[103] A. Amar, D. Song, C. J. Lobb, and F. C. Wellstood, Phys. Rev. Lett. **72**, 3234 (1994). 32

[104] M. Tinkham, J. M. Hergenrother, and J. G. Lu, Phys. Rev. B **51**, 12649 (1995). 32

[105] J. G. Lu, J. M. Hergenrother, and M. Tinkham, Phys. Rev. B **53**, 3543 (1996). 32

[106] T. M. Eiles, J. M. Martinis, and M. H. Devoret, Phys. Rev. Lett. **70**, 1862 (1993). 32, 127

[107] J. M. Hergenrother, M. T. Tuominen, and M. Tinkham, Phys. Rev. Lett. **72**, 1742 (1994). 32

[108] J. Aumentado, M. W. Keller, J. M. Martinis, and M. H. Devoret, Phys. Rev. Lett. **92**, 066802 (2004). 33, 124, 125

[109] T. Yamamoto, Y. Nakamura, Y. A. Pashkin, O. Astafiev, and J. S. Tsai, Applied Physics Letters **88**, 212509 (2006). 33, 124

[110] D. V. Averin and K. K. Likharev, in *Mesoscopic Phenomena in Solids*, edited by B. L. Altshuler, P. A. Lee, and R. A. Webb, volume 294, North Holland, 1991. 33

[111] A. B. Zorin *et al.*, Journal of Superconductivity **12**, 747 (1999). 35, 36

[112] K. K. Likharev, Magnetics, IEEE Transactions on **23**, 1142 (1987). 39

[113] L. Spietz, K. Irwin, and J. Aumentado, Applied Physics Letters **95**, 092505 (2009). 39

[114] M. Mück and R. McDermott, Superconductor Science and Technology **23**, 093001 (2010). 39

[115] R. E. Williams, *Modern GaAs Processing Methods*, 2nd ed. (Artech House, Boston, 1990). 43

[116] G. J. Dolan, Appl. Phys. Lett. **31**, 337 (1977). 53

[117] L. J. van der Pauw, Philips Technical Review **20**, 220 (1958). 60

[118] J. R. Petta, A. C. Johnson, C. M. Marcus, M. P. Hanson, and A. C. Gossard, Phys. Rev. Lett. **93**, 186802 (2004). 62

[119] M. Pioro-Ladrière *et al.*, Phys. Rev. B **72**, 115331 (2005). 62, 69

[120] F. Pobell, *Matter and Methods at Low Temperatures*, 2nd ed. (Springer, 2002). 66

[121] D. Vion, P. F. Orfila, P. Joyez, D. Esteve, and M. H. Devoret, Journal of Applied Physics **77**, 2519 (1995). 72, 121

[122] A. B. Zorin, Review of Scientific Instruments **66**, 4296 (1995). 73

[123] A. Fukushima *et al.*, Instrumentation and Measurement, IEEE Transactions on **46**, 289 (1997). 74

[124] H. S. J. van der Zant, D. Berman, T. P. Orlando, and K. A. Delin, Phys. Rev. B **49**, 12945 (1994). 79

[125] L. J. Geerligs, M. Peters, L. E. M. de Groot, A. Verbruggen, and J. E. Mooij, Phys. Rev. Lett. **63**, 326 (1989). 79

[126] J. Männik *et al.*, Phys. Rev. B **71**, 220509 (2005). 84, 88

[127] J. C. Fenton and P. A. Warburton, Phys. Rev. B **78**, 054526 (2008). 84

[128] V. M. Krasnov *et al.*, Phys. Rev. Lett. **95**, 157002 (2005). 88

[129] S.-X. Li *et al.*, Phys. Rev. Lett. **99**, 037002 (2007). 88

[130] H. F. Yu *et al.*, Phys. Rev. Lett. **107**, 067004 (2011). 90, 106

[131] P. Joyez, D. Vion, M. Gotz, M. H. Devoret, and D. Esteve, Journal of Superconductivity **12**, 757 (1999). 92

[132] P. Agren, J. Walter, and D. B. Haviland, Phys. Rev. B **66**, 014510 (2002). 95

[133] G. Zimmerli, T. M. Eiles, R. L. Kautz, and J. M. Martinis, Applied Physics Letters **61**, 237 (1992). 97

[134] A. M. van den Brink, A. A. Odintsov, P. A. Bobbert, and G. Schon, Z. Physica B Condensed Matter **85**, 459 (1991). 110

[135] D. B. Haviland, Y. Harada, P. Delsing, C. D. Chen, and T. Claeson, Phys. Rev. Lett. **73**, 1541 (1994). 110, 114

[136] T. A. Fulton, P. L. Gammel, D. J. Bishop, L. N. Dunkleberger, and G. J. Dolan, Phys. Rev. Lett. **63**, 1307 (1989). 110

[137] Y. Nakamura, C. D. Chen, and J. S. Tsai, Phys. Rev. B **53**, 8234 (1996). 110

[138] J. J. Toppari *et al.*, Phys. Rev. B **76**, 172505 (2007). 114

[139] J. Walter, E. Tholén, D. B. Haviland, and J. Sjöstrand, Phys. Rev. B **75**, 094515 (2007). 121

[140] K. Bladh *et al.*, Review of Scientific Instruments **74**, 1323 (2003). 122

[141] A. Lukashenko and A. V. Ustinov, Review of Scientific Instruments **79**, 014701 (2008). 122

[142] O. Naaman and J. Aumentado, Phys. Rev. B **73**, 172504 (2006). 124

[143] A. J. Ferguson, N. A. Court, F. E. Hudson, and R. G. Clark, Phys. Rev. Lett. **97**, 106603 (2006). 124

[144] S. J. MacLeod, S. Kafanov, and J. P. Pekola, Applied Physics Letters **95**, 052503 (2009). 124

[145] N. A. Court, A. J. Ferguson, R. Lutchyn, and R. G. Clark, Phys. Rev. B **77**, 100501 (2008). 124

[146] W. Kuo, C. S. Wu, J. H. Shyu, and C. D. Chen, Phys. Rev. B **74**, 184522 (2006). 124

[147] A. M. Savin *et al.*, Applied Physics Letters **91**, 063512 (2007). 124